Universidade de Aveiro Departamento de Engenharia Mecânica
2014

Carlos Manuel Rodrigues de Almeida

Optimization of Li-ion solid electrolytes

Otimização de eletrólitos sólidos de iões-Lítio

Universidade de Aveiro Departamento de Engenharia Mecânica
2014

Carlos Manuel Rodrigues de Almeida

Optimization of Li-ion solid electrolytes

Otimização de eletrólitos sólidos de iões-Lítio

Dissertação apresentada à Universidade de Aveiro para cumprimento dos requisitos necessários à obtenção do grau de Mestre em Sistemas Energéticos Sustentáveis, realizada sob a orientação científica do Doutor Duncan Paul Fagg, Equiparado a Investigador Auxiliar do Departamento de Engenharia Mecânica da Universidade de Aveiro.

Dedico este trabalho aos meus avós.

o júri

presidente

Professor Doutor Luís António da Cruz Tarelho
Professor Auxiliar do Departamento de Ambiente e Ordenamento da Universidade de Aveiro

Doutor Duncan Paul Fagg
Equiparado a Investigador Auxiliar do Departamento de Engenharia Mecânica da Universidade de Aveiro

Doutor Andrei Kavaleuski
Equiparado a Investigador Principal no CICECO do Departamento de Engenharia de Materiais e Cerâmica da Universidade de Aveiro

agradecimentos

Agradeço toda a ajuda prestada no decorrer do meu trabalho pelo meu orientador, Dr. Duncan Fagg; pelas minhas coorientadoras, Ana Brandão e Isabel Antunes; e pelos meus colegas Tao Yang e Narender Nasani.
Também não posso deixar de agradecer ao grupo de química alimentar do Prof. Dr. Jorge Saraiva, em particular ao Rui Queirós, assim como a todas as pessoas com quem me cruzei no laboratório do NRD e da Cerâmica.
E agradeço aos meus familiares e amigos pelo apoio dado ao longo de todo este tempo.

acknowledgements

I want to thank all the help provided during my work by my supervisor, Dr. Duncan Fagg; by my technical cosupervisors, MSc. Ana Brandão and Isabel Antunes; and my colleagues Tao Yang and Narender Nasani.
I also want to thank the research group of prof. Dr. Jorge Saraiva, particularly to Rui Queirós, as well as all people with whom I cross paths in the NRD and the Ceramics laboratories.
And my family and friends for their support during all this time.

palavras-chave

Eletrólitos sólidos, Baterias ar-lítio, Perovsquite, NASICON, Mecanosintese, Sol-Gel.

resumo

A síntese e otimização das propriedades de dois eletrólitos sólidos, condutores de iões de lítio, foram estudadas neste trabalho.

Várias combinações de precursores foram usadas para preparar $La_{0.5}Li_{0.5}TiO_3$ através de mecanosíntese. Apesar da obtenção duma fase perovskite, através da reação mecanoquímica, não foi possível obter uma fase pura de $La_{0.5}Li_{0.5}TiO_3$ por via deste processo. De todas as sete combinações de precursores e condições, que foram testadas, aquela em que se moeram La_2O_3, Li_2CO_3 e TiO_2 ao longo de 480min (LaOLiCO-480) foi a que apresentou melhores resultados. As principais fases das impurezas foram La_2O_3 após a mecanosíntese (22.84%) e Li_2TiO_3 após a calcinação (4.20%).

Dois métodos de síntese sol-gel foram utilizados para dopar $LiZr_2(PO_4)_3$ com boro no lugar do zircónio, $Li_{1+x}Zr_{2-x}B_x(PO_4)_3$, ou no lugar do fósforo, $Li_{1+6x}Zr_2(P_{1-x}B_xO_4)_3$; com a dopagem a ser alcançada no lugar do Zr utilizando um método adaptado de Alamo *et al* (1989). Os resultados mostram que a substituição no lugar do Zr é o mecanismo preferencial na dopagem de $LiZr_2(PO_4)_3$ com B e não no lugar do P. Foi efetuado o refinamento Rietveld dos parâmetros da célula unitária, tendo sido verificado pela aplicação da lei de Vegard que é possível obter uma fase pura até x = 0.05. Esta verificação está de acordo com as fases presentes nos dados de DRX, que mostram a presença adicional da fase de baixa temperatura (monoclínica) para os pós sinterizados a 1200ºC durante 12h, para as composições com $x \geq 0.075$. As composições, dentro do limite de solubilidade sólida, apresentam uma transição da fase triclínica (PDF#01-074-2562) para romboédrica (PDF#01-070-6734) quando aquecidas de 25 para 100ºC, tal como indicado na bibliografia consultada para a composição base. Apesar de vários esforços, não foi possível obter pastilhas bem densificadas e integras após o ciclo de sinterização, sendo necessário trabalho adicional para conseguir obter pastilhas densas para posterior caracterização eletroquímica das composições $LiZr_2(PO_4)_3$ e $Li_{1.05}Zr_{1.95}B_{0.05}(PO_4)_3$.

keywords

Solid Electrolytes, Lithium-Air Batteries, Perovskite, NASICON, Mechanosynthesis, Sol-Gel.

abstract

The synthesis and optimization of two Li-ion solid electrolytes were studied in this work.

Different combinations of precursors were used to prepare $La_{0.5}Li_{0.5}TiO_3$ via mechanosynthesis. Despite the ability to form a perovskite phase by the mechanochemical reaction it was not possible to obtain a pure $La_{0.5}Li_{0.5}TiO_3$ phase by this process. Of all the seven combinations of precursors and conditions tested, the one where La_2O_3, Li_2CO_3 and TiO_2 were milled for 480min (LaOLiCO-480) showed the best results, with trace impurity phases still being observed. The main impurity phase was that of La_2O_3 after mechanosynthesis (22.84%) and Li_2TiO_3 after calcination (4.20%).

Two different sol-gel methods were used to substitute boron on the Zr-site of $Li_{1+x}Zr_{2-x}B_x(PO_4)_3$ or the P-site of $Li_{1+6x}Zr_2(P_{1-x}B_xO_4)_3$, with the doping being achieved on the Zr-site using a method adapted from Alamo *et al* (1989). The results show that the Zr-site is the preferential mechanism for B doping of $LiZr_2(PO_4)_3$ and not the P-site. Rietveld refinement of the unit-cell parameters was performed and it was verified by consideration of Vegard's law that it is possible to obtain phase purity up to $x = 0.05$. This corresponds with the phases present in the XRD data, that showed the additional presence of the low temperature (monoclinic) phase for the powder sintered at 1200ºC for 12h of compositions with $x \geq 0.075$. The compositions inside the solid solution undergo the phase transition from triclinic (PDF#01-074-2562) to rhombohedral (PDF#01-070-6734) when heating from 25 to 100ºC, as reported in the literature for the base composition. Despite several efforts, it was not possible to obtain dense pellets and with physical integrity after sintering, requiring further work in order to obtain dense pellets for the electrochemical characterisation of $Li\,Zr_2(PO_4)_3$ and $Li_{1.05}Zr_{1.95}B_{0.05}(PO_4)_3$.

Table of Contents

List of figures

List of tables

Abbreviations

% – percentage.

σ - conductivity.

ρ – density.

ΔL – length variation.

Δm – mass variation.

2θ - two theta.

Å – Angstrom.

a.u. – arbitrary units.

B – Boron.

Cl – Chlorine.

cm – centimetres

d – pellet diameter.

dm – decimetre.

g – gram.

h – hours.

H – Hydrogen.

hkl - Miller indices.

I – Intensity.

kg – kilogram.

La – Lanthanum.

Li – Lithium.

LLTO – lithium lanthanum titanate.

m – mass.

m – meter.

min – minutes.

mm – millimetre.

NASICON – sodium super ionic conductor.

n.a. – not available.

O – oxygen.

ºC – degree Celsius.

P – phosphorous.

RT – room temperature.

S – Siemens.

T – temperature.

t – time.

TGA – thermogravimetric analysis.

th – pellet thickness.

Ti – Titanium.

V – volume.

W – water.

x – Boron molar doping content in lithium zirconium phosphate [$Li_{1+6x}Zr_2(P_{1-x}B_xO_4)_3$ and of $Li_{1+x}Zr_{2-x}B_x(PO_4)_3$].

x – Lithium molar content in lithium lanthanum titanate ($Li_{3x}La_{2/3-x}TiO_3$).

XRD – X-ray diffraction.

Zr – Zirconium.

Chapter 1 - Introduction

1.1. World energy trends

During the last 40 years the total amount of energy consumed in the world keeps growing fast, as can be observed in Figure 1. This growth is mostly driven by increased usage in Brazil, Russia, India, South Africa (BRICS) and especially China, but also by the organisation for economic co-operation and development (OECD) countries constant high demand.

Figure 1 and Figure 2, also demonstrate that the majority of the fuel sources used to produce the energy consumed in the World are still based on fossil fuels, like coal, oil and natural gas. It is well known that the combustion of these fossil fuels causes health problems and environmental degradation, especially due to the emissions of CO_2; a greenhouse effect gas.

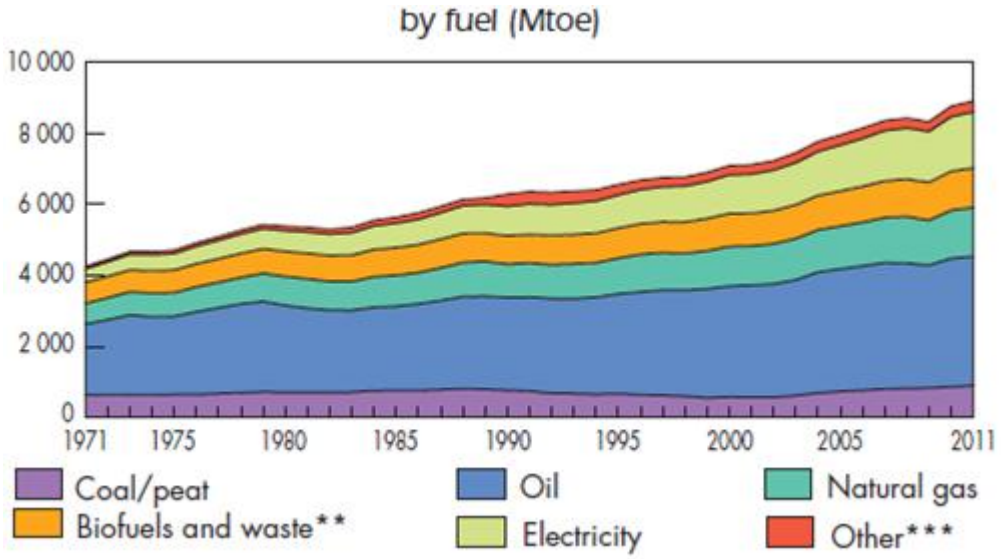

Figure 1: Annual evolution of world energy consumption, by fuel type, from 1971 to 2011 [1].

Consequently the CO_2 emissions, responsible for the largest percentage of Human induced greenhouse effect, also keep growing as is shown in Figure 3. This is a problem that needs to be addressed, creating new possibilities for alternative fuel sources to be explored and developed. Special focus is given to renewable energy sources like hydroelectric, solar, wind, waves, tidal, geothermal and others, to help solve this issue.

The fossil fuel sources are finite and its constant supply to countries that do not produce large amounts of these fuels creates a dependency relationship with the producing countries. In any industrialized nation, an uninterruptible source of energy is critical for its economic stability and energy security. As most industrialized countries are dependent on other countries for their energy, their economies are dependent on the availability of other countries to supply it.

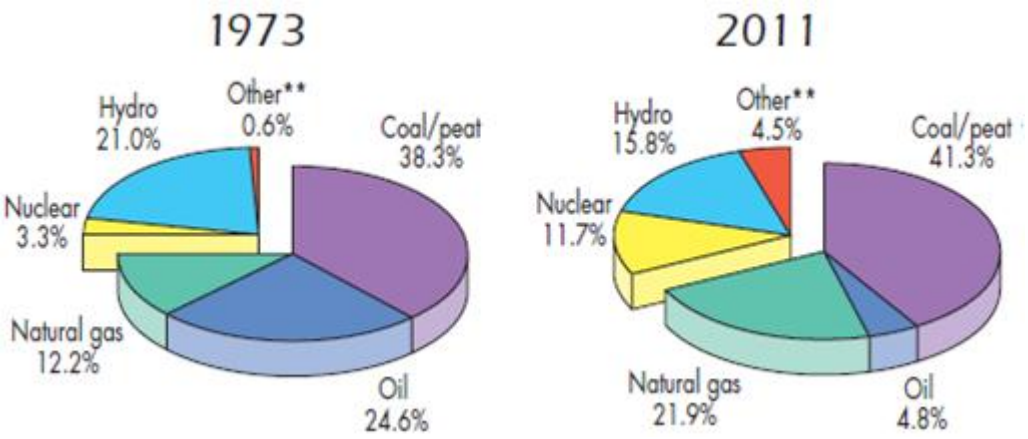

Figure 2: Percentage of electricity generation by type of fuel source [1].

The reserves of these fossil fuels is predicted to decline and be unable to satisfy the demand over medium to long term and, even if they can be consumed more efficiently through enhanced energy conversion technologies and other means, they still are not renewable in the time frame of their consumption. Thus, fossil fuels cannot be seen as the definitive solution to the problem of energy demand, meaning that an alternative needs to be developed [2]. However, most alternative renewable fuels are still far from being competitive with fossil fuels in both cost and production capacity.

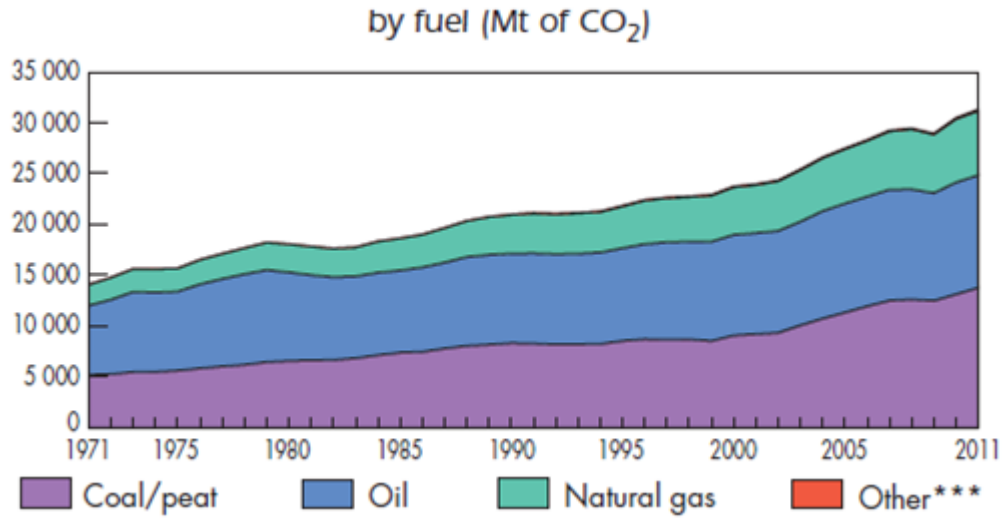

Figure 3: Annual evolution of the CO2 emissions, by fuel type, from 1971 to 2011 [1].

1.2. Energy storage

The renewable energy sources alone are neither the definitive answer to the problems associated with pollution and external dependency of fossil energy sources, because they have some intrinsic problems that need to be tackled and solved with further solutions and technology development.

According to Al-Hallaj *et al* [2], the most important challenges for the wide spread adoption of renewable energy technologies can be divided in three categories: economic, technological and social, while the main advantages and disadvantages of their use are the ones cited below.

“Most important advantages:

• The operation of renewable energy systems produces no harmful emissions, and for that reason have no adverse effects on people’s health. Additionally, no greenhouse gases are emitted as a result of their operation.

• Variety and long term viability of methods to produce electricity. As a result of the large number of electricity production technologies, renewable energy is also viewed as a means to enhance energy security. Since electricity can be generated from a variety of renewable sources, any country with a large enough energy resource can increase energy security.

• In many developing areas of the world, the electrical distribution infrastructure needed to provide users with electricity does not exist. The infrastructure requires a large amount of resources and can be expensive. Often, large diesel generators are used to provide electricity in areas with no infrastructure, but this too can be expensive because of fuel requirements and maintenance costs. In these cases, if a significant renewable resource is available, renewable energy systems are a viable alternative.

Most important disadvantages:

• Intermittent operation. Because of the resources from which renewable energy is derived, demand loads cannot be met with a high degree of reliability. Energy storage becomes necessary to achieve a high degree of reliability and this storage can be very costly and inefficient. If renewable energy is ever to compete with conventional, fossil fuel based electricity generation, this problem will need to be addressed.

• Grid stability. Some authors have found that if wind penetration exceeds maximum grid demand by 20–30% then grid stability becomes an issue. Utilization of some form of energy storage will be necessary if higher grid penetration levels are going to be achieved. In this way, energy can be stored when production levels are high and released to the grid later, thereby improving capacity utilization and the economics of the renewable energy system.

• High initial capital costs. As a result of the high initial capital costs of renewable energy systems, smart energy management must be employed to minimize the cost of electricity over the life of the system.” [2]

These problems are driving the development of some solutions that usually rely on the storage of the energy produced in surplus, especially from solar, wind, waves and tidal, in some type of storage medium or energy carriers. The most common energy carriers have been water in pumped-storage hydroelectrics, electrochemical energy in rechargeable batteries, electrostatic fields in supercapacitors and hydrogen in hydrogen hybrid systems.

The storage of the energy produced from wind in Portugal is already becoming an underlying issue. It is possible to conclude from Figure 4 that the fraction of electricity produced from wind of the total production of electricity in Portugal in 2013 was 21%, already inside the 20-30% interval mentioned above. It is also possible to observe in Figure 5 that there was a progressive increase of the

electricity fraction produced from wind since 2005, at around 3% per year. Based on the data available, it is possible to predict an electricity fraction produced from wind of 30% by 2018.

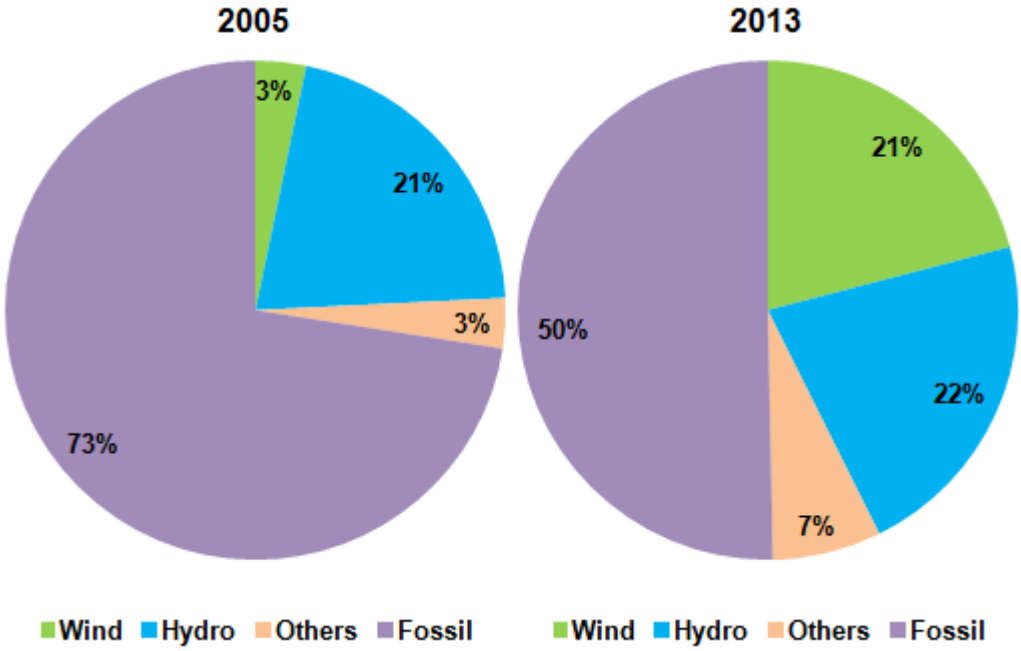

Figure 4: Weight of renewables on the production of electricity in Portugal in 2005 and 2013 [3].

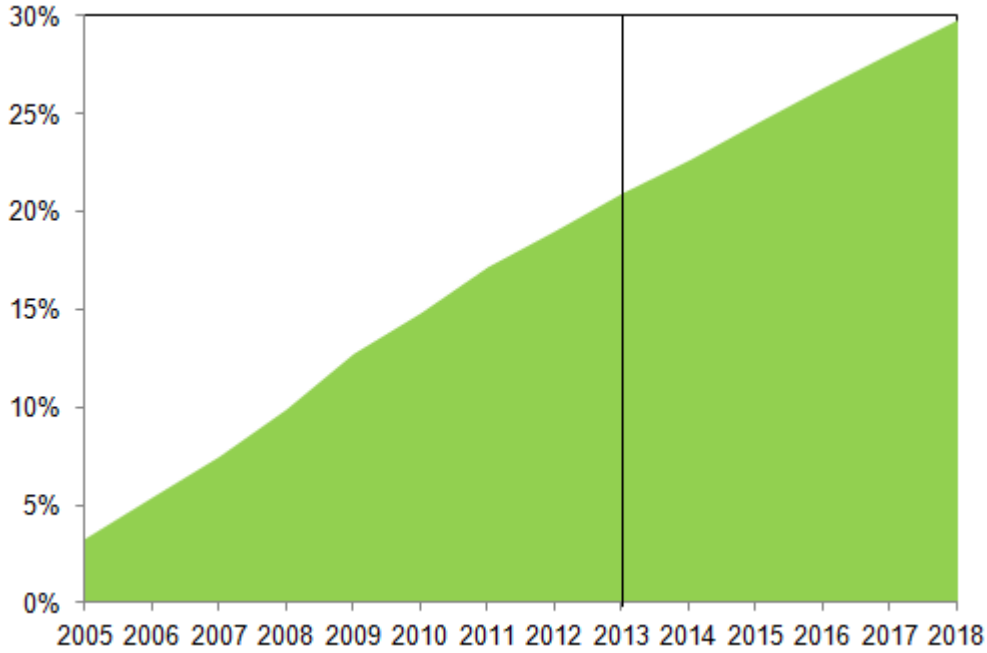

Figure 5: Evolution of wind power in Portugal from 2005 to 2013 [3] and estimate until 2018.

It is also known that in recent years there was an investment effort in pump-storage hydroelectric, but that investment is only able to avoid the waste of electricity produced from hydro, being unable to help in the storage of the electricity produced from wind power. In the end the surplus of

electricity produced at night from wind in Portugal is being sold to Spain at lower prices than it is bought back during the day.

Thus, more investment needs to be done to avoid the loss of income for Portugal, not only from the production side but also from the storage point of view. So, it makes sense to invest in research and development (R&D) of more than just one alternative for energy storage technology, besides the ones already implemented (pump-storage hydroelectric). As mentioned above, these alternatives could be rechargeable batteries, supercapacitors or hydrogen hybrid systems. In addition, the replacement of internal combustion engine vehicles with plug-in electric vehicles, that have no tailpipe emissions, such as battery electric vehicles, corresponds to an essential part of a new energy cycle in order to control CO_2 emissions, local air pollution and ensure energy security.

1.3. Lithium-air batteries

The design of new batteries for automotive application has been a very active research area, with initial focus on the improvement of safety and reliability at high power utilization [4]-[6]. Note that high power utilization results in greater polarization and resistance, which generates heat with the passage of current [4]-[6]. This generated heat needs careful thermal management in order to prevent thermal runaway as well as to maintain battery pack performance and longevity. Most importantly, the attainment of a high energy density has been noted to be the critical factor limiting the future success of battery design for automotive application.

To help explain this further, Figure 6 displays the Ragone plot of some typical primary and secondary batteries while Figure 7 compares volumetric with the gravimetric energy density for the main types of commercially available rechargeable batteries. One can observe that, rechargeable lithium ion batteries (LIB) or lithium-ion polymer batteries (LIPB) offer the best compromise between a high energy density and high power density, as well as the best compromise between a high volumetric energy density and gravimetric energy density. For this reason, these batteries have traditionally been the batteries of choice for automotive application, allowing greater capacity than the other commercially available technologies for the same size and weight, or the same capacity with reduced size and weight. Nonetheless, the current maximum energy density of these batteries is less than 200Wh.kg^{-1}, Figure 6 and Figure 7. When one compares this value to the energy density of the gasoline/air internal combustion engine (11860Wh.kg^{-1}), one immediately realizes there is a huge shortfall in energy density of current lithium-ion batteries [5]. This means that the driving range of an electric vehicle will be much shorter than that of a vehicle with a gasoline/air engine. Hence, the current goal for battery development for automobile application is to produce a battery with an energy density higher than 700Wh.kg^{-1} [7],[8]. In this respect, one should note that lithium-air batteries offer an extremely high energy density that far exceeds that of the LIB and LIPB technologies, Figure 6, despite the fact that the achieved power densities, to date, have been slightly lower. Thus, the study of Li-air batteries is a research field with great potential.

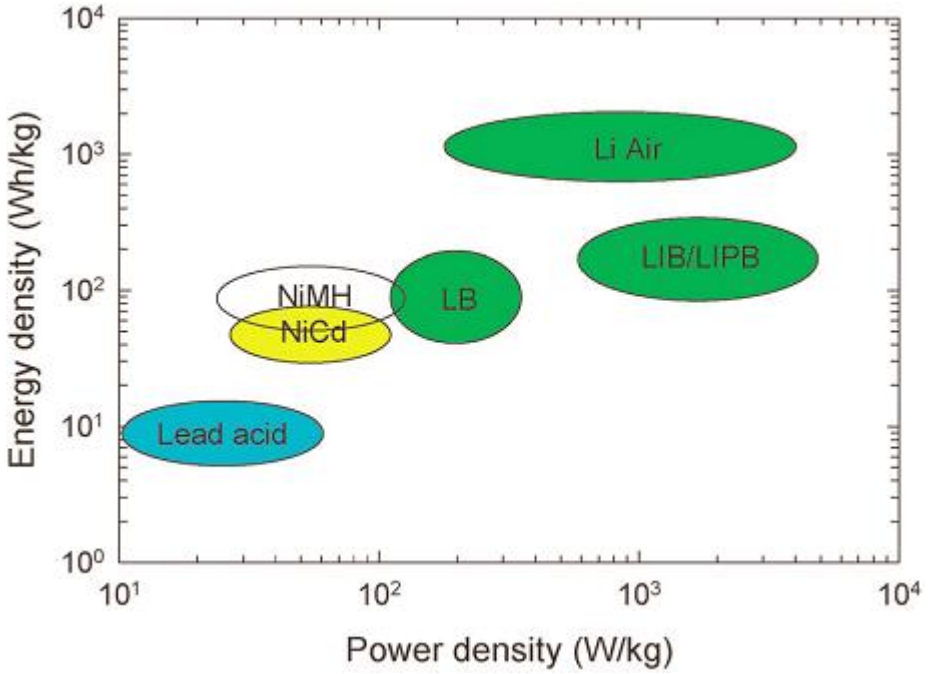

Figure 6: Ragone plot of some primary and secondary batteries, highlighting the much higher energy density of Li-air batteries [5].

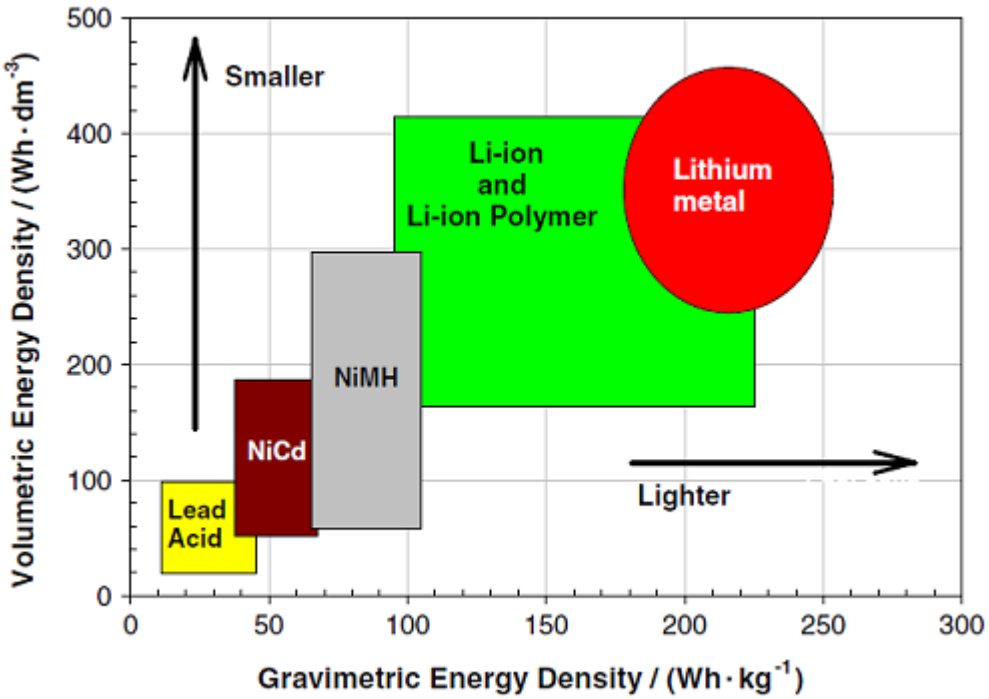

Figure 7: Comparison between the volumetric and gravimetric energy densities for the main types of secondary batteries [9].

Typical rechargeable lithium-ion batteries are comprised of a positive electrode formed from an intercalation compound, classically $LiCoO_2$, and a graphite negative electrode, similar to the schematics shown in Figure 8.

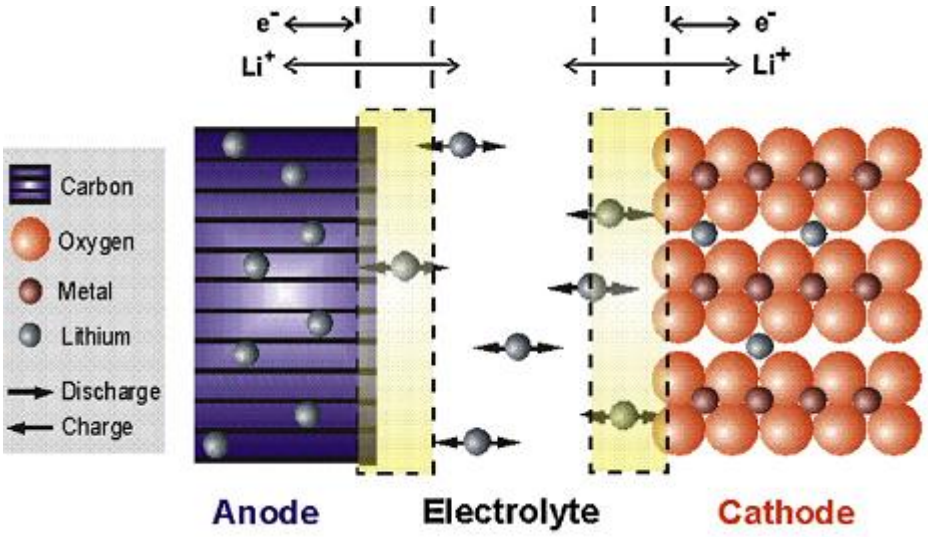

Figure 8: Schematics of a unit cell of a lithium-ion battery [4].

Li is removed from the $LiCoO_2$ electrode during the charging cycle, carried across the electrolyte, and finally inserted between the graphene layers in the graphite anode. The discharge cycle reverses the process. The limitations of energy storage come mostly from the positive electrode, which stores only 130-150mA.h.g^{-1} of charge compared with 300mA.h.g^{-1} for graphite [10]. For this reason, a high amount of scientific effort has been invested to improve the performance of the positive electrode. Nonetheless, the large effort by researchers worldwide to design and synthesize new intercalation electrodes is unlikely to yield a substantial improvement in energy density. This is because insertion reactions are limited to a maximum of one electron transfer per transition metal, a fact that greatly limits the specific energy obtainable from Li-ion intercalation batteries, e.g. $xLi + MX_y \leftrightarrow Li_xMX_y$. Hence, radical changes in the fundamental electrochemical process are needed in order to significantly increase performance. Recently, a completely different approach has been suggested that removes the necessity of a positive intercalation electrode, reacting lithium directly with O_2 from the air. This describes the so-called Li-air battery, Figure 9. Lithium reacts directly with oxygen from the air following the equation, $2Li + O_2 \leftrightarrow Li_2O_2$. As all reactants do not have to be carried on-board, very high energy densities can theoretically be obtained with values 5-10 times greater than that in LIBs or LIPBs.

The current limitations of these devices are those related to the diffusion of water and oxygen from air through the electrolyte and the subsequent damage of the lithium metal anode. Significant performance drops have been noted, even when attempts are made to prevent moisture intrusion by use of hydrophobic membranes. Hence, the stability of the lithium metal anode is the key point of current investigation on of these devices. The coating of the lithium metal anode in Li-air batteries by water stable lithium ion conducting solid electrolytes, as separators, has been suggested to prevent damage by atmospheric moisture and oxygen [7],[8][11]. Such lithium-ion conducting solid electrolytes would also find application in all-solid state Li-ion batteries.

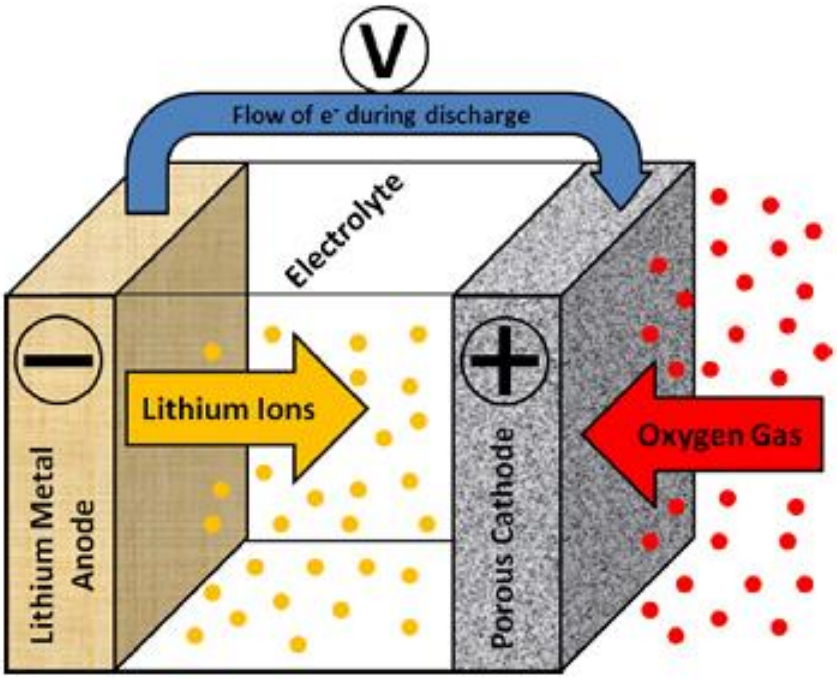

Figure 9: Schematics of a lithium-air secondary battery [12].

1.3.1. Solid electrolytes

According to Quartarone *et al* [5], the electrolyte is the main component that determines the power density, the time stability, and the safety of a rechargeable battery. As the electrolyte is in intimate contact with the electrodic compartments, a good chemical and physical compatibility with both the electrodes is required in order to obtain a stable electrified interface (EI) and, consequently, energy and power density values stabilised with time [5]. Four types of electrolytes can be used in lithium-air batteries, as illustrated in Figure 10. They are aqueous electrolyte; Non-aqueous electrolyte; mixed electrolyte, which consists of using an aqueous electrolyte at the cathode and a non-aqueous electrolyte at the anode; and solid electrolyte.

During the last twenty years research efforts have been focused on the search for alternative electrolytes for lithium batteries. One of the approaches is the fabrication of all solid-state batteries. The main reason to use a solid material is that the problems related to the management of a liquid medium are overcome [5]. With all solid-state lithium batteries being expected to offer major advantages comparatively to the commonly used polymer/gel batteries, namely: thermal stability, absence of leakage and pollution, resistance to shocks and vibrations, and a wider electrochemical window for practical applications [13].

The materials that can be used as solid lithium-ion conductors must meet the following characteristics: (a) high lithium ion conductivity at operating temperature (preferably at room temperature); (b) negligibly small or nonexistent grain-boundary resistance; (c) negligible electronic conductivity in operation conditions; (d) stability against chemical reaction with both electrodes; (e) matching thermal expansion coefficients of the electrolyte with both electrodes; (f) high electrochemical decomposition voltage [13]. In this context, different types of materials as been

investigated as potential solid-state lithium ion conductors, namely: (i) perovskite-type oxides, as (Li,La)TiO_3 based materials (called in this dissertation LLTO); (ii) garnet-type structures as $Li_5La_3M_2O_{12}$ (M = transition metal); (iii) sodium super ionic conductor (NASICON)-structured lithium electrolytes, e.g. $LiM_2(PO_4)_3$ (M = Ti, Zr, Ge); and (iv) glassy and glass-ceramic electrolytes, based on lithium nitrides, sulphides, borates and phosphates [5].

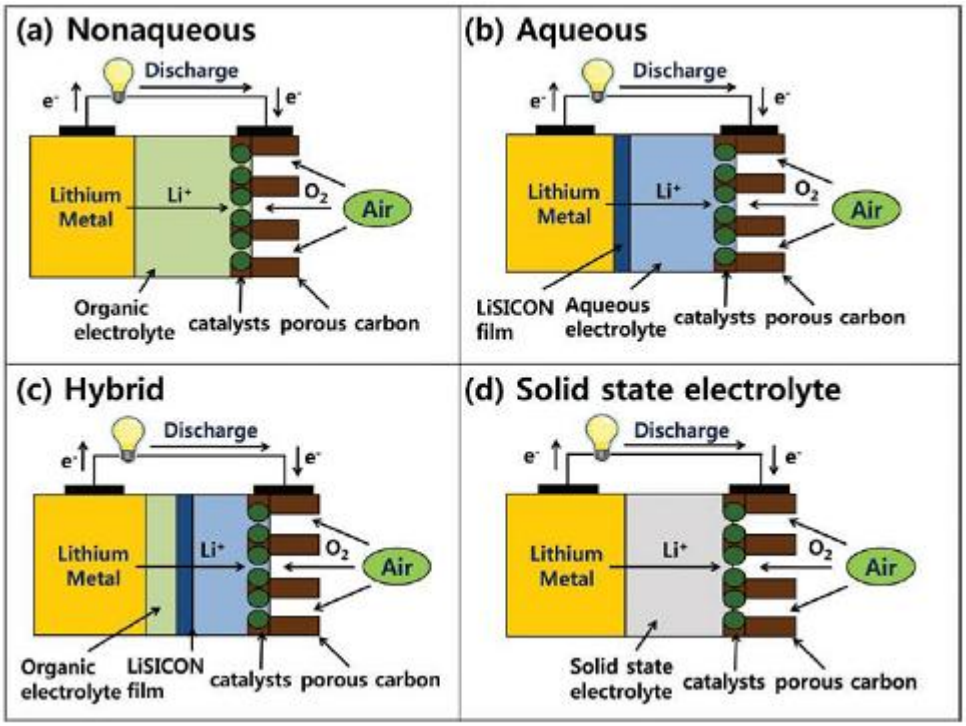

Figure 10: Schematics of lithium-air secondary batteries according to electrolyte type: (a) non-aqueous electrolytes; (b) aqueous electrolytes; (c) mixed electrolytes; (d) solid electrolytes.

The focus of this group has been in research of materials for hydrogen storage and fuel cells, mainly based on ceramic materials [14]-[18]. In this work, this experience in solid state chemistry was extended by the preparation of two different types of ceramics with good reported ionic conduction of lithium ions, a perovskite-type oxide [13],[19], and a NASICON-structured lithium electrolyte [20]. Being that the majority of the methods used to synthesize and characterise any of these ceramic materials are the same or very similar.

Chapter 2 – Mechanochemical processing of a solid lithium conductor with perovskite structure (LLTO)

Abstract

Different combinations of precursors were used to prepare $La_{0.5}Li_{0.5}TiO_3$ via mechanosynthesis. Despite the ability to produce the perovskite phase by mechanosynthesis, it was not possible to obtain a phase pure material. Of all the seven combinations of precursors and conditions tested, the one where La_2O_3, Li_2CO_3 and TiO_2 were milled for 480min (LaOLiCO-480) showed the best results, with some trace impurity phases still being observed (22.84% after mechanosynthesis and 4.20% after calcination).

2.1. Introduction

All solid-state lithium batteries are expected to offer major advantages comparatively to the commonly used polymer/gel batteries, namely: thermal stability, absence of leakage and pollution, resistance to shocks and vibrations, and a wider electrochemical window for practical applications [13]. The materials that can be used as solid lithium-ion conductors must meet the characteristics listed in section 1.3.1, along with the list of different types of materials that have been investigated as potential solid-state lithium ion conductors [13],[5].

In the search for an all solid-state lithium batteries, the perovskite-type structure (ABO_3 in Figure 11), lithium lanthanum titanate compounds ($Li_{3x}La_{2/3-x}TiO_3$) have appeared as strong candidates to be used as lithium-solid electrolytes or as cathode materials due to higher lithium ionic conductivity, between 10^{-3} and 10^{-4} $S.cm^{-1}$ for the crystal grain [19], compared with other lithium ion conductors. However, the application of lithium lanthanum titanates (LLTO) as electrolyte materials is still limited, mainly due to its low grain-boundary conductivity ($<10^{-4}$ $S.cm^{-1}$) and the instability in direct contact with metallic lithium anodes with increase in electronic conductivity [21]. To overcome the instability in Li-excess environments the use of Li alloy electrodes to reduce the activity of lithium has been considered [21].

The lower values of grain boundary conductivity reported to be exhibited by these materials have been associated with compositional and microstructural effects [22]. In theory, it should be possible to minimize the influence of grain boundary conductivity by increasing the sintering temperature, because the higher the sintering temperature, the higher the apparent grain boundary conductivity due to a larger grain size and thus smaller grain boundary area [22]. However, taking into account that LLTO materials are subject to lithium volatilization at sintering temperatures above 1100ºC, it is expected that substantial compositional changes would occur when elevated sintering temperatures are employed [22]. Despite the lithium loss issues, it is possible to obtain samples nearly fully dense after sintering at 1200ºC or above by conventional solid state synthesis, and the apparent grain boundary conductivity of these materials has been shown to increase rapidly with sintering temperature due to an increased grain size [22]. Nonetheless, besides lithium volatilization, segregation of secondary phases in grain boundaries or compositional inhomogeneity between grain and grain boundary may derive from a high temperature and long-time of sintering [23], contributing to higher grain boundary resistances in these materials.

In order to increase the grain-boundary conductivity some attempts have also been performed to promote the densification and grain growth by the control of Li content and the presence of La/Li site vacancies [19]. Mei *et al* [24] reported that it is possible to increase the grain-boundary conductivity by introducing silica, increasing the total conductivity of the LLTO ceramics to as high as $8.9\times^{-4}$ $S.cm^{-1}$, at room temperature. This idea was going to be incorporated into the present work, by introducing the silica using mechanochemical processing. But taking into account the inability to produce pure LLTO materials using mechanochemical processing, as described below, this idea had to be abandoned.

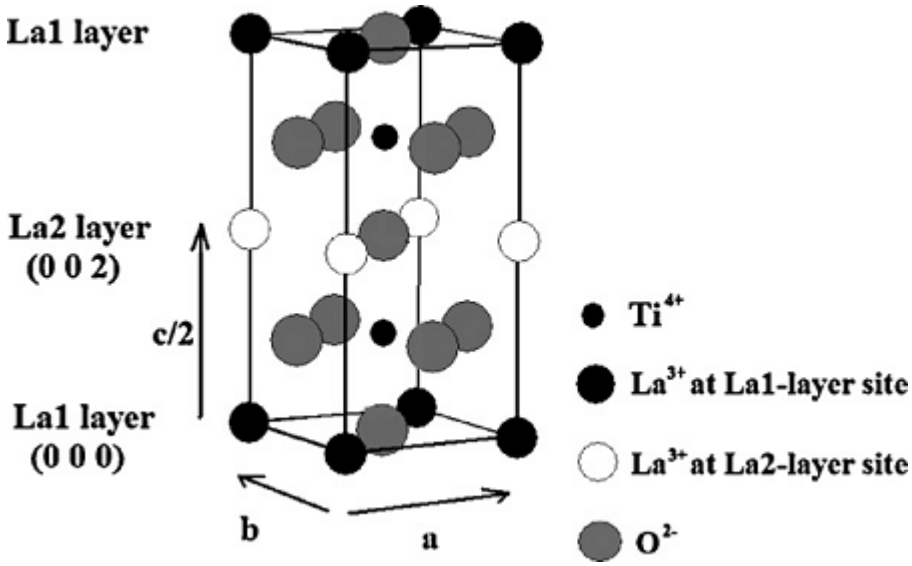

Figure 11: Crystal structure of $Li_{3x}La_{2/3-x}TiO_3$. The perovskite structure (ABO_3) is occupied by La^{3+}, Li^{+}, and vacancies at A-sites, by Ti^{4+} at B-sites, and by O^{2-} at O-sites [19].

Based on the bibliographic review done before starting this work, it was decided to use mechanochemical processing (often called mechanosynthesis) to synthesize LLTO. This would be a new technique for the preparation of these materials that could offer potential advantages over other synthesis methods that have been used so far, including conventional solid state reaction, sol–gel method, pulsed laser deposition and microwave sintering methods [25]. It is noteworthy, that the most commonly used method has been the conventional solid state reaction, with sintering temperatures of around 1350ºC and long sintering times (several hours) [25]. By choosing mechanochemical processing for the synthesis of LLTO, our goal was to make mechanosynthesised powders due to their high activity, nanometric particle size and, thus, good densification [26]. By doing this, we aimed to lower the required sintering temperature to minimize lithium loss due to volatilization, which otherwise would lead to the presence of impurities or compositional inhomogeneity at the grain boundaries that have been shown to lead to low grain boundary conductivities and, hence, low total conductivities [19],[21],[22],[23].

In recent years, mechanochemistry has become a research topic of increasing activity for the formation of materials, motivated by a surge of interest in the preparation of nano-powders. The structural supersaturation by vacancies and chemical non-uniformity of mechanochemical powders promote enhanced sinterability, while the high density of aggregates and reduced crystallite density produce high green-densities. Such factors are highly attractive for preparation of dense ceramic-

oxide materials, as required for the formation of Li-solid electrolytes. Additionally, mechanochemical ceramic processing may allow the synthesis of novel materials, which cannot be synthesized by other methods.

Mechanochemical synthesis occurs at interparticle contacts. The small impact area between solid particles concentrates the relatively low mechanical energy, giving rise to local changes in physical parameters, such as temperature and pressure, and the progression of chemical interaction. The primary mechanochemical event can be described by Equation 1 [27]:

$$A + B \rightarrow (A_xB)^* \rightarrow A_{1-\delta}B^* + B^* \qquad \text{Equation 1}$$

Where $(A_xB)^*$ defines a dynamic state, in the form of a layer grown due to a rolling mass transfer mechanism (Figure 12), A and B represent the hard and soft reactants, respectively, B* is a particular form of reactant B, with amorphous or turbostratic structure, resulting from the relaxation of dynamic state, and $A_{1-\delta}B^*$ represents the primary product, deficient in the hardest reagent [27],[28]. The composition of the dynamic state and the primary reaction product is determined by the difference in the Mohs' hardness of the oxide precursors.
During the secondary event of the mechanical alloying mechanism, there is a slow conversion of the primary product towards the final equilibrium composition by a deformation mixing regime, with the formation of rotation zones, and further mass transfer during stoppage and unloading [27],[28].

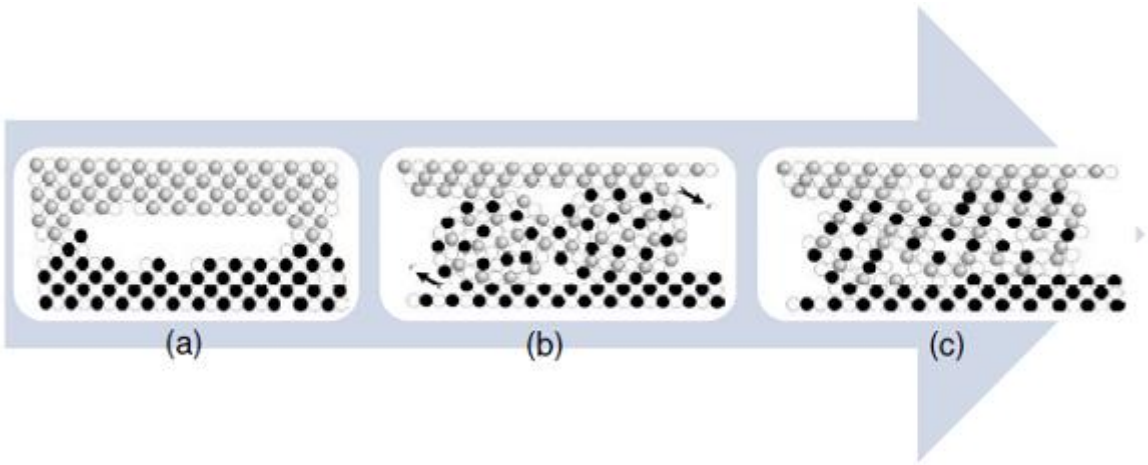

Figure 12: Two-dimensional scheme illustrating the primary event of the mechanical alloying mechanism: (a) initial state; (b) roll growth until collision, accompanied by emission processes, and (c) relaxation of (AxB)* to the primary product [27],[28].

Figure 13 describes graphically the dynamic of this process, highlighting the gradual change between reagent consumption, primary product formation and conversion to final product. One can also see that any interruption of the process before completion will lead to inhomogeneous mixtures of metastable and highly active reactants that are deficient in the hardest component. Such high-energy milling without synthesis of an overall equilibrium product is called "mechanochemical activation", and can offer distinct advantages with respect to reactivity and densification of ceramic materials [29],[30].

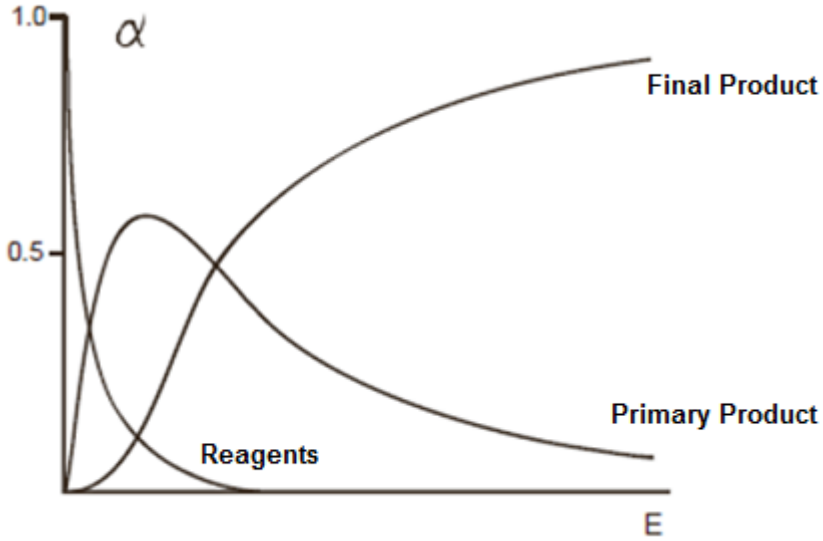

Figure 13: Dynamics of mechanosynthesis. Inter-relationship between reagents, primary product and final product concentrations with extent of milling [27],[28].

Mechanochemically produced powders often shows agglomerates up to 100 μm with low densities (65-70%), consisting of aggregates with densities up to 80% in the range 0.2-2 μm [27],[28]. These aggregates are comprised of composites of nanosized crystallites in an amorphous matrix (Figure 14).

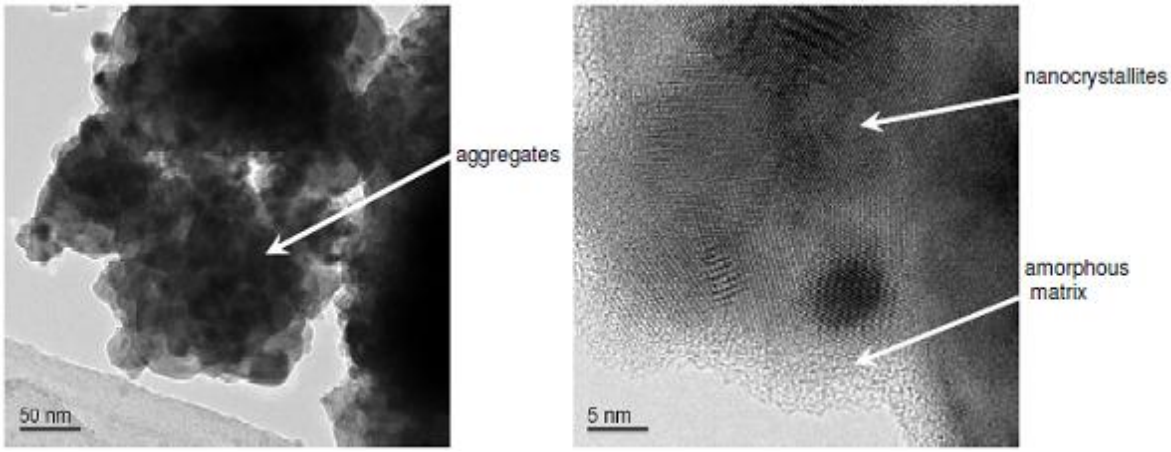

Figure 14: Mechanically produced barium titanate-based powders.

The relative amounts and compositions of these entities are defined by milling time, intensity and precursor choice. By modifying these parameters, one has the ability to refine the chemical non-uniformity of mechanochemical powders to enhance sinterability and green density [31]. The dynamics of the mechanochemical process are controlled by the molecular mass, the difference in Moh's hardness and the thermodynamic properties of the precursors [32].

Mechanosynthesis has also been a synthesis method widely spread in industry and research in the preparation of several types of materials [33], including materials with the perovskite-type structure [34]. Mechanosynthesis has also been employed in the preparation of other lithium-based oxides such as $LiMO_2$ (M=Ti, Mn, Fe, Co, Ni) [35], or $Li_4Ti_5O_{12}$ [23],[36].

As with any other method, many advantages are attributed to mechanosynthesis [33], but also a few disadvantages [37]. Besides the fact that this method is readily available, it was selected because we wanted to perform a simple, dry, time-convenient one-step syntheses, prepare nanomaterials with properties set in advance, and use a short sintering cycle with the lowest temperature possible, but keeping in mind that it is notoriously energy inefficient [37].

2.2. Experimental procedure

2.2.1. Mechanosynthesis of $La_{0.5}Li_{0.5}TiO_3$

Lithium lanthanum titanate $La_{0.5}Li_{0.5}TiO_3$ (LLTO) was prepared by mixing stoichiometric amounts of different lanthanum and lithium precursors with titanium oxide (TiO_2), Sigma-Aldrich 99.8% purity, for a total mass of 4.5g. The range of precursors used were lanthanum(III) oxide (La_2O_3), Sigma-Aldrich 99.99% purity; lanthanum hydroxide [$La(OH)_3$], Sigma-Aldrich 99.95% purity; lithium hydroxide monohydrate ($LiOH.H_2O$), Sigma-Aldrich ≥99.0% purity; lithium hydroxide (LiOH), Sigma-Aldrich 100% purity after drying; lithium carbonate (Li_2CO_3), Sigma-Aldrich ≥99.0% purity; lithium acetate dehydrate ($CH_3COOLi.2H_2O$), Sigma-Aldrich ≥97.0% purity, according to the data available on Table A 1.

The mechanosynthesis conditions were the same as described in [26]: A planetary mill, PM200 (Retsch), was used with constant planetary rotation of 650rpm using 125cm^3 tetragonal zirconia vials (Retsch) and balls (TosohCo.). The ball to powder ratio of 10:1 was used. To avoid excess heating the program was run for 5 minutes with 5 minutes intervals, reversing the direction of rotation after each interval. The progression of the reaction was followed by XRD analysis of the powder samples collected after each hour of effective mechanosynthesis, using a Rigaku Geigerflex diffractometer, (Cu$K\alpha$ radiation, step width 0.02º, scan rate 3º/min).

The precursors used for each mechanosynthesis of $La_{0.5}Li_{0.5}TiO_3$, and their masses are listed in Table 1, while the pre-treatment conditions of the precursors are listed in Table 2. The different mechanosynthesis reactions are given the acronyms; LaOLiOH.W-420 (Equation 2), LaOLiOH.W-300 (Equation 2), LaOLiOH.W-600 (Equation 2), LaOHLiOH.W-600 (Equation 3), LaOLiOH-480 (Equation 4), LaOLiCO-480 (Equation 5) and LaOLiAcetate-480 (Equation 6)], where the effective milling times are indicated by the final number and the label W indicates the presence of water of crystallisation in the precursor $LiOH.H_2O$. Each different combination of precursors followed the chemical reactions below (Equations 2–6):

$La_2O_3 + 4TiO_2 + 2LiOH.H_2O \rightarrow 4La_{0.5}Li_{0.5}TiO_3 + 3H_2O$ Equation 2

$La(OH)_3 + 2TiO2 + LiOH.H_2O \rightarrow 2La0.5Li0.5TiO3 + 3H_2O$ Equation 3

$La_2O_3 + 4TiO_2 + 2LiOH \rightarrow 4La_{0.5}Li_{0.5}TiO_3 + H_2O$ Equation 4

$La_2O_3 + 4TiO_2 + Li_2CO_3 \rightarrow 4La_{0.5}Li_{0.5}TiO_3 + CO_2$ Equation 5

$La_2O_3 + 4TiO_2 + 2CH_3COOLi.2H_2O \rightarrow 4La_{0.5}Li_{0.5}TiO_3 + 3H_2O + 2CH_3COOH$ Equation 6

Table 1: List of precursors used for each mechanosynthesis, including the effective milling time.

Mechanosynthesis	Lanthanum		Lithium		Titanium	t (min)
	precursor	m (g)	precursor	m (g)	m TiO_2 (g)	
LaOLiOH.W-420	La_2O_3	2.0119	$LiOH.H_2O$	0.5183	1.9718	420
LaOLiOH.W-300	La_2O_3	2.0108	$LiOH.H_2O$	0.5180	1.9714	300
LaOLiOH.W-600	La_2O_3	2.0128	$LiOH.H_2O$	0.5183	1.9720	600
LaOHLiOH.W-600	$La(OH)_3$	2.1826	$LiOH.H_2O$	0.4827	1.8355	600
LaOLiOH-480	La_2O_3	2.1151	LiOH	0.3109	2.0736	480
LaOLiCO-480	La_2O_3	2.0392	Li_2CO_3	0.4622	1.9986	480
LaOLiAcetate-480	La_2O_3	1.7267	$CH_3COOLi.2H_2O$	1.0814	1.6927	480

Table 2: List of heat treatments used for the precursors before the mechanosynthesis, including other mechanosynthesis conditions.

Mechanosynthesis	Lanthanum	Lithium	Titanium	Other conditions
	T (ºC)	T (ºC)	T (ºC)	
LaOLiOH.W-420	1000	200	RT	normal
LaOLiOH.W-300	1000	200	RT	vial was always closed
LaOLiOH.W-600	1000	200	RT	La_2O_3 milled for 1h at 150rpm
LaOHLiOH.W-600	RT	200	RT	changed the La precursor from La_2O_3 to $La(OH)_3$
LaOLiOH-480	1000	200	RT	LiOH was weighed after the water of crystallization of $LiOH.H_2O$ was removed by drying at 200ºC
LaOLiCO-480	1000	RT	RT	changed the Li precursor from $LiOH.H_2O$ to Li_2CO_3
LaOLiAcetate-480	1000	250	RT	changed the Li precursor from $LiOH.H_2O$ to $CH_3COOLi.2H_2O$

2.3. Results and discussion

Figure 15 shows the evolution of XRD patterns with effective milling time for the LaOLiOH.W-420 mechanosynthesis (0 to 420min). One can observe that this mechanosynthesis develops very fast up to 180min, showing no significant evolution in the phases after 240min and that the desired LLTO ($La_{0.5}Li_{0.5}TiO_3$) phase is present, along with impurity phases, mainly, La_2O_3 (PDF#01-075-2530), even after 420min.

Based on the results of mechanosynthesis LaOLiOH.W-420, it was decided to perform mechanosynthesis LaOLiOH.W-300 with a closed vial, as at the time it was thought that carbon dioxide from air could be the cause for the presence of impurities in the final powder due to the appearance of Li_2CO_3 during milling in the LaOLiOH.W-420 case. The evolution of XRD patterns with effective milling time for the LaOLiOH.W-300 mechanosynthesis is shown in Figure 16 (0 and 300min). One can observe that the desired LLTO ($La_{0.5}Li_{0.5}TiO_3$) phase is present, along with impurity phases, even after 300min in a closed vial.

Figure 16 shows that these impurity phases cannot be removed upon subsequent calcining, despite an increase in crystallinity with increasing calcining temperature. The main impurity phase

of Li_2TiO_3 suggests a deficiency of lanthanum in the final product, in agreement with the presence of La_2O_3 noted as a secondary phase in the mechanosynthesised product.

Based on the results of mechanosynthesis LaOLiOH.W-420 and LaOLiOH.W-300, it was, therefore, decided to perform two mechanosyntheses in parallel to test the influence of i) a pre-low speed milling step of the La_2O_3 precursor to mechanically activate this powder with the aim that it will increase its reactivity (LaOLiOH.W-600) and ii) to test a different lanthanum precursor, $La(OH)_3$, (LaOHLiOH.W-600). The mechanosyntheses were also run for an extended time period of 600min instead of 420min. Figure 17 and Figure 18 show the evolution of XRD patterns with effective milling time for the LaOLiOH.W-600 and LaOHLiOH.W-600 mechanosyntheses (0 to 600min). One can observe that the activated La_2O_3 powder synthesis, LaOLiOH.W-600, develops very fast up to 180min, showing no significant evolution in the phases after 240min. In contrast, LaOHLiOH.W-600 develops slower and only stops showing a significant evolution in the phases after 480min. One can also observe that the desired LLTO ($La_{0.5}Li_{0.5}TiO_3$) phase is present in both mechanosyntheses, along with impurity phases, even after 600min. Of these two syntheses the activated La_2O_3 route appears to offer the purest product.

As two vials can be used during each mechanosynthesis experiment, the next parallel runs were performed using the activated La_2O_3 powder with different Li-precursors. Firstly, to test the influence of using the precursor $LiOH.H_2O$ after removing its water of crystallization at 200ºC and secondly, to use Li_2CO_3 as the lithium precursor. Based on the previous results that no significant advantage was gained by extensive milling times, the final time was defined to be 480min. Figure 19 and Figure 20 show the evolution of XRD patterns with effective milling time for the LaOLiOH-480 and LaOLiCO-480 mechanosyntheses (0 to 480min). One can observe that LaOLiOH-480 develops very fast before 180 min, showing no significant evolution in the phases after 300 min of milling and that LaOLiCO-480 also develops very fast up to 180 min, showing no significant evolution in the phases after 240 min of milling. One can also observe that the desired LLTO ($La_{0.5}Li_{0.5}TiO_3$) phase is present in both mechanosyntheses, along with La_2O_3 impurity phases, even after 480min.

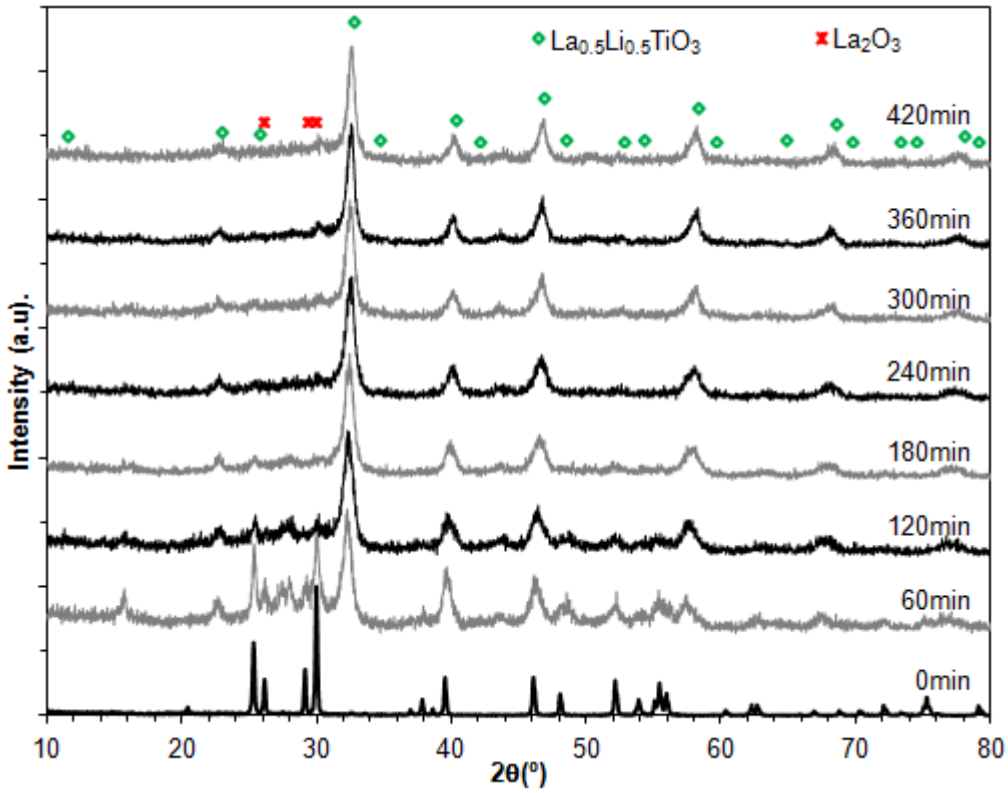

Figure 15: Evolution of powder X-ray diffraction patterns with mechanosynthesis time for LaOLiOH.W-420 with La_2O_3, $LiOH.H_2O$ and TiO_2 as precursors.

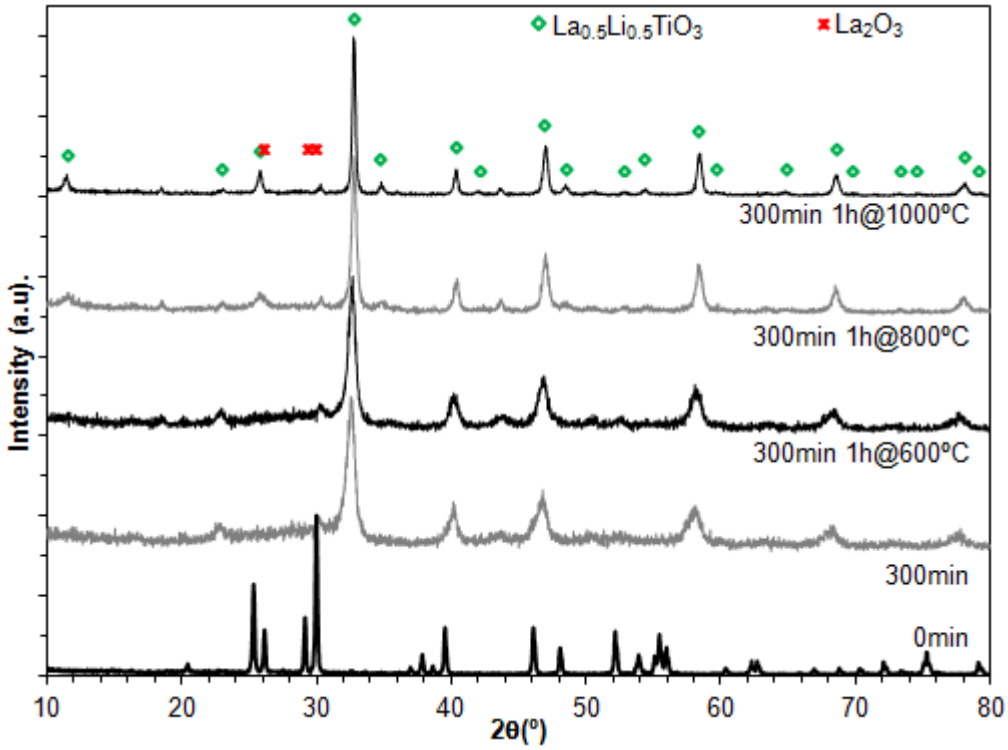

Figure 16: Evolution of powder X-ray diffraction patterns with mechanosynthesis time for LaOLiOH.W-300 with La_2O_3, $LiOH.H_2O$ and TiO_2 as precursors.

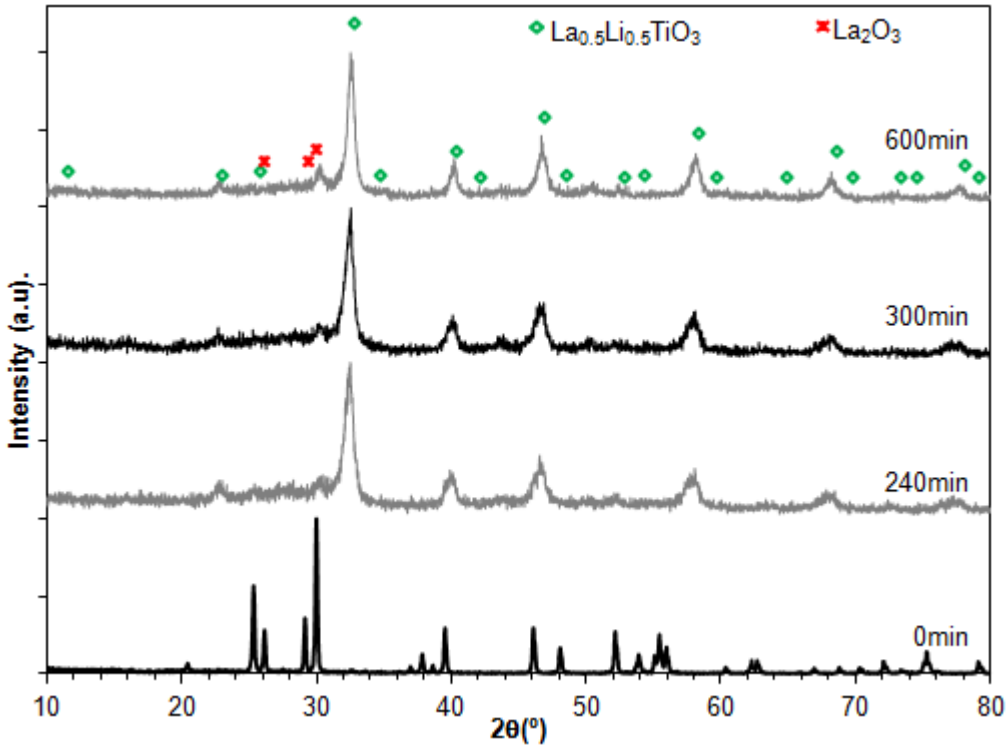

Figure 17: Evolution of powder X-ray diffraction patterns with mechanosynthesis time for LaOLiOH.W-600 with mechanically activated La_2O_3, $LiOH.H_2O$ and TiO_2 as precursors.

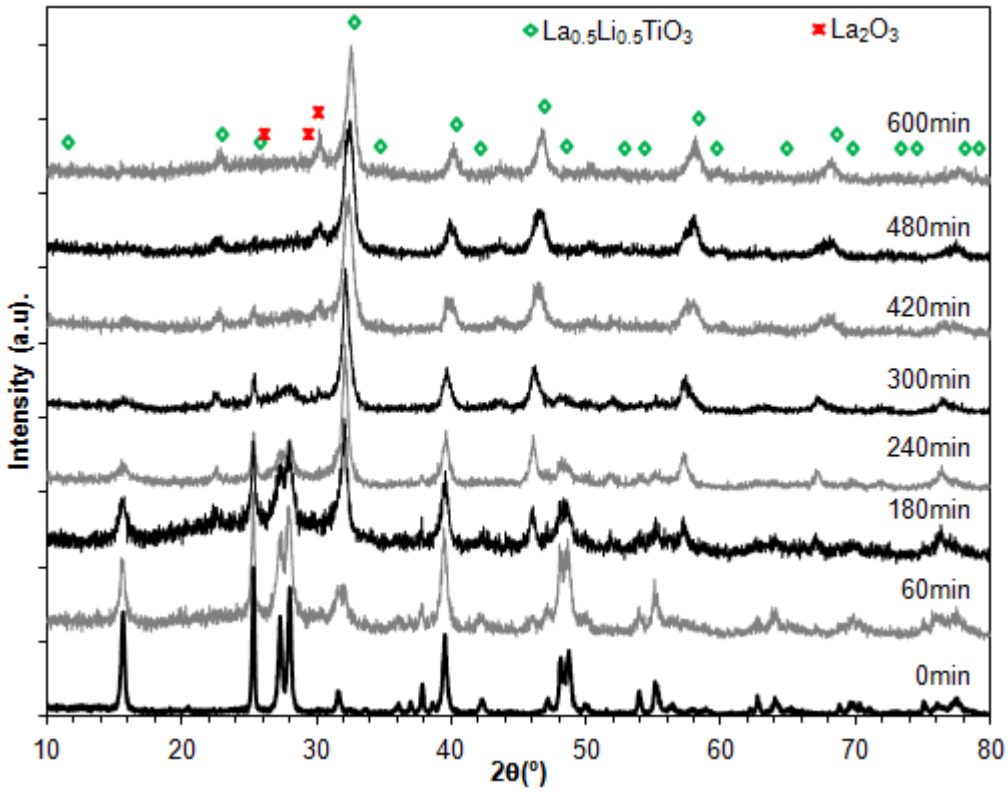

Figure 18: Evolution of powder X-ray diffraction patterns with mechanosynthesis time for LaOHLiOH.W-600 with $La(OH)_3$, $LiOH.H_2O$ and TiO_2 as precursors.

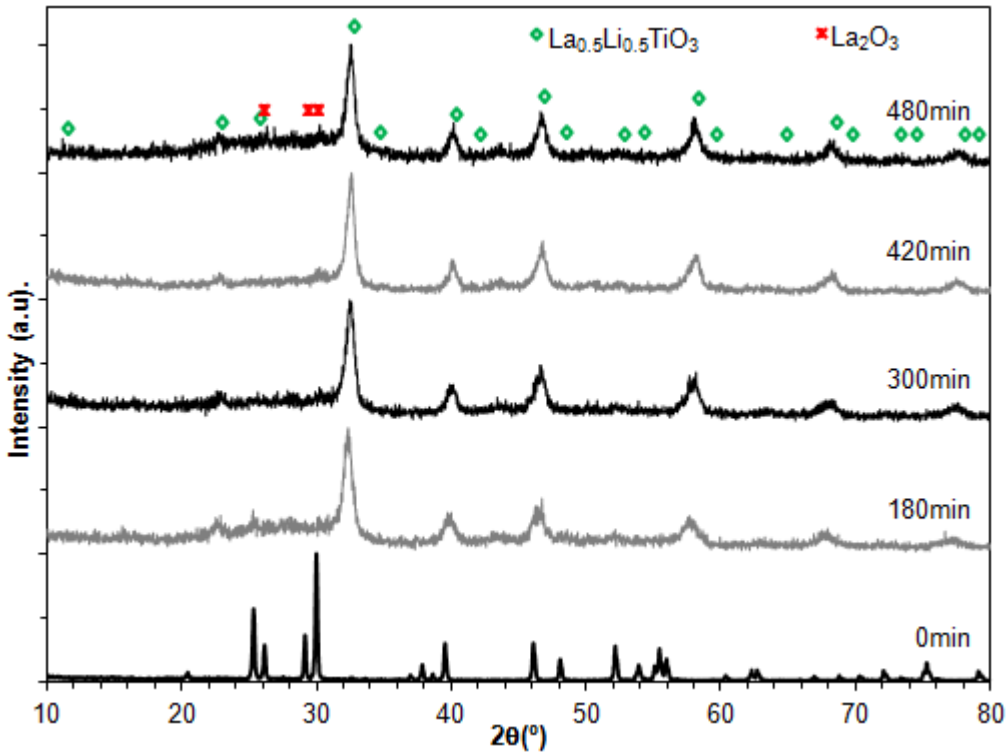

Figure 19: Evolution of powder X-ray diffraction patterns with mechanosynthesis time for LaOLiOH-480 with mechanically activated La_2O_3, LiOH and TiO_2 as precursors.

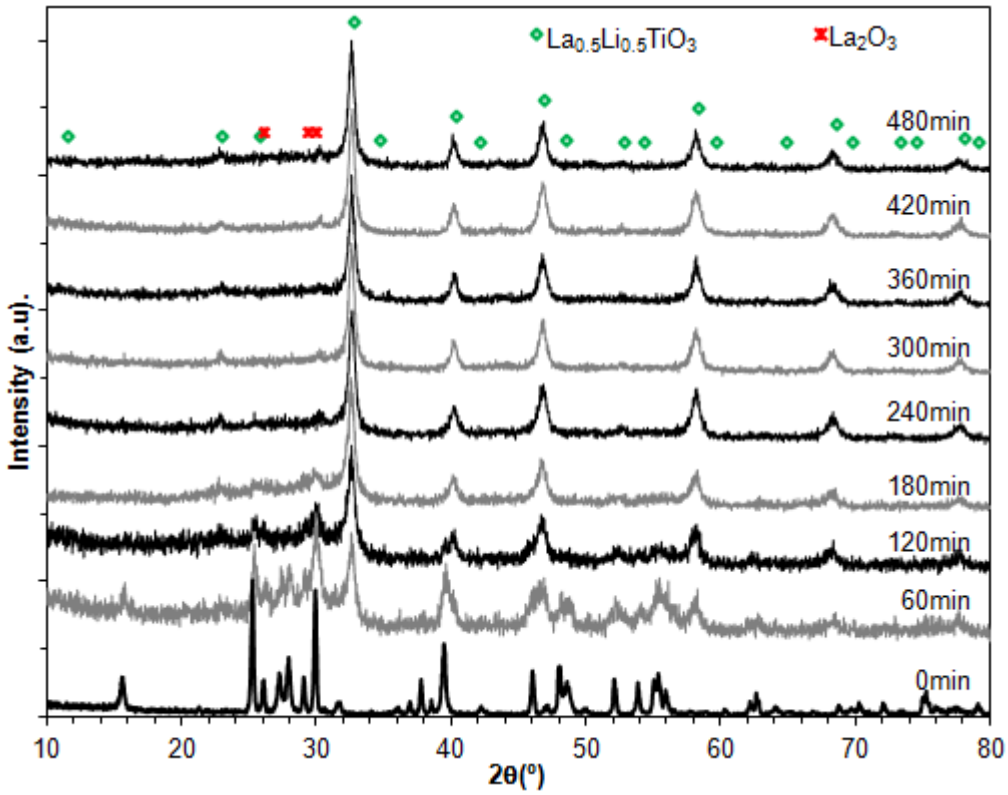

Figure 20: Evolution of powder X-ray diffraction patterns with mechanosynthesis time for LaOLiCO-480 with mechanically activated La_2O_3, Li_2CO_3 and TiO_2 as precursors.

A final mechanosynthesis was performed using $CH_3COOLi.2H_2O$ as the lithium precursor. Figure 21 shows that there was no transformation of precursors into LLTO, and only the amorphization of precursors is shown to occur. Hence the precursor $CH_3COOLi.2H_2O$ is an ineffective precursor for the mechanosynthesis of LLTO in LaOLiAcetate-480.

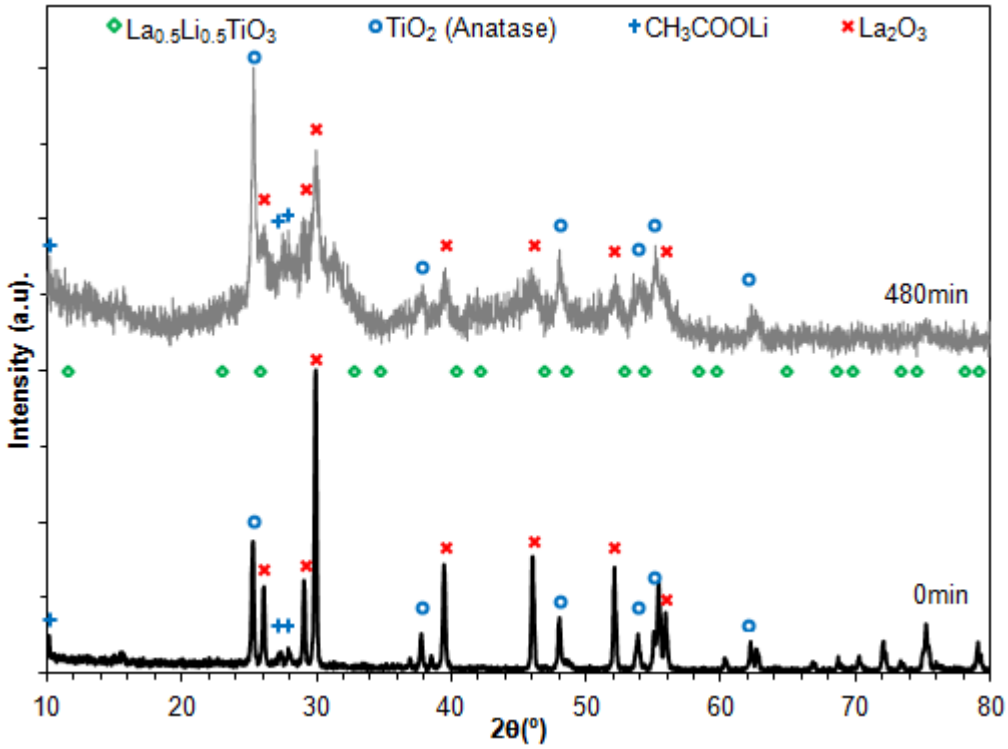

Figure 21: Evolution of powder X-ray diffraction patterns with mechanosynthesis time for LaOLiAcetate-480 with mechanically activated La_2O_3, $CH_3COOLi.2H_2O$ and TiO_2 as precursors.

By looking at Table 3 and Figure 22 one can observe which mechanosynthesis presented the best and worst levels of impurities after the duration of the mechanosynthesis, by assessment of the relative intensities of the main 110/102 peak of the desired LLTO phase (PDF#01-070-6720), at 2θ = 32.687º, and the 011 peak of the main impurity phase La_2O_3 (PDF#01-075-2530), at 2θ = 30.041º. LaOLiCO-480 is the mechanosynthesis with the least impurity peaks (22.84%). LaOLiAcetate-480 is the one with the most impurity peaks (100%), because there was no transformation of reagents into LLTO, as explained above.

Table 3: Comparison of the size of the relative intensities of the impurities peaks after mechanosynthesis.

	LLTO			Impurities				
Mechanosynthesis	**2θ (º)**	**hkl**	**I (a.u.)**	**Impurity**	**2θ (º)**	**hkl**	**I (a.u.)**	**%**
LaOLiCO-480	32.687	110/102	845	La_2O_3	30.041	011	193	22.84
LaOLiOH.W-300	32.687	110/102	815	La_2O_3	30.041	011	200	24.54
LaOLiOH.W-600	32.687	110/102	985	La_2O_3	30.041	011	278	28.22
LaOLiOH.W-420	32.687	110/102	685	La_2O_3	30.041	011	213	31.09
LaOLiOH-480	32.687	110/102	595	La_2O_3	30.041	011	225	37.82
LaOHLiOH.W-600	32.687	110/102	663	La_2O_3	30.041	011	288	43.44
LaOLiAcetate-480	25.281	n.a.	n.a.	TiO_2	25.281	101	540	100.00

From Figure 22 one can also observe that, for every tested mechanosyntheses, the LLTO peaks are somewhat broad, suggesting fine particle size, and the final powder presents low levels of crystallinity. This is easier to observe when one compares the mechanosynthesis results in Figure 22 with results after calcination at 1000ºC for 1h in Figure 23.

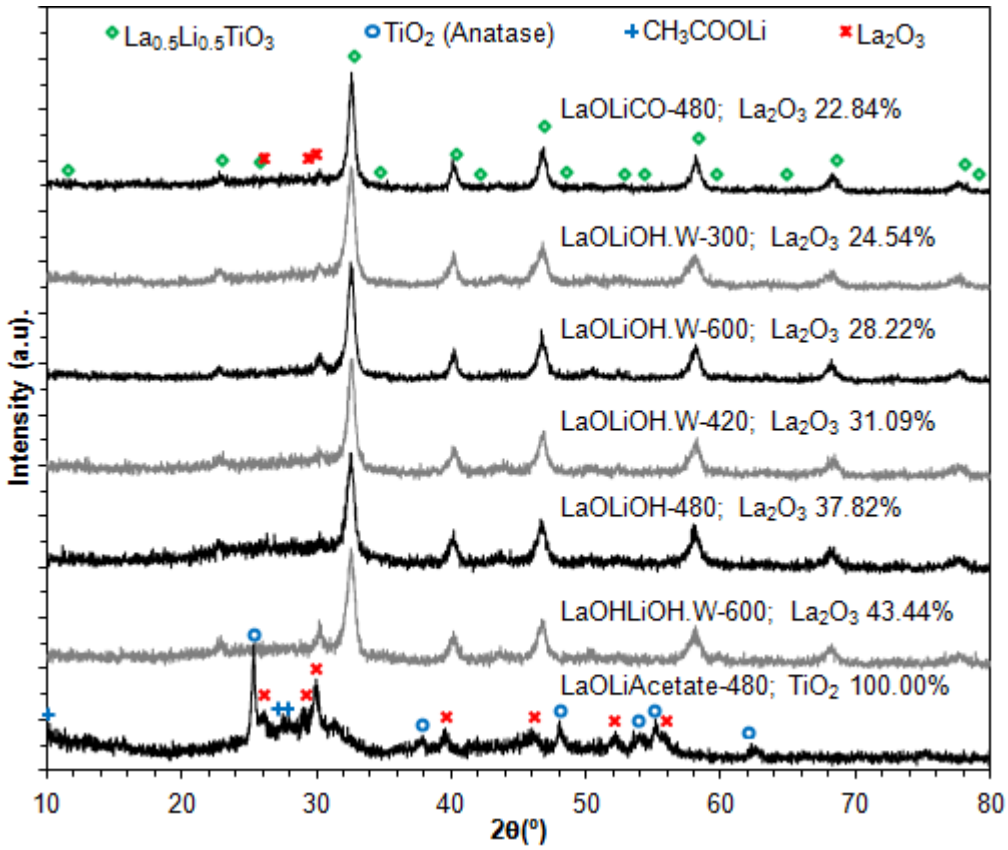

Figure 22: XRD spectra of the final powder for the mechanosyntheses LaOLiCO-480, LaOLiOH.W-300, LaOLiOH.W-600, LaOLiOH.W-420, LaOLiOH-480, LaOHLiOH.W-600 and LaOLiAcetate-480, from the top to the bottom.

By looking at Table 4 and Figure 23 one can observe which final powder presented the least impurities after calcination, by assessment of the relative intensities of the main 110/102 peak of the desired LLTO phase (PDF#01-070-6720), at 2θ = 32.687º, and the 002 peak of the main impurity phase Li_2TiO_3 (PDF#01-071-2348), at 2θ = 18.510º. Mechanosynthesis LaOLiCO-480 is the one the least impurity peaks (4.20%), while LaOLiOH.W-300 is the one with the most impurity peaks (8.50%).

Table 4: Comparison of the biggest impurities peak with the biggest peak of the LLTO phase after calcination.

	LLTO			Impurities				
Mechanosynthesis	**2θ (º)**	**hkl**	**I (a.u.)**	**Impurity**	**2 (º)**	**hkl**	**I (a.u.)**	**%**
LaOLiCO-480	32.687	110/102	4473	Li_2TiO_3	18.510	002	188	4.20
LaOLiAcetate-480	32.687	110/102	2850	Li_2TiO_3	18.510	002	170	5.96
LaOHLiOH.W-600	32.687	110/102	4080	Li_2TiO_3	18.510	002	248	6.08
LaOLiOH-480	32.687	110/102	3180	Li_2TiO_3	18.510	002	223	7.01
LaOLiOH.W-600	32.687	110/102	3955	Li_2TiO_3	18.510	002	303	7.66
LaOLiOH.W-300	32.687	110/102	2448	Li_2TiO_3	18.510	002	208	8.50

The XRD data of the final powders after calcination at 1000ºC for 1h, for each of the milling cycles listed in Table 1, are represented in Figure 23. Here one can observe that even after calcination for every mechanosyntheses tested the desired LLTO ($La_{0.5}Li_{0.5}TiO_3$) phase is present, along with minor impurity phases. In the case of mechanosyntheses LaOLiOH.W-300, LaOLiOH.W-600, LaOHLiOH.W-600, LaOLiOH-480, LaOLiCO-480 and LaOLiAcetate-480 the impurities were Li_2TiO_3 (PDF#01-071-2348) and La_2O_3 (PDF#01-075-2530).

After calcination, for every mechanosyntheses, the final powder of LLTO shows sharp peaks in the XRD pattern, indicating a high crystallinity level, even after a short calcination cycle at 1000ºC for 1h. Note that the perovskite phase is now formed after calcination of the Li-acetate derived precursor powder, LaOLiAcetate-480. In this case it is possible that the milling increased the reactivity of the precursors before the calcination cycle even though the LLTO phase could not be formed during milling. However, in all cases a pure LLTO phase was never achieved.

Mechanosynthesis LaOLiCO-480, using La_2O_3, Li_2CO_3 and TiO_2 as precursors, presents the best results from all the conditions studied, however small impurity peaks are still observed even after calcination, of lithium titanium oxide (Li_2TiO_3, PDF#01-071-2348) and La_2O_3 (PDF#01-075-2530), as seen in Figure 23, Figure 24 and Table 4.

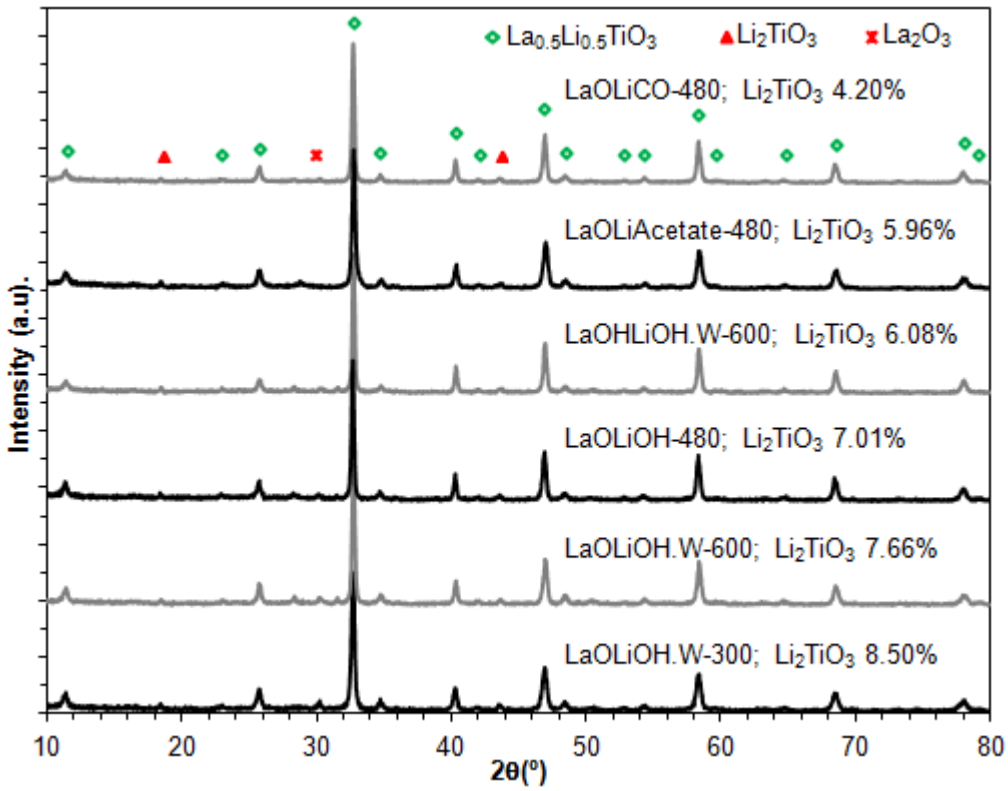

Figure 23: XRD spectra of the final powder for the mechanosyntheses LaOLiCO-480, LaOLiAcetate-480, LaOHLiOH.W-600, LaOLiOH-480, LaOLiOH.W-600 and LaOLiOH.W-300, after calcination at 1000ºC for 1h.

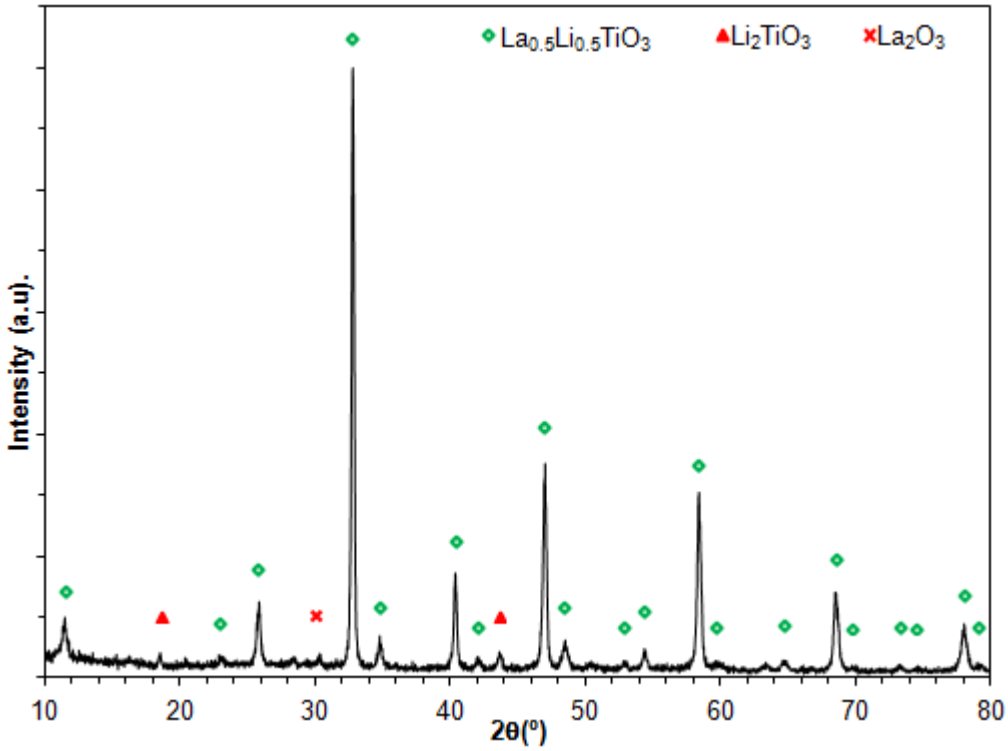

Figure 24: XRD pattern for the mechanosynthesis LaOLiCO-480 after 480min, after calcination at 1000ºC for 1h.

2.4. Conclusions

Results showed that it is not possible to obtain a pure LLTO phase through mechanosynthesis using the conditions of the current experiments and the seven precursors combinations studied. However, the results showed that mechanosynthesis can produce the perovskite phase. Moreover, the temperature and time needed to achieve a crystalline LLTO phase is shown to be decreased to 1000ºC for 1h for the mechanochemically derived powders, when compared to the conventional solid state reaction, which typically need around 1350ºC for more than 1h [25].

Of all the seven combinations of precursors and conditions tested, the one where La_2O_3 was pre-mechanically activated and subsequently milled with Li_2CO_3 and TiO_2 precursors for 480min (LaOLiCO-480) showed the best results, with trace impurity phases still being observed (22.84% after mechanosynthesis and 4.20% after calcination).

The presence of La_2O_3 as the major impurity phase in each mechanosyntheses suggests that the final product will be deficient in lanthanum, thereby forming the phase Li_2TiO_3 on calcination. Such lanthanum deficiency is probably due to the low activity of the La-precursors even when La_2O_3 is previously mechanical activated or when the La_2O_3 precursor is replaced for $La(OH)_3$. Simple alteration of precursors, as performed in the current study, is shown to be unable to counteract lanthanum deficiency and the formation of the Li_2TiO_3 impurity phase on calcination. As phase purity was not obtained under the current conditions, it was not possible to further analyze and modify the LLTO prepared by mechanosynthesis. It is thought that only by more aggressive milling, for example, higher rotational velocities or by different ball/powder ratios can a pure phase be possibly formed. Alternatively, more aggressive mechanical activation conditions of the La_2O_3 precursor may also be considered. These suggestions would be the goal of future studies.

Chapter 3 – Sol-gel synthesis of a solid lithium conductor (LZP)

Abstract

Two different sol-gel methods were used to attempt to dope boron on either the Zr-site or the P-site of $LiZr_2B(PO_4)_3$, with the doping being achieved using a method adapted from Alamo *et al*. The results show that the Zr-site is the preferential mechanism for boron doping of $LiZr_2(PO_4)_3$ and not the P-site. Rietveld refinement of the unit-cell parameters was performed and by assessment of Vegard's Law it was verified that it is possible to obtain phase purity up to x = 0.05. These results confirm the XRD data obtained for the powder samples sintered at 1200ºC for 12h, where the monoclinic phase (PDF#01-070-5819) was detected for compositions with values of $x \geq 0.075$. XRD experiments performed as a function of temperature showed that compositions inside the solid solution undergo the phase transition from triclinic (PDF#01-074-2562) to rhombohedral (PDF#01-070-6734) when heated from 25ºC to 100ºC, as is reported in the literature. Despite many efforts, it was found to be difficult to obtain dense pellets of $LiZr_2(PO_4)_3$ and $Li_{1.05}Zr_{1.95}B_{0.05}(PO_4)_3$ under typical sintering conditions, hence, further densification studies are required before electrochemical characterization can be performed.

3.1. Introduction

The coating of the lithium metal anode in Li-air batteries by water stable lithium ion conducting solid electrolytes, as separators, has been suggested to prevent damage by atmospheric moisture and oxygen [7],[8],[11]. Such lithium-ion conducting solid electrolytes would also find application in all-solid state Li-ion batteries. These solid materials ideally should offer Li-ion conduction greater than $10^{-4}S.cm^{-1}$ at room temperature [38]. Nowadays, the best commercially available solid Li-electrolyte is that of $Li_{1.3}Ti_{1.7}Al_{0.3}(PO_4)_3$ [7],[8],[11],[39], having a similar crystallographic structure to that of rhombohedral sodium super ionic conductors (NASICON), from the sodium zirconium phosphate (NZP) structural family [11],[38]. However, the presence of the reducible ion Ti in this material, limits its electrochemical performance. Very recently, advances have been offered by the study of the material $Li_{1.2}Zr_{1.9}Ca_{0.1}(PO_4)_3$ where the zirconium based phosphate offers a much higher electrochemical stability.

The general formula of the NZP materials is given by $M_xA_2(TO_4)_3$. Positions T commonly represent phosphate groups, although a wide range of further elements have also been reported such as, arsenic, antimony, silicon, bismuth, boron, molybdenum and others [40],[41]. The essential requirement is for these elements to form tetrahedral, TO_4, groups. Atoms A occupy octahedral AO_6 arrays and are predominantly trivalent or tetravalent cations. Mixtures (III-IV) or partial substitution of these elements by di- or pentavalent cations have also been documented [40],[41]. These tetrahedral, TO_4, and octahedral AO_6 building blocks form the framework of the NZP materials, while the resultant interstitial sites are filled by M-cations. The M-cations are commonly ions of unit charge, such as alkali metal, hydrogen, ammonium groups, however, they can also be partially or fully occupied by ions of higher charges (2+ or 3+) or even absent [40],[41]. There are four such interstitial sites per formula unit, described by the crystallographic formula

$(Mi)(Mii)_3A_2(TO_4)_3$, where Mi and Mii have different crystallographic orientations, connected by narrow passageways, Figure 25 [42].

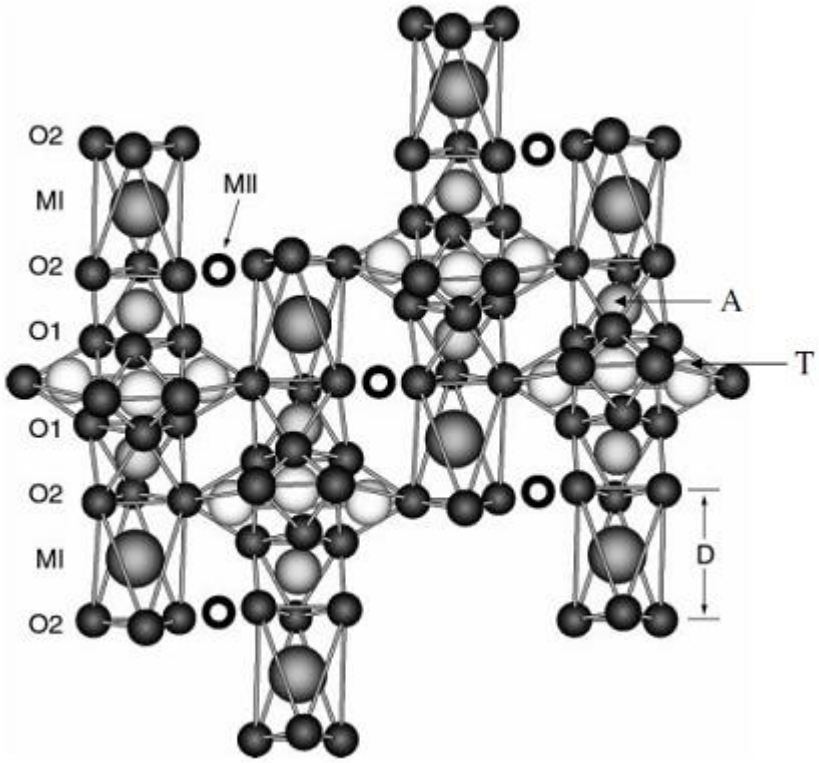

Figure 25: Portion of the ideal NZP structure, with crystallographic formula $(Mi)(Mii)_3A_2(TO_4)_3$ showing the packing of polyhedral units along the c axis. The sites available for Li-incorporation, MI and MII, are shown. The parameter D refers to the distance between adjacent O_2 planes along the c axis [42].

This highlights the vast compositional flexibility of this structural family and, hence, an almost unrivalled capacity with which to tailor properties. Indeed, fast Na-ionic conduction has been introduced into these materials by adoption of suitable substitution mechanisms, such as $Na_{1+3x}Zr_2(P_{1-x}Si_xO_4)_3$ (NASICON) where peak performance is offered in the range $1.8 < x < 2.3$ [43]. Conversely, the end members of this series $NaZr_2(PO_4)_3$ and $Na_4Zr_2(SiO_4)_3$ offer poor ionic conduction. In the former case Na is confined to the Mi sites due to the narrowness of the Mi to Mii passageways, whereas in the latter all Mii and Mii sites are fully occupied. It is only by the correct dopant strategy and removal of steric hindrances that the Mii sites can be partial filled and ion migration can occur. The lower ionic radii of Li allows it to reside in both Mi and Mii sites in the composition lithium zirconium phosphate, $LiZr_2(PO_4)_3$, leading to higher conduction than the Na analogue [44],[45],[46]. Further improvements can be made by adopting suitable solid solution mechanisms such as $Li_{3+2x}(Sc_{1-x}Mg_x)_2(PO_4)_3$, $Li_{3-2x}(Sc_{1-x}Ti_x)_2(PO_4)_3$ and $Li_{3-4x}(Sc_{1-x}Nb_x)_2(PO_3)_2$ [47]. Note similar to the Na-case, such improvements in conductivity relate to improved distribution of Li over the Mi and Mii sites and partial occupancy. It is only when these criterion are met that peak fast ion conductivity can be obtained.

In the current work, improvements will be made in the design of lithium ion conducting solid electrolytes as separators in Li-air batteries by attempting to dope with boron (B) on the T-site,

$Li_{1+6x}Zr_2(P_{1-x}B_xO_4)_3$, and A-site, $Li_{1+6x}Zr_2(P_{1-x}B_xO_4)_3$. This aims to both increase the Li-content and to distribute the Li over the two distinct interstitial crystallographic sites, as needed for fast ionic motion.

Boron (B) was reported to have been successfully doped in NZP materials both on the A-site [48] (called here Zr-site for $LiZr_2(PO_4)_3$) and the T-site [49] (called here P-site for $LiZr_2(PO_4)_3$), showing that B can potentially go on either the Zr-site or P-Site of $LiZr_2(PO_4)_3$.

$LiZr_2(PO_4)_3$ has been reported to be successfully synthesized by conventional solid state reaction [38],[50] and sol-gel methods [50],[51]. With the samples prepared by conventional solid state reaction undergoing repeated thermal treatments at 1100ºC for 16h and above 1300ºC for around 16h [50], increasing the risk of lithium volatilization. In contrast, the samples prepared by sol-gel processes undergo thermal treatments of at maximum 1200ºC for 12h [50], decreasing the risk of lithium volatilization when compared with the solid state reaction. $LiZr_2(PO_4)_3$ can either be sintered at a so called high temperature of 1200ºC, crystallizing in a triclinic form at room temperature or at a so called low temperature of 900ºC, crystallizing in a monoclinic form at room temperature. Conversely, at temperatures between 900 and 1200ºC $LiZr_2(PO_4)_3$ presents a mixture of both triclinic and monoclinic phases [44],[45]. The high temperature triclinic phase suffers a phase transition to a rhombohedral form at around 40-60ºC [44],[20]. The high temperature phase offers a sharp increase in lithium mobility leading to high ionic conductivity above the phase transition from triclinic to rhombohedral with $\sigma = 1.2x10^{-2}S.cm^{-1}$ at 300°C, while the low temperature phase has more hindered lithium motion with conductivity limited to values around, $\sigma = 5x10^{-4}S.cm^{-1}$ at 300ºC [20].

Thus, to minimize lithium losses, it was decided to synthesize $LiZr_2(PO_4)_3$ using a sol-gel method and to start by trying to dope $LiZr_2(PO_4)_3$ with boron on the P-site due to the more similar ionic radii of B^{3+} and P^{5+}, B = 0.25Å Vs P = 0.31Å [52], useful for forming the 4-coordinate tetrahedron necessary for the P-site. Secondly, attempts were made to dope $LiZr_2(PO_4)_3$ with B on the Zr-site. Here B^{3+} offers a much smaller ionic radii than Zr^{4+}, B = 0.41Å Vs Zr = 0.86Å [52], when forming the 6-coordinate octahedron as required for the Zr-site. Due to the higher ionic conduction of the high temperature phase, it was also decided to sinter the high temperature phase instead of the low temperature phase, but attempting from the beginning to avoid temperatures as high as 1200ºC.

3.2. Experimental procedure

3.2.1. Sol-gel synthesis of $Li_{1+6x}Zr_2(P_{1-x}B_xO_4)_3$ and of $Li_{1+x}Zr_{2-x}B_x(PO_4)_3$ (x = 0 to 0.25)

Lithium zirconium phosphate, $LiZr_2(PO_4)_3$, with x = 0 and 0.15, powders were synthesized based on a sol–gel method adapted from a recent work by Kim *et al* [51]. The compositions doped with boron on the P-site [$Li_{1+6x}Zr_2(P_{1-x}B_xO_4)_3$], were prepared by mixing stoichiometric amounts of the precursors orthophosphoric acid, H_3PO_4, (Carlo Erba 85% purity); zirconium(IV) acetate hydroxide, $(CH_3COO)_xZr(OH)_y$, with $x+y \cong 4$, (Sigma-Aldrich 100% purity); boric acid, H_3BO_3, (Merck 99.8% purity); lithium acetate dehydrate, $CH_3COOLi.2H_2O$, (Sigma-Aldrich 97% purity); and using citric acid (CA), $C_6H_8O_7$, (Sigma-Aldrich 99.5% purity), as the chelating agent; according to the data on

Table A 2. Lithium zirconium phosphate doped with boron on the Zr-site [$Li_{1+x}Zr_{2-x}B_x(PO_4)_3$] was prepared by mixing stoichiometric amounts of the same precursors used to prepare $Li_{1+6x}Zr_2(P_{1-x}B_xO_4)_3$, but with stoichiometries according to the data on Table A 3 instead of the data on Table A 2.

H_3PO_4, $(CH_3COO)_xZr(OH)_y$, H_3BO_3, and $CH_3COOLi.2H_2O$ were dissolved in deionised water, in that respective order. Citric acid was then added as a chelating agent, in a molar ratio CA/M: 7.5/1 (M = [Li]+[Zr]) adapted from Barre *et al* [53]. The B doping was attempted by introducing H_3BO_3 in the solution, as mentioned above. The solution was continuously stirred at 80ºC for at least 12 h. The resulting gel was fired in air at 750ºC for 5h (above the carbon self-ignition temperature [54]), with heating and cooling rates of 1ºC/min, in order to burn the organics present. The resulting powder was ground with a mortar and pestle and pressed uniaxially into pellets (8mm in diameter) for 1min at 20MPa, followed by isostatic pressing for 15min at 450MPa. The pellets were fired using sacrificial powder of the same composition, as illustrated in Figure 26 (b), following a two-step sintering cycle, illustrated in Figure 26 (a), with a peak temperature of 1000ºC for 30min and a dwell temperature of 900ºC for 10h, with heating to 1000ºC at 5ºC/min, cooling to 900ºC at 10ºC/min and cooling to 20ºC at 5ºC/min. Both the calcined and sintered powders were analyzed by X-ray diffraction (XRD) using a Rigaku Geigerflex diffractometer (Cu$K\alpha$ radiation, 10-80º 2θ, step width 0.02º, scan rate 3º/min).

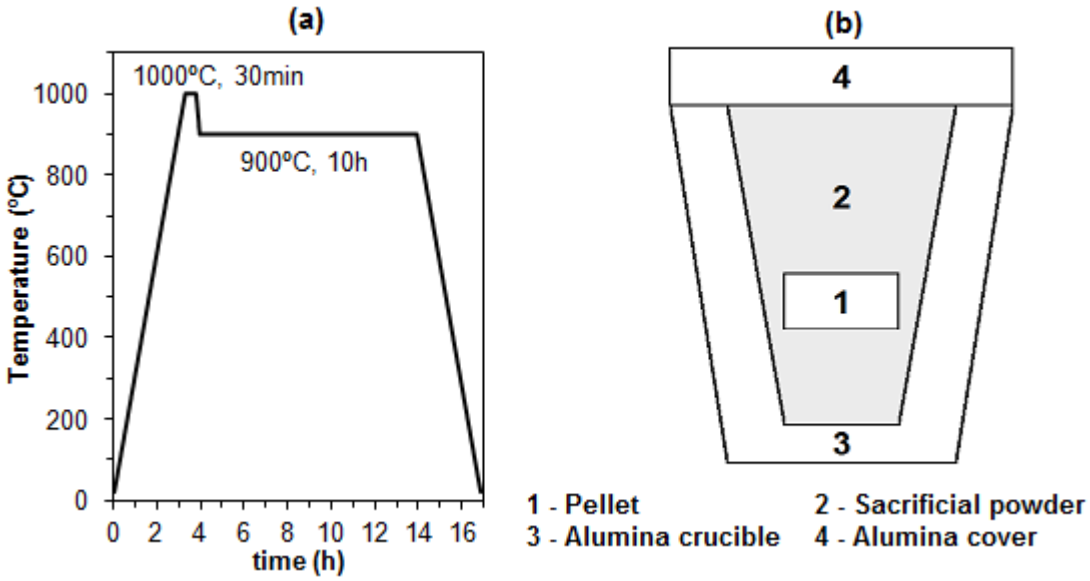

Figure 26: Two-step sintering cycle (a) and pellet sintering schematics (b).

Due to the noted low solubility of $(CH_3COO)_xZr(OH)_y$ in water, an alternative sequence for addition of the chemicals was also attempted. $(CH_3COO)_xZr(OH)_y$ was dissolved in a solution of 5mL of acetic acid, Sigma-Aldrich 99% purity, in deionised water, followed by the addition of $CH_3COOLi.2H_2O$, H_3BO_3 and citric acid, with the solution of H_3PO_4 in deionised water added after total solubilisation of the other precursors. Other than the altered addition sequence of the chemicals, the process was the same as described above, except for the calcination cycle where the resulting gel was fired in air at 600ºC for 5h, with a heating and cooling rate of 1ºC/min, in order to burn the organics present based on the thermogravimetric analysis (TGA) data recorded for the gel synthesized by this modified method.

As the method described before did not produce pure $Li_{1+6x}Zr_2(P_{1-x}B_xO_4)$ phases (see section 3.3), one tried another soft chemistry method changing the precursors. In this case, the $Li_{1+6x}Zr_2(P_{1-x}B_xO_4)_3$, with x = 0 and 0.10, powders were synthesized based on a sol–gel method adapted from Alamo *et al* [50], as illustrated in Figure 28. These compositions doped with boron on the P site, $Li_{1+6x}Zr_2(P_{1-x}B_xO_4)_3$, were prepared by mixing stoichiometric amounts of the precursors zirconium (IV) oxychloride octahydrate, $ZrOCl_2.8H_2O$, (Sigma-Aldrich ≥99.5% purity); boric acid, H_3BO_3, (Merck 99.8% purity); lithium carbonate, Li_2CO_3, (Sigma-Aldrich ≥99% purity); and ammonium dihydrogen phosphate, $NH_4H_2PO_4$, (Sigma-Aldrich 99.999% purity); according to the data on Table A 4. Lithium zirconium phosphate doped with boron on the Zr-site, $Li_{1+x}Zr_{2-x}B_x(PO_4)_3$, with x = 0, 0.025, 0.050, 0.075, 0.100, 0.150, 0.200 and 0.250, powders were prepared by mixing stoichiometric amounts of the same precursors used to prepare $Li_{1+6x}Zr_2(P_{1-x}B_xO_4)_3$, but with stoichiometries according to the data on Table A 5 instead of the data on Table A 4.

$ZrOCl_2.8H_2O$, H_3BO_3 and Li_2CO_3 were dissolved in deionised water with constant stirring, in that respective order. The pH of the solution was confirmed to be inside the range 1-3, as suggested by Alamo *et al* [50]. If the value measured was outside that interval the pH was corrected with the addition of hydrochloric acid or ammonium hydroxide. A solution containing the $NH_4H_2PO_4$, in deionised water, was added with strong stirring. The solution was continuously stirred at 60ºC for at least 12 h. The resulting gel was oven dried above 105ºC, with an intermediary step of grinding with a mortar and pestle, to ensure homogeneous drying. The resulting oven dried gel was further ground with a mortar and pestle and was pressed uniaxially into pellets (8mm in diameter) for 1min at 20MPa, followed by isostatic pressing for 15min at 450MPa. The pellets were fired using sacrificial powder of the same composition, as illustrated in Figure 26 (b), following three different sintering cycles, as illustrated in Figure 27, the first with a dwell temperature of 1000ºC for 5h (A), the second with a dwell temperature of 1200ºC for 5h (B), both with heating at 1.2ºC/min and cooling at 5ºC/min, and the third and final with a dwell temperature of 1200ºC for 12h (C), with heating and cooling at 5ºC/min. The experimental densities of the green and sintered pellets were registered from Table 5 through Table 9. The calcined and sintered powders were analyzed by XRD using a Rigaku Geigerflex diffractometer (Cu$K\alpha$ radiation, 10-80º 2θ, step width 0.02º, scan rate 3º/min).

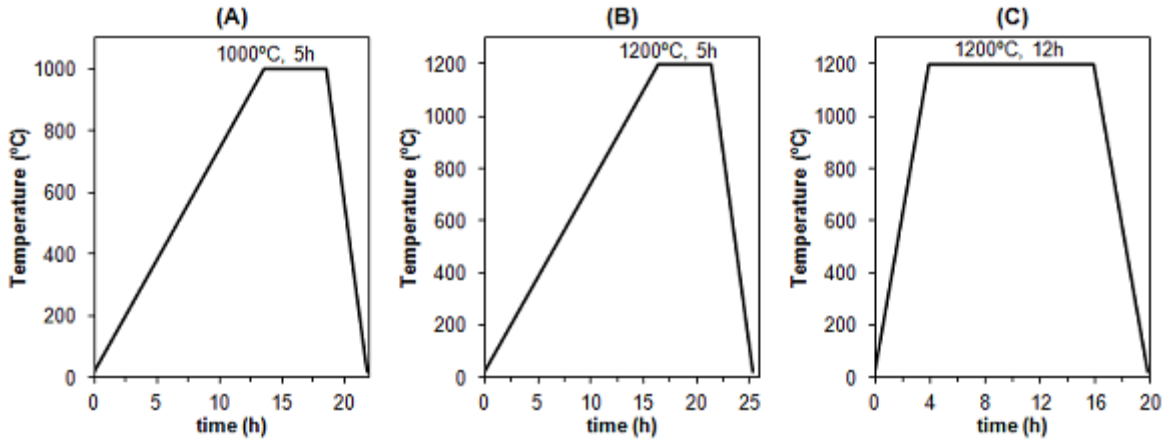

Figure 27: The three different sintering cycles tested:
(A) 1000ºC for 5h; (B) 1200ºC for 10h and (C) 1200ºC for 12h.

A pure phase of $LiZr(PO_4)_3$ materials was only obtained for B-doped compositions in Zr-site, using the preparation method illustrated on Figure 28, for the sintering cycle of 12h at 1200ºC [Figure 27 (C)]. Hence the powders with $Li_{1+x}Zr_{2-x}B_x(PO_4)_3$, with x = 0, 0.025, 0.050, 0.075, 0.100, 0.150, 0.200 and 0.250 were selected for further characterization.

The oven dried gel of $Li_{1.20}Zr_{1.80}B_{0.20}(PO_4)$ was analyzed by TGA using a Netzsch STA 449F3 TG-DTA/DSC instrument in flowing air. Thermal expansion or contraction behaviour in air was followed using a Linseis dilatometer on a green compact rectangular sample of $Li_{1.025}Zr_{1.975}B_{0.025}(PO_4)_3$. Microstructural analysis was performed in sintered samples of $LiZr_2(PO_4)_3$ and $Li_{1.05}Zr_{1.95}B_{0.05}(PO_4)$ by scanning electron microscopy (SEM) using a Hitachi S4100 equipment. Rietveld refinement of the unit cell parameters, volume V, a, b and c, was performed from the XRD data of the sintered powders of $Li_{1+x}Zr_{2-x}B_x(PO_4)_3$, with x = 0, 0.025, 0.050, 0.075 and 0.100, using the FullProf Suite Program (2.05), to find the solid solution limit of B on the Zr-site. Sintered powders of $LiZr_2(PO_4)3$, $Li_{1.05}Zr_{1.95}B_{0.05}(PO_4)_3$ and $Li_{1.10}Zr_{1.90}B_{0.10}(PO_4)_3$ were analyzed by XRD as a function of temperature, on a HTK 18N High-Temperature Chamber, using a PANalitical X'Pert Pro Diffractometer (Cu$K\alpha$ radiation, 10-80º 2θ, step width 0.02º, scan rate 100s/step), to study the evolution of the powder XRD patterns with temperature in 100ºC steps, from 25 to 800ºC.

With the aim to obtain fully densified pellets for electrochemical characterization, different densification approaches were tested: i) calcination of the gel at 400ºC before sintering, ii) milling of the gel after calcination, iii) isostatic pressing after milling and iv) two-step sintering. The density results from those attempts are listed in Table 9.

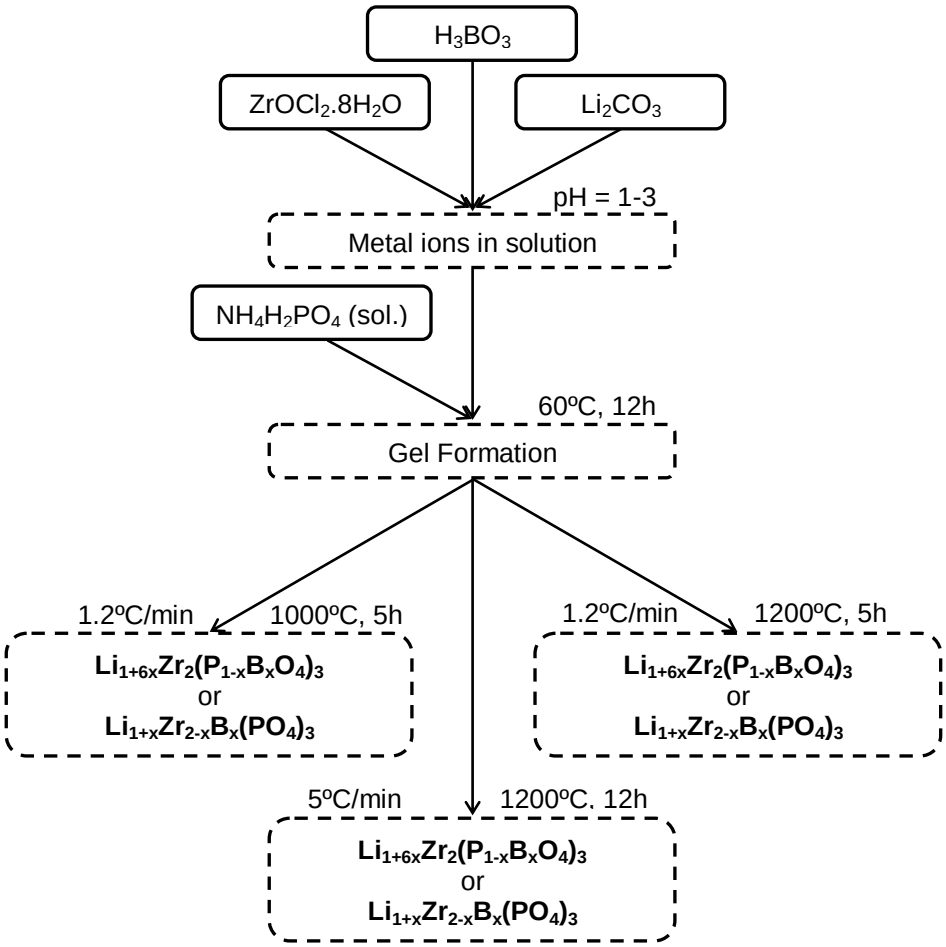

Figure 28: Experimental procedure for the preparation of $Li_{1+6x}Zr_2(P_{1-x}B_xO_4)_3$ or $Li_{1+x}Zr_{2-x}B_x(PO_4)_3$ powders.

3.3. Results and discussion

3.3.1. Sol-gel method and B doping site selection

Figure 29 to Figure 31 show the XRD results for the sintered powders of B doped $LiZr_2(PO_4)_3$ that were synthesized based on a sol–gel method adapted from the work by Kim *et al* [51]. Figure 29 and Figure 30 show the XRD results from the powders prepared with the original addition order of chemicals. One can observe from those XRD spectra that a good crystallinity was achieved after sintering. However, a pure $LiZr_2(PO_4)_3$ phase was not obtained and ZrP_2O_7 impurity peaks were always detected. The same can also be observed for the modified order with the use of acetic acid with the XRD data presented on Figure 31, with even more impurities being detected. One can also observe that for the selected sintering cycles, a mixture of both the high temperature phase (triclinic) and the low temperature phase (monoclinic) is present at room temperature in accordance with the bibliographic references [44],[45].

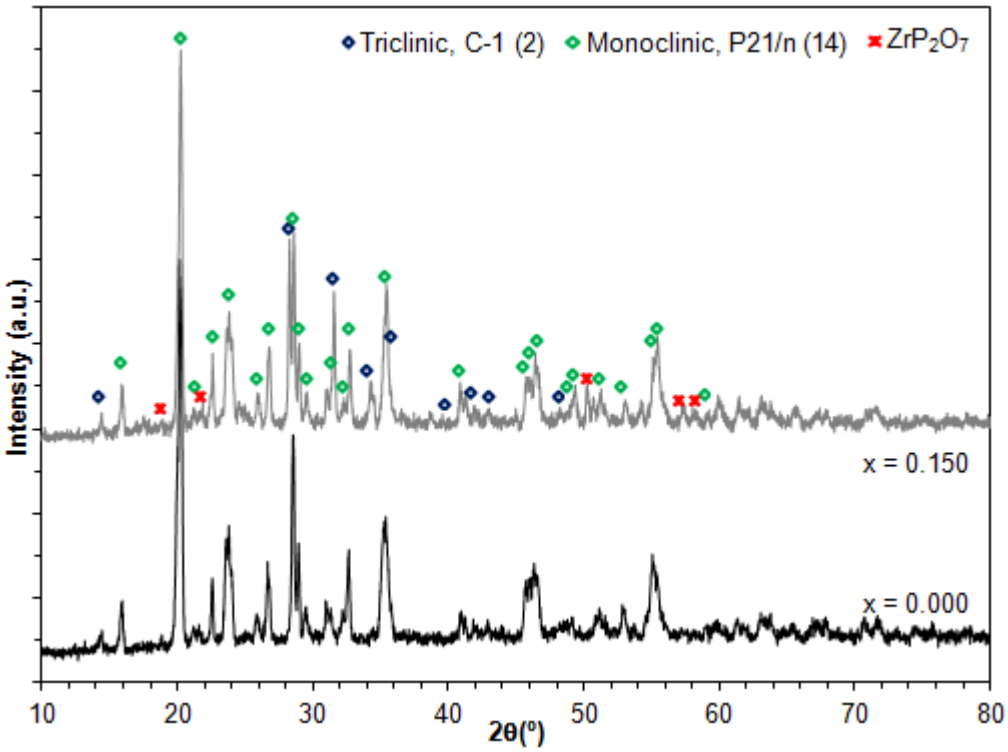

Figure 29: Powder XRD spectra of $Li_{1+6x}Zr_2(P_{1-x}B_xO_4)_3$, after a two-step sintering cycle of 1000ºC for 30min and of 900ºC for 10h, with x = 0.000 and 0.150.

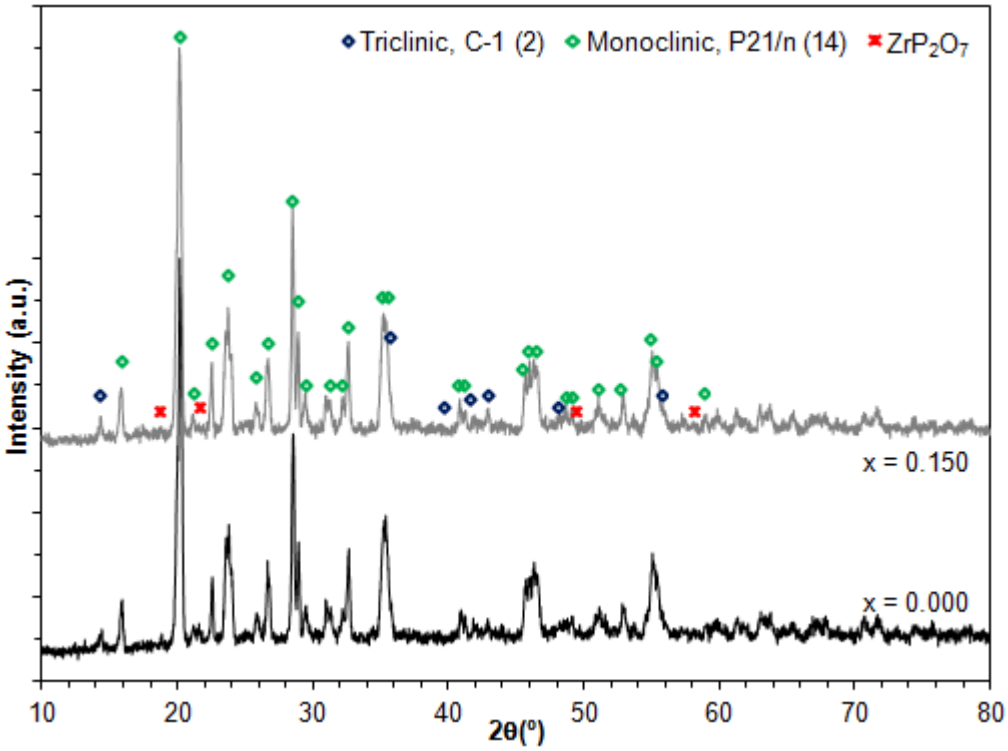

Figure 30: Powder XRD spectra of $Li_{1+x}Zr_{2-x}B_x(PO_4)_3$, after a two-step sintering cycle of 1000ºC for 30min and of 900ºC for 10h, with x = 0.000 and 0.150.

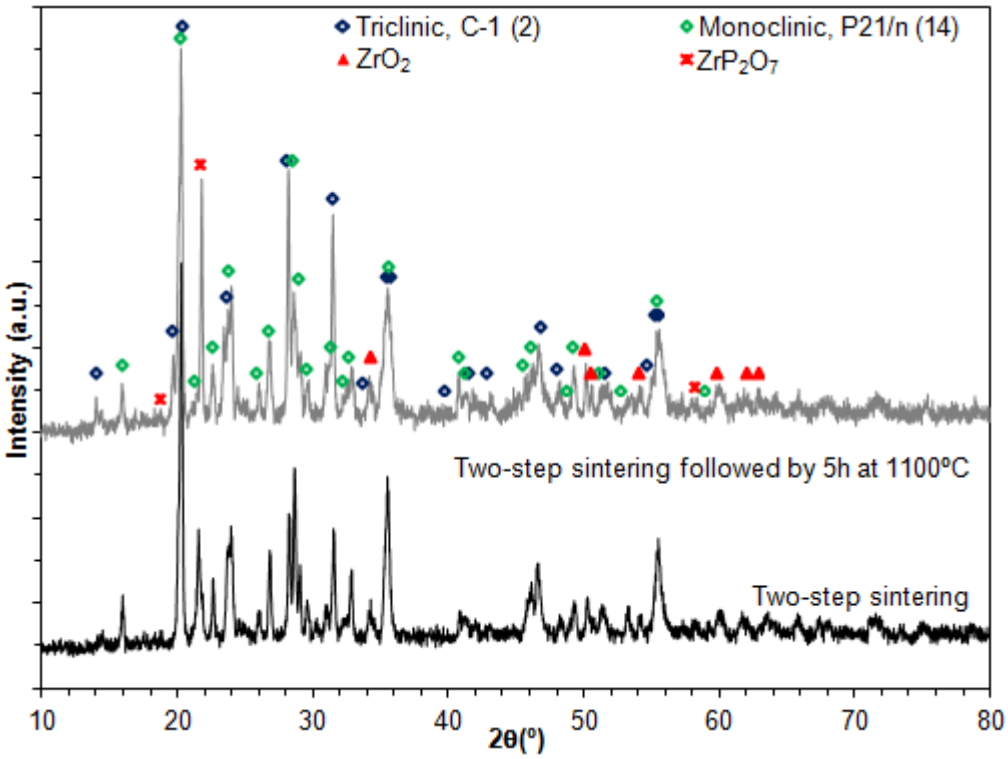

Figure 31: Powder XRD spectra of $Li_{1+x}Zr_{2-x}B_x(PO_4)_3$, x=0, prepared using the alternative sequence for addition of the chemicals with acetic acid, after calcination at 600ºC for 5h followed by a two-step sintering cycle and an extra cycle at 1100ºC for 5h.

Figure 32 and Figure 33 show the XRD results for the sintered powders of B doped $LiZr_2(PO_4)_3$ that were synthesized based on a sol–gel method adapted from Alamo *et al* [50], as illustrated on Figure 28. Figure 32 shows the XRD results from the powders sintered with the initially selected sintering cycle at 1000ºC for 5h. One can observe from the XRD spectra that a good crystallinity was achieved after sintering for both B doping in the P-site and Zr-site. However, a pure $LiZr_2(PO_4)_3$ phase was only achieved for B doping in the Zr-site and not for B doping in the P-site, as Li_3BO_3 impurity peaks were detected for $L_{1+6x}Zr_2(P_{1-x}B_xO_4)_3$ with x = 0.10. One can also observe that for the selected sintering cycle a mixture of both the high (triclinic) and the low (monoclinic) temperature phases are present at room temperature in accordance with the bibliographic references [44],[45].

Figure 33 shows the XRD results from the powders sintered with the final sintering cycle at 1200ºC for 12h. One can observe from the XRD spectra that a good crystallinity was achieved after sintering for both B doping of the P-site and Zr-site. A pure $LiZr_2(PO_4)_3$ phase was obtained for B doping in the Zr-site but not for B doping in the P-site, as Li_3BO_3 impurity peaks were detected for $L_{1+6x}Zr_2(P_{1-x}B_xO_4)_3$ with x = 0.10, as before. One can also observe that for the selected sintering cycle and for $Li_{1+x}Zr_{2-x}B_x(PO_4)_3$ only the high temperature phase (triclinic) is present at room temperature in accordance with the bibliographic references [44],[45]. However for $Li_{1+6x}Zr_2(P_{1-x}B_xO_4)_3$ both high (triclinic) and low (monoclinic) temperature phases still coexist, in addition to the Li_2BO_3 impurity phase.

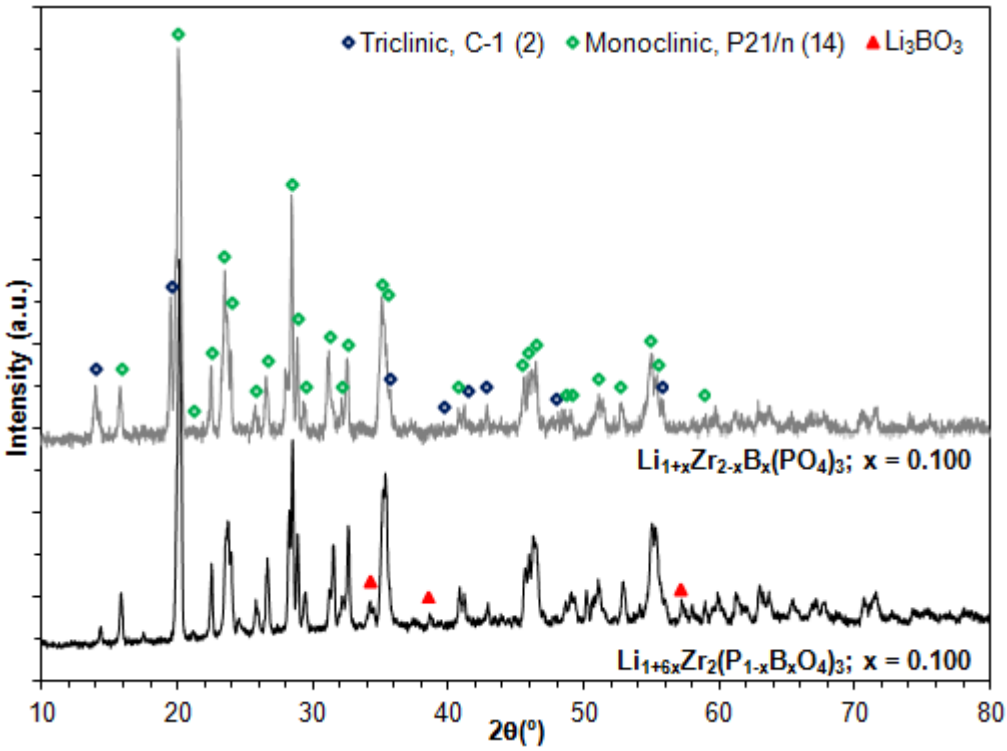

Figure 32: XRD spectra of $Li_{1+x}Zr_{2-x}B_x(PO_4)_3$ and $Li_{1+6x}Zr_2(P_{1-x}B_xO_4)_3$, after sintering at 1000ºC for 5h, with x = 0.100.

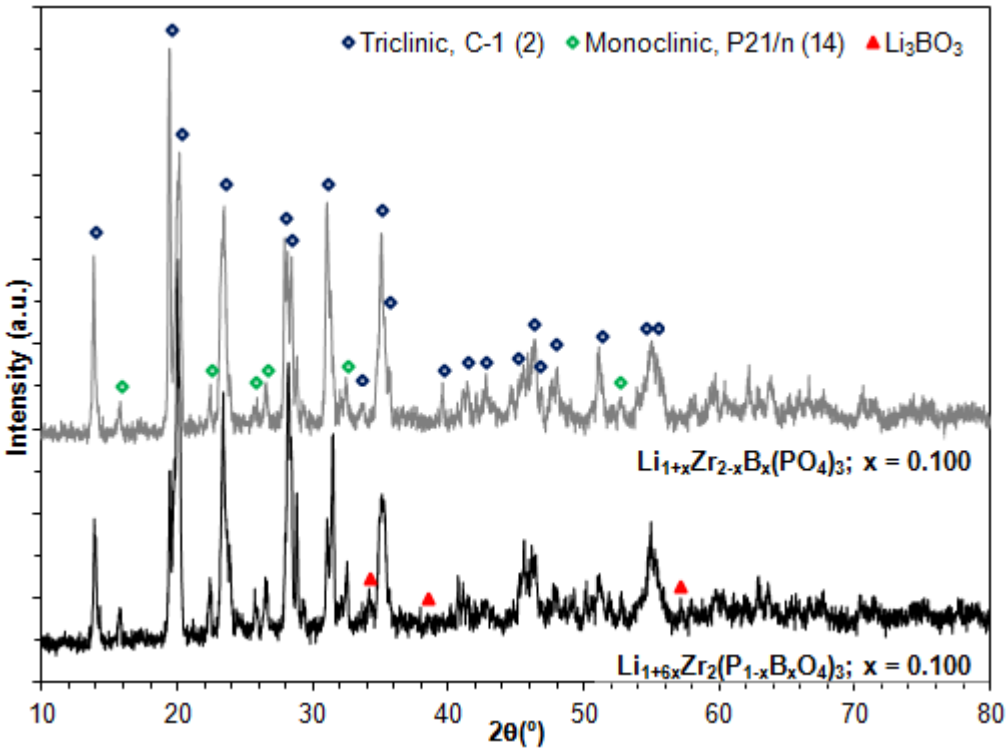

Figure 33: XRD spectra of $Li_{1+x}Zr_{2-x}B_x(PO_4)_3$ and $Li_{1+6x}Zr_2(P_{1-x}B_xO_4)_3$, after sintering at 1200ºC for 12h, with x = 0.100.

3.3.2. Sintering method selection

After facing several issues with the initial sol-gel method employed to synthesize $LiZr_2(PO_4)_3$, it was decided to perform a TGA of the gel before and after a calcination step at 350ºC, graphically represented on Figure 34. Looking at Figure 34 one can observe that it is possible to calcine the gel directly at temperatures above 500ºC, but based on the previous work it was decided to calcine the gel at 600ºC.

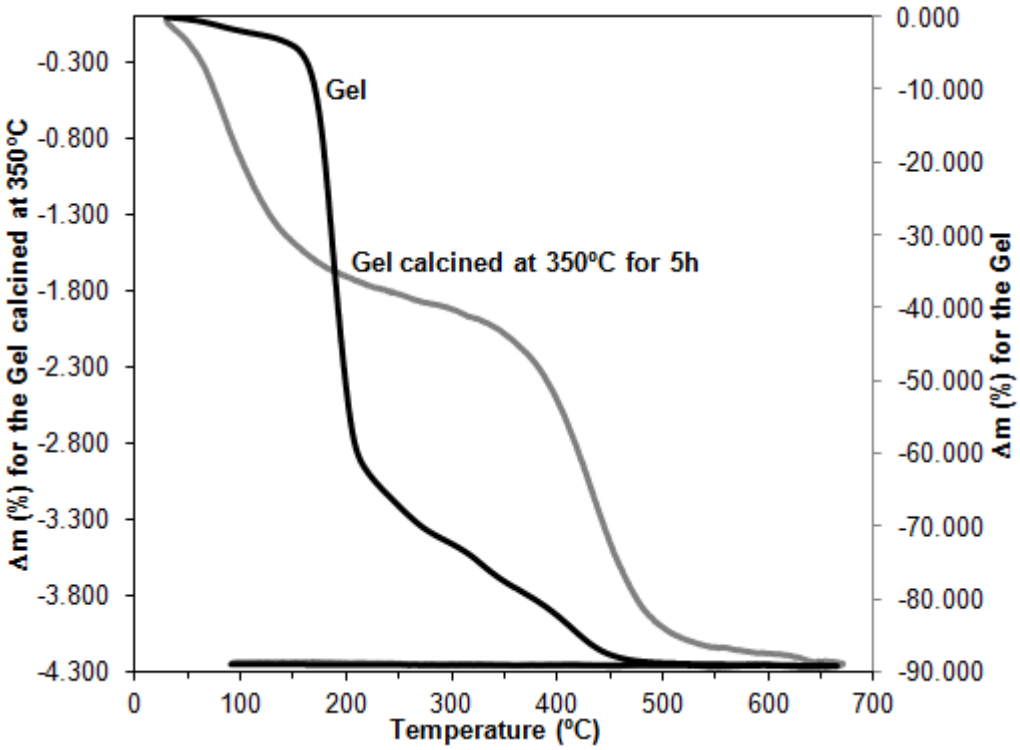

Figure 34: TGA of the gel and the gel calcined at 350ºC for 5h, for $LiZr_2(PO_4)_3$, for the modified method with acetic acid.

Figure 35 confirms that for temperatures around 800ºC crystallization of the low temperature phase (monoclinic) already occurs with some residual high temperature phase also present. From Figure 36 one can observe that it is preferable to do a single calcination step at 600ºC, than two steps at 350ºC followed by 600ºC, because in this way the starting powder does not present traces of a final reaction product and, thus, would be more active and homogenous, which are desirable properties for the reaction powder before pressing the pellets and for further densification and sintering.

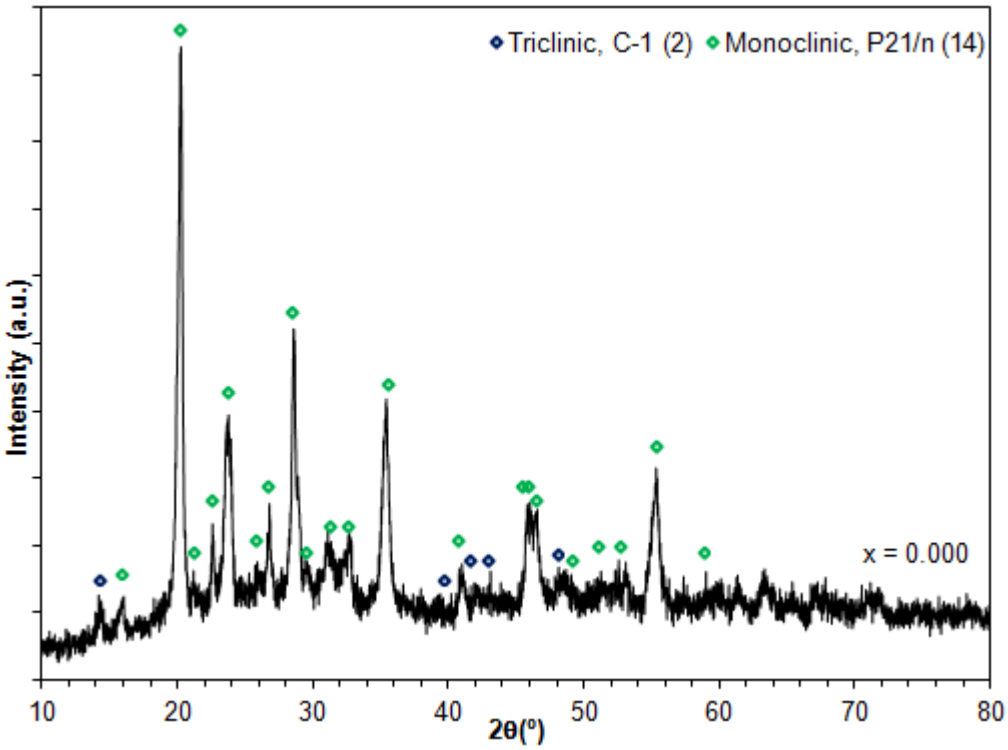

Figure 35: Powder XRD spectra of $LiZr_2(PO_4)_3$, after calcination at 800ºC for 5h (heating and cooling at 1ºC/min).

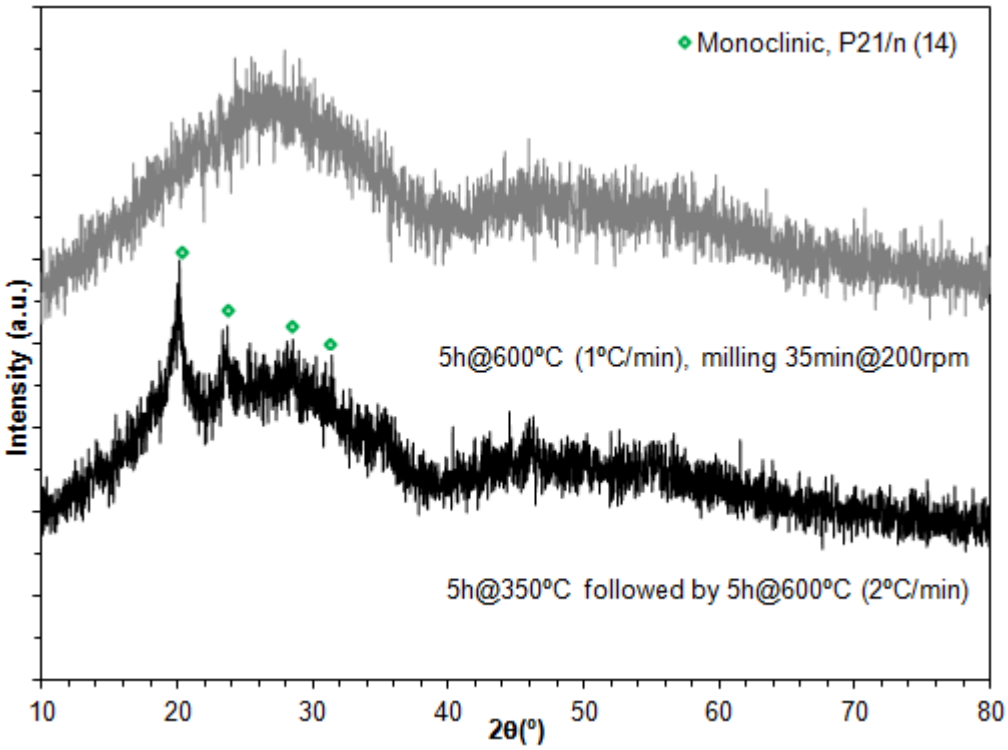

Figure 36: Powder XRD spectra of $LiZr_2(PO_4)_3$, prepared using the alternative sequence for addition of the chemicals with acetic acid, after calcination at 600ºC for 5h.

In an attempt to minimize the lithium losses during the heat treatments several sintering cycles were tested, starting from sintering at 1000ºC for 5h, with on extra cycle at 1200ºC for 12h for x = 0, that resulted on the data summarized in both Table 5 and Table 6 and the XRD spectra of Figure 32. A sintering cycle at 1200ºC for 5h was also tested, with an extra cycle at 1200ºC for 12h for x = 0.25, resulting in the data presented in Table 7. From this data it was decided to sinter the pellets using the sintering cycle with a dwell at 1200ºC for 12h, as illustrated by Figure 27 (C), that produced sintered powders of $Li_{1+x}Zr_{2-x}B_x(PO_4)_3$, with $x \leq 0.075$, with the pure high temperature phase (triclinic) phase, as shown by the results from section 3.3.3 (Figure 37).

Table 5: Sintering attempt at 1000ºC for 5h, heating at 1.2ºC/min and cooling at 5ºC/min, for $Li_{1+6x}Zr_2(P_{1-x}B_xO_4)_3$.

	Green					Sintered				
x	**mass (g)**	**d (mm)**	**th (mm)**	**ρ (kg/dm³)**	**% ρ**	**mass (g)**	**d (mm)**	**th (mm)**	**ρ (kg.dm³)**	**% ρ**
0.00	0.3263	8.035	3.270	1.968	60.93%	0.1919	7.025	2.890	1.713	53.04%
0.10	0.2978	8.055	3.440	1.699	52.59%	0.2012	5.840	2.565	2.928	90.66%

Table 6: Sintering attempt at 1000ºC for 5h, heating at 1.2ºC/min and cooling at 5ºC/min, for $Li_{1+x}Zr_{2-x}B_x(PO_4)_3$, with x = 0, 0.10 and 0.25. With an extra cycle at 1200ºC for 12h, heating and cooling at 5ºC/min, for x = 0.

	Green					Sintered				
x	**mass (g)**	**d (mm)**	**th (mm)**	**ρ (kg/dm³)**	**% ρ**	**mass (g)**	**d (mm)**	**th (mm)**	**ρ (kg.dm³)**	**% ρ**
0.00	0.3192	8.020	3.080	2.052	63.51%	0.1905	7.100	2.760	1.743	53.97%
0.10	0.3409	8.030	3.630	1.854	57.41%	0.2252	6.450	2.980	2.313	71.60%
0.25	0.3364	8.065	3.460	1.903	58.92%	0.1898	5.815	2.580	2.770	85.76%
0.00	0.3192	8.020	3.080	2.052	63.51%	0.1775	8.080	1.940	1.784	57.25%

Table 7: Sintering at 1200ºC for 5h, heating and cooling at 5ºC/min, for $Li_{1+x}Zr_{2-x}B_x(PO_4)_3$, with x = 0.10. With an extra cycle at 1200ºC for 12h, heating and cooling at 5ºC/min, for x = 0.25.

	Green					Sintered				
x	**mass (g)**	**d (mm)**	**th (mm)**	**ρ (kg/dm³)**	**% ρ**	**mass (g)**	**d (mm)**	**th (mm)**	**ρ (kg.dm³)**	**% ρ**
0.10	0.3201	8.090	3.190	1.952	62.63%	broken	n.a.	n.a.	n.a.	n.a.
0.25	0.3125	8.035	3.250	1.896	60.84%	0.1707	5.370	2.480	3.039	97.50%
0.25	0.3192	8.020	3.080	2.052	63.51%	0.1816	7.890	1.380	2.691	86.35%

3.3.3. Phase characterization

By looking at Figure 37 one can easily observe that for x ≥ 0.10 there is a mixture of both the high (triclinic) and the low (monoclinic) temperature phases, with impurity peaks of ZrP_2O_7 appearing for x = 0.25. This data suggest that the $Li_{1+x}Zr_{2-x}B_x(PO_4)_3$ system has reached the solid solution limit at x = 0.075, where neither impurity phases or low temperature phase (monoclinic) peaks are observed. Further XRD data treatment by Rietveld refinement, graphically represented in Figure 38, suggests, by assessment of Vegard's behaviour, that the solid solution limit of B in Zr site in $Li_{1+x}Zr_{2-x}B_x(PO_4)_3$ compositions lies closer to x = 0.050, after which there is a change in the linear dependence of the cell parameters values with B content.

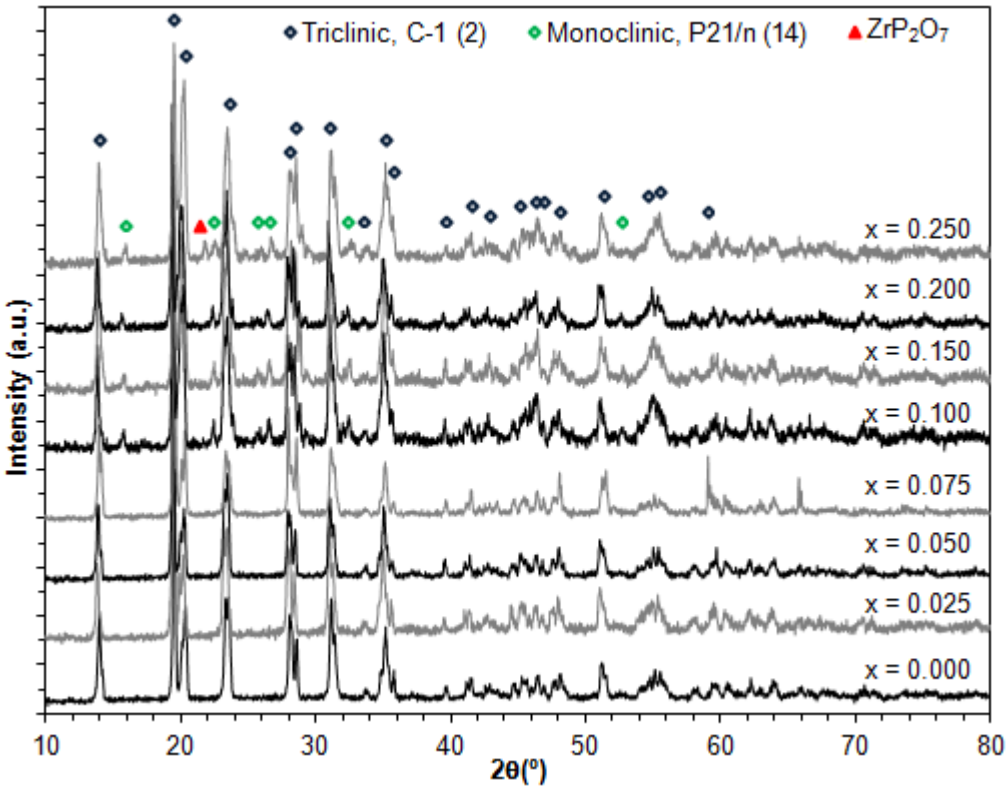

Figure 37: XRD spectra of $Li_{1+x}Zr_{2-x}B_x(PO_4)_3$, after sintering at 1200ºC for 12h, with x = 0; 0.025; 0.050; 0.075; 0.100; 0.150; 0.200 and 0.250 from the bottom to the top.

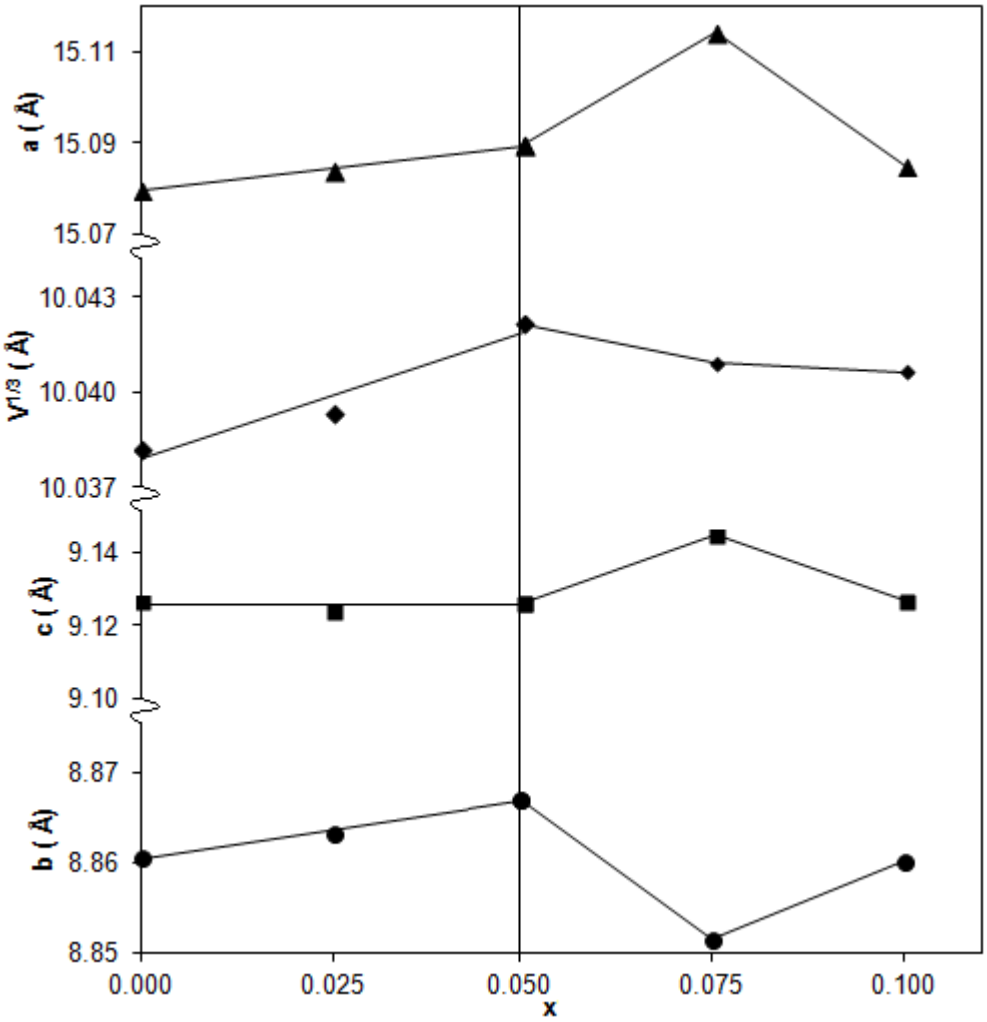

Figure 38: Graphic representation of the cubic root of the volume ($V^{1/3}$), with a, c and b parameters of the unit-cell (the order from the top to the bottom is: $V^{1/3}$, a, c and b).

To better understand this data and the structural phenomena happening with temperature, new XRD spectra were acquired at different temperatures. It is explained in the literature that both the high (triclinic) and low (monoclinic) temperature phases undergo phase transitions at two different temperatures above room temperature, at around 40-60ºC for the high temperature phase and at around 300ºC for the low temperature phase [44],[20].

The XRD spectra presented from Figure 39 to Figure 44 show the temperature induced behaviour of $LiZr_2(PO_4)_3$, and $Li_{1.05}Zr_{1.95}B_{0.05}(PO_4)_3$ (x = 0.05) that are inside the limits of solid solution and finally $Li_{1.10}Zr_{1.90}B_{0.10}(PO_4)_3$ (x = 0.10) that is outside the solid solution limit. The observed behaviour is as expected based on the data from the literature [44],[20]. One can observe the phase transition from triclinic (PDF#01-074-2562) to rhombohedral (PDF#01-070-6734) for the high temperature phase when heating from 25ºC to 100ºC (Figure 39 to Figure 42) and apparently no phase transition from monoclinic (PDF#01-070-5819) for the low temperature phase when heating to 300ºC and above (Figure 43 and Figure 44), most likely due to the low content of this low temperature phase.

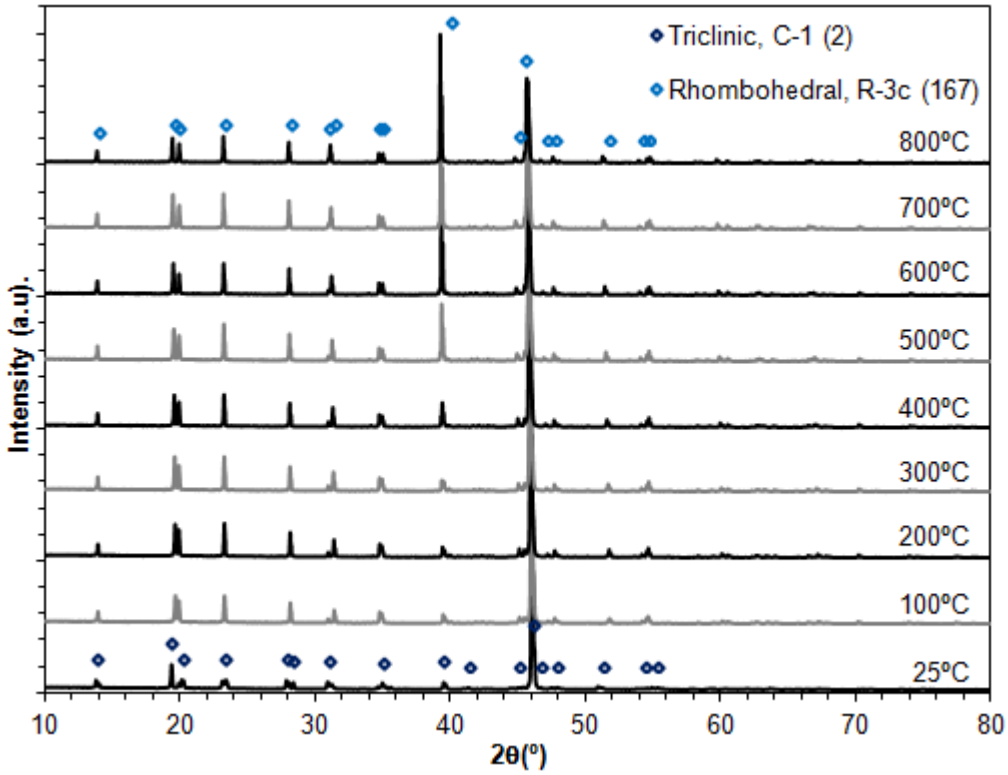

Figure 39: Evolution of powder XRD patterns with temperature for $LiZr_2(PO_4)_3$, after sintering at 1200ºC for 12h, from 25 to 800ºC from the bottom to the top.

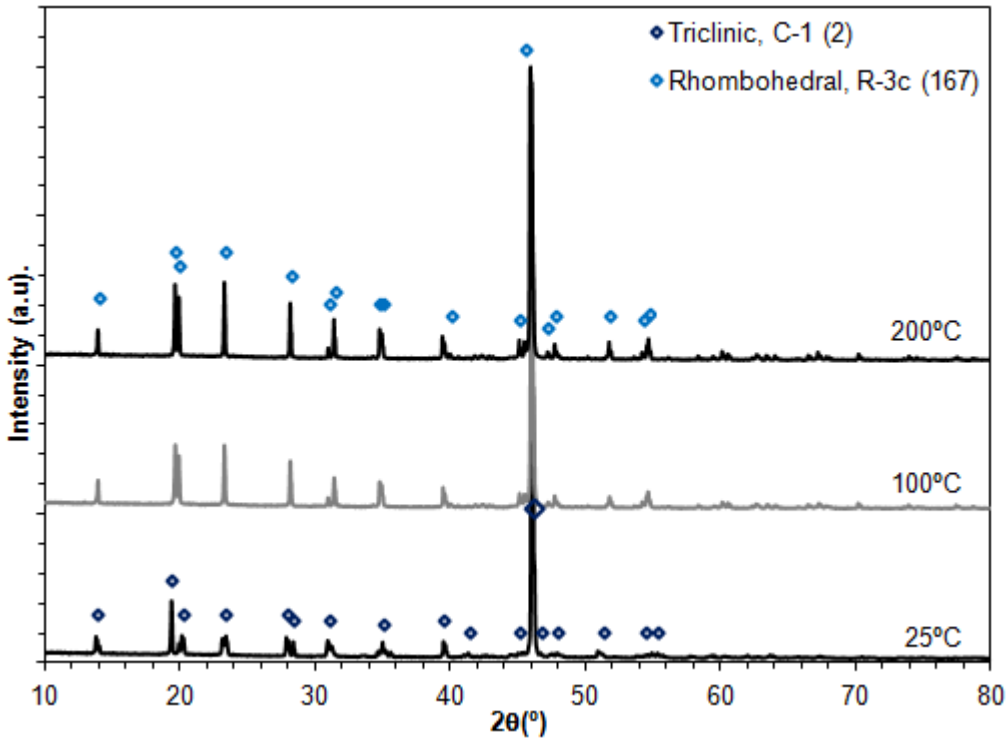

Figure 40: Evolution of powder XRD patterns with temperature for $LiZr_2(PO_4)_3$, after sintering at 1200ºC for 12h, for 25, 100 and 200ºC from the bottom to the top.

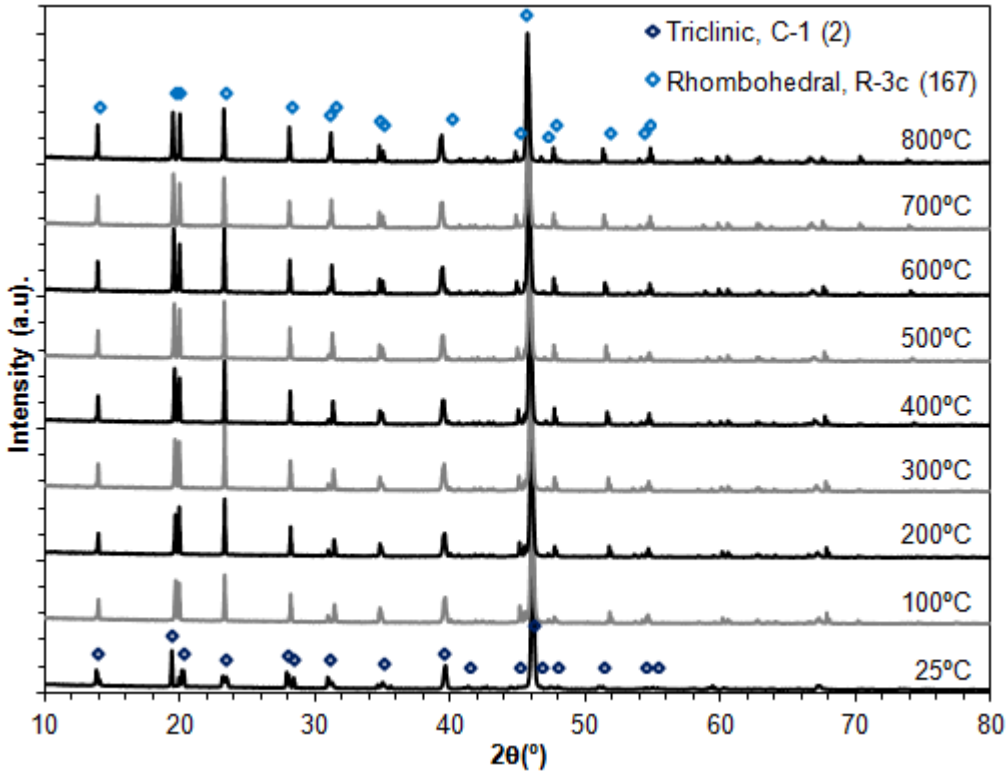

Figure 41: Evolution of powder XRD patterns with temperature for $Li_{1.05}Zr_{1.95}B_{0.05}(PO_4)_3$, after sintering at 1200ºC for 12h, from 25 to 800ºC from the bottom to the top.

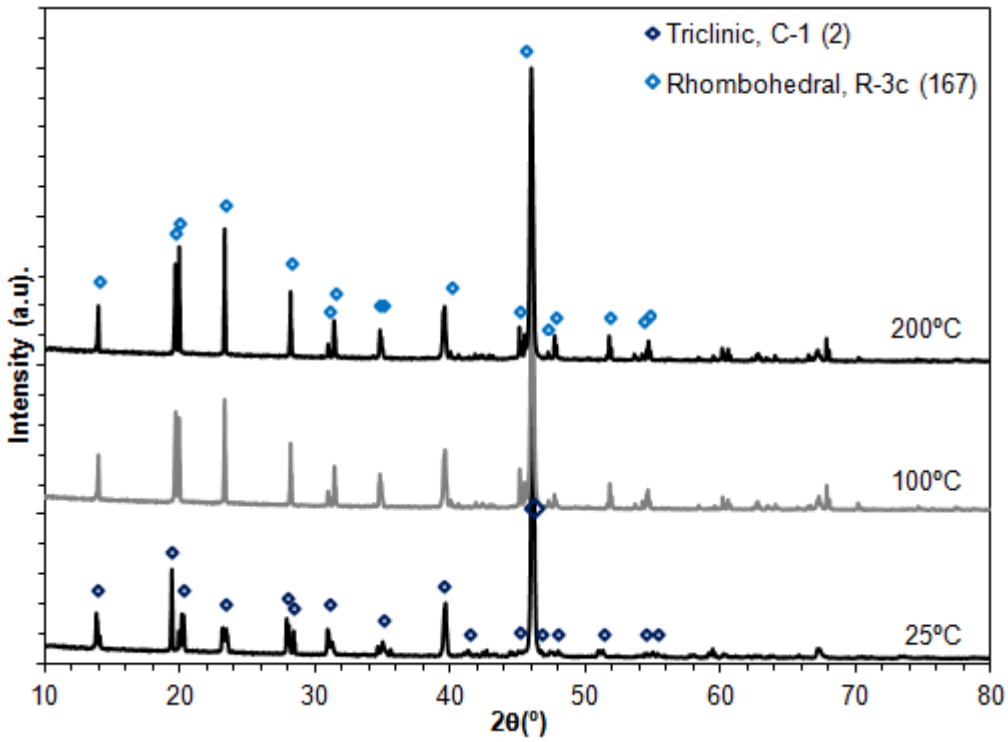

Figure 42: Evolution of powder XRD patterns with temperature for $Li_{1.05}Zr_{1.95}B_{0.05}(PO_4)_3$, after sintering at 1200ºC for 12h, 25, 100 and 200ºC from the bottom to the top.

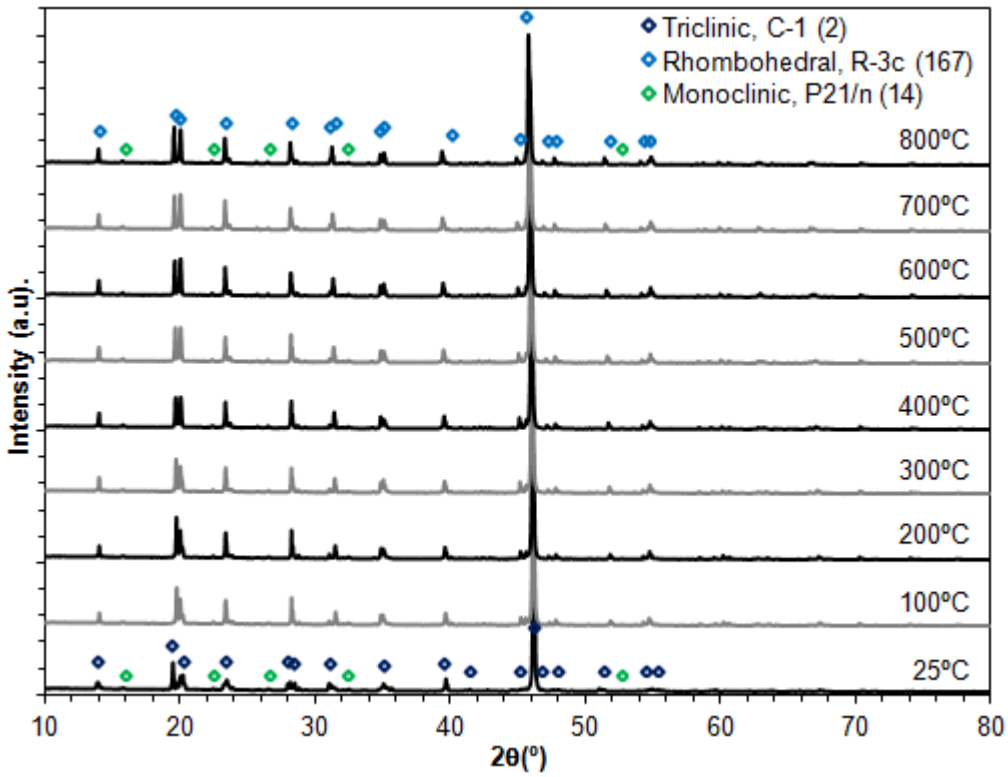

Figure 43: Evolution of powder XRD patterns with temperature for $Li_{1.10}Zr_{1.90}B_{0.10}(PO_4)_3$, after sintering at 1200ºC for 12h, 25 to 800ºC from the bottom to the top.

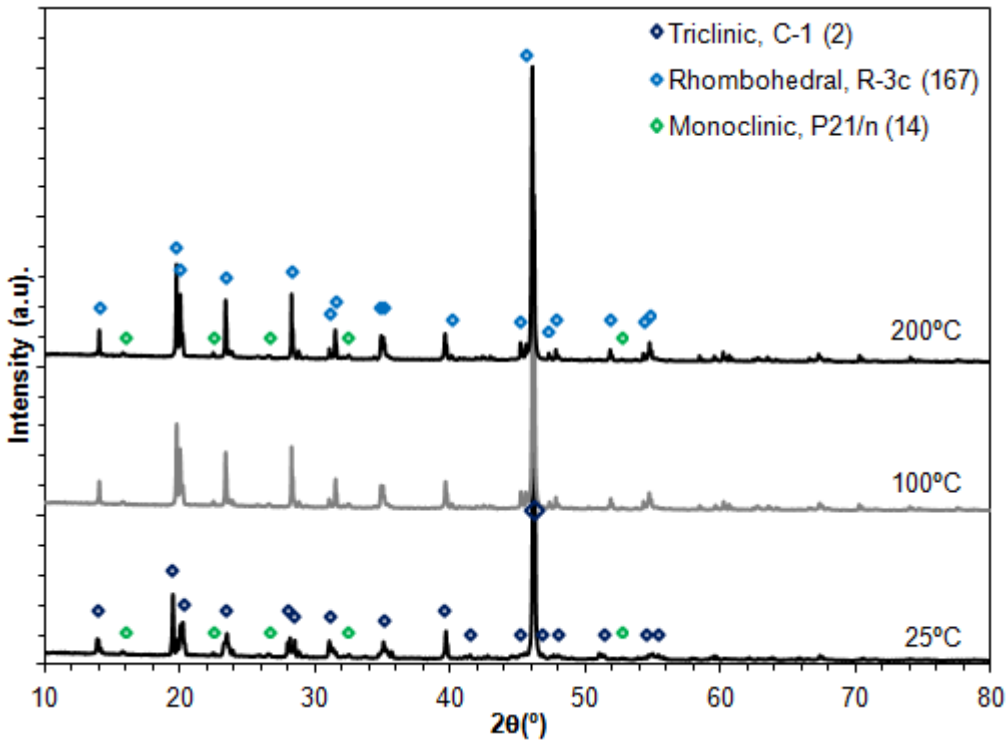

Figure 44: Evolution of powder XRD patterns with temperature for $Li_{1.10}Zr_{1.90}B_{0.10}(PO_4)_3$, after sintering at 1200ºC for 12h, 25, 100 and 200ºC from the bottom to the top.

3.3.4. Densification study

The sintering results for the sintering cycle selected above, that of a dwell at 1200ºC for 12h, originated the data listed on Table 8 and the XRD data already presented and discussed. From that data it is possible to observe that only for the compositions outside of the solid solution was possible to achieve densities close to the reported density for the triclinic phase of 3.117kg.dm^{-3} [45], with densifications between 78.51 and 88.32% of the theoretical density, for x ≥ 0.10. In this respect an excess of B_2O_3 has already been noted to be an effective sintering additive for NZP materials [55]. For the compositions inside the solid solution, the pellets either had low densification 57.77% for $LiZr_2(PO_4)_3$, or the pellets would be cracked beyond the possibility of measuring their dimensions. Still, the resulting pellets were in good enough conditions to be ground into powder to analyze by powder XRD.

Table 8: Sintering attempt at 1200ºC for 12h, heating and cooling at 5ºC/min, for $Li_{1+x}Zr_{2-x}B_x(PO_4)_3$.

	Green					Sintered				
x	**mass (g)**	**d (mm)**	**th (mm)**	**ρ (kg.dm^3)**	**% ρ**	**mass (g)**	**d (mm)**	**th (mm)**	**ρ (kg.dm^3)**	**% ρ**
0.000	0.3229	8.010	3.230	1.984	63.65%	0.1812	7.020	2.600	1.801	57.77%
0.025	0.3335	7.990	3.380	1.968	63.13%	cracked	n.a.	n.a.	n.a.	n.a.
0.050	0.2523	7.140	2.980	2.115	67.84%	cracked	n.a.	n.a.	n.a.	n.a.
0.075	n.a.	n.a.	n.a.	n.a.	n.a.	cracked	n.a.	n.a.	n.a.	n.a.
0.100	0.3741	8.020	3.880	1.908	61.23%	0.2099	6.280	2.730	2.482	79.63%
0.150	0.3343	8.015	3.480	1.904	61.09%	0.1876	6.070	2.355	2.753	88.32%
0.200	0.3290	8.020	3.400	1.915	61.45%	0.1846	5.785	2.870	2.447	78.51%

After gathering all the data present on Table 8 several efforts were performed in order to obtain dense pellets with suitable integrity, but all failed for the synthesized compositions after achieving phase purity, with the pellets either cracking or breaking after sintering as can be seen from the data listed on Table 9. Different approaches were tried, by changing the sintering temperature profile, by pressing isostatically, by calcining the resulting gel and by milling the calcined powder. However, none of these approaches worked without issues, either breaking, cracking or resulting in bi-phasic mixtures of the high (triclinic) and low (monoclinic) temperature phases after sintering.

TGA and dilatometry were performed on two different oven dried gel samples, to better help determine what steps could be done to overcome the densification issues. This was performed as a potential limit of densification could most likely be derived from decomposition of the by-product salt NH_4Cl of the sol-gel synthesis, that has a melting point of 338ºC and a boiling point of 520ºC, with sublimation occurring at 337.6ºC. It was decided from the TGA data represented graphically in Figure 45 and the dilatometry represented graphically in Figure 46 to perform two different calcinations at 400ºC and 700ºC, with an extra milling step to help achieve better densification. With that information and the powder XRD spectra of Figure 47 it was suggested that a temperature between 400 and 700ºC could possibly be the solution to remove NH_4Cl while maintaining the calcined powder amorphous enough to ensure phase homogeneity in the sintering step, as at 700ºC the powder was shown to already have crystallized, Figure 47. Another interesting feature of the dilatometry curve in Figure 46, is that the densification process is shown to be heavily dependent on time at the maximum temperature, suggesting that longer dwell times may be useful. Unfortunately there was no more time to test other temperatures and conditions.

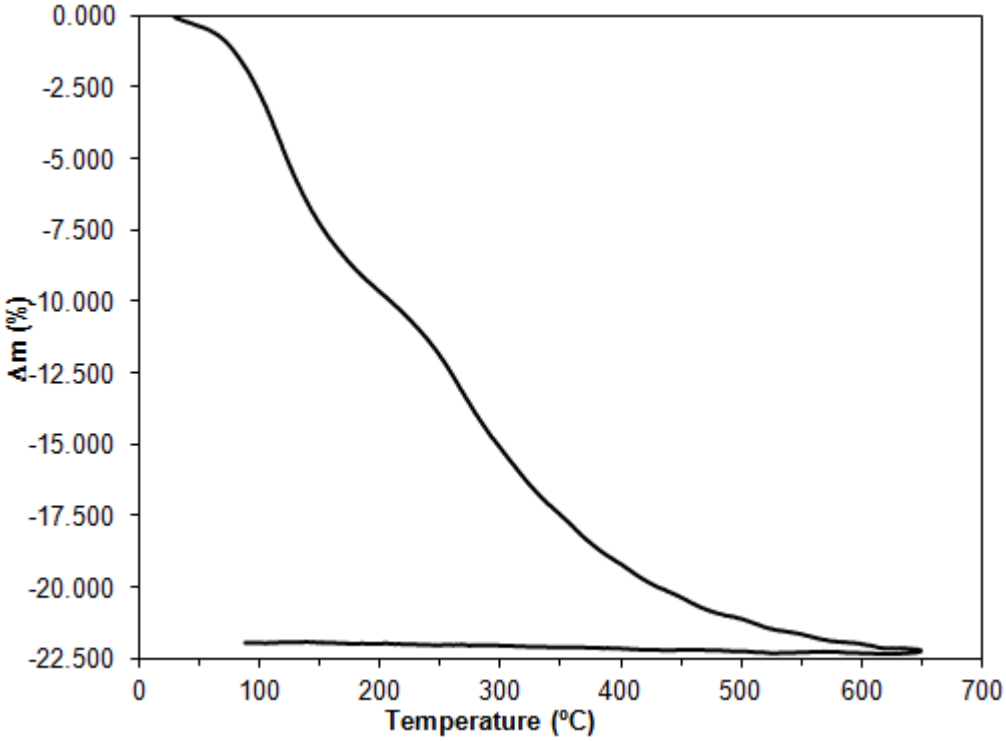

Figure 45: TGA of the oven dried gel for $Li_{1.20}Zr_{1.80}B_{0.20}(PO_4)$.

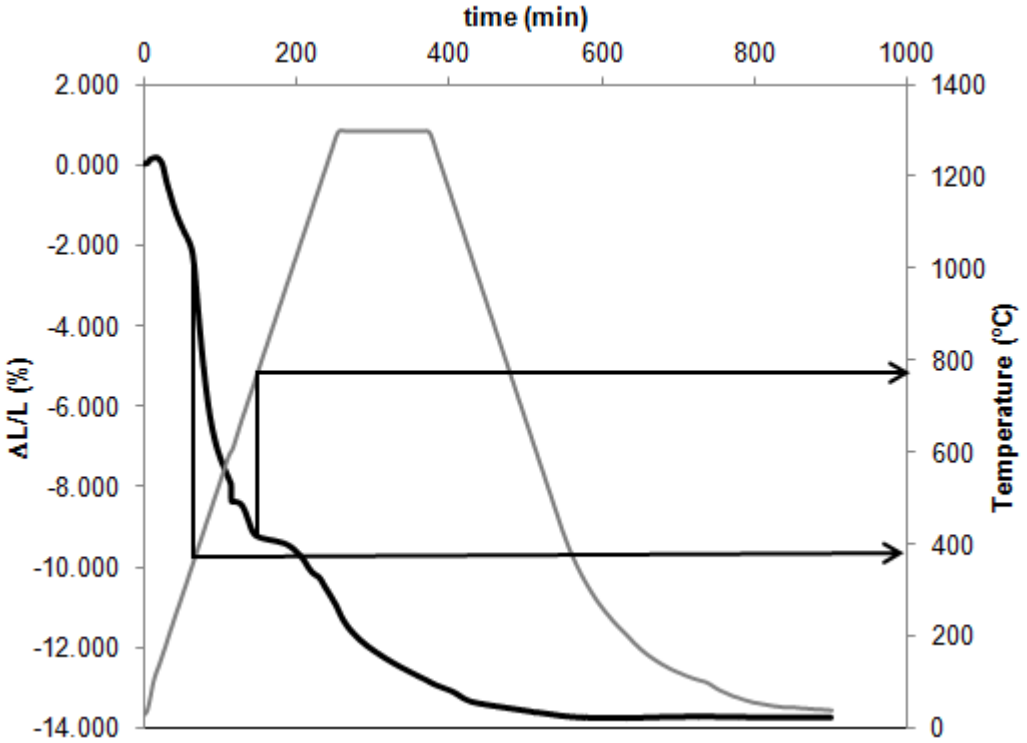

Figure 46: Dilatometry of a green compact rectangular sample of $Li_{1.025}Zr_{1.975}B_{0.025}(PO_4)_3$.

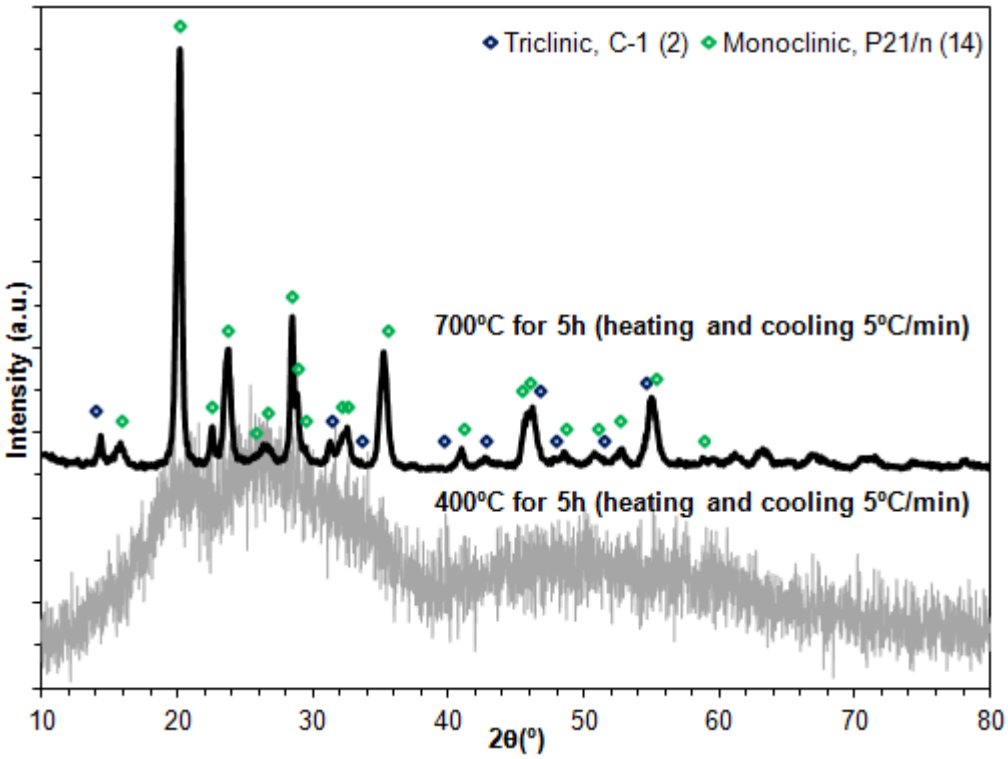

Figure 47: Powder XRD spectra of $Li_{1+x}Zr_{2-x}B_x(PO_4)_3$, x = 0.05, comparing the powder after calcination at 400ºC for 5h and 700ºC for 5h.

The different approaches that correspond to the data in Table 9, were from top to bottom: sintering at 1200ºC for 12h, heating and cooling at 5ºC/min, for $Li_{1+x}Zr_{2-x}B_x(PO_4)_3$ with x = 0.05, preceded by calcination at 400ºC for 5h, that originated a powder XRD spectrum with low temperature phase peaks (middle spectrum of Figure 48). Sintering at 1200ºC for 12h, heating and cooling at 5ºC/min, for $Li_{1+x}Zr_{2-x}B_x(PO_4)_3$ with x = 0 and 0.05, preceded by a calcination at 400ºC for 5h, milling at 300rpm for 30min and isostatic pressing for 15min at 450MPa, that always resulted in broken pellets of only the triclinic phase (bottom spectrum of Figure 48). Sintering at 1200ºC for 12h, heating and cooling at 5ºC/min, for $Li_{1+x}Zr_{2-x}B_x(PO_4)_3$ with x = 0.05, preceded by a calcination at 700ºC for 5h, milling at 300rpm for 30min and isostatic pressing for 15min at 450MPa, that always resulted in broken pellets with little low temperature phase peaks (top spectrum of Figure 48). Sintering at 1200ºC for 12h, heating and cooling at 5ºC/min, for $Li_{1+x}Zr_{2-x}B_x(PO_4)_3$ with x = 0.075, preceded by isostatic pressing for 15min at 450MPa, that always resulted in broken pellets. And a two-step sintering at 1300ºC for 1h with cooling at 10ºC/min followed by a dwell at 1200ºC for 12h (heating and cooling at 5ºC/min), preceded by a calcination at 550ºC for 5h, grinding with a mortar and pestle, for x = 0.20, that always resulted in broken pellets.

Table 9: List of results for the several densification attempts tested.

	Green					Sintered				
x	mass (g)	d (mm)	th (mm)	ρ (kg.dm^3)	% ρ	mass (g)	d (mm)	th (mm)	ρ (kg.dm^3)	% ρ
0.050	0.3828	8.005	3.910	1.945	62.41%	0.2148	6.505	2.550	2.535	81.32%
0.000	0.3315	7.210	3.880	2.093	67.14%	broken	n.a.	n.a.	n.a.	n.a.
0.050	0.1329	7.175	1.530	2.148	68.92%	broken	n.a.	n.a.	n.a.	n.a.
0.050	0.1643	7.600	1.980	1.829	58.68%	broken	n.a.	n.a.	n.a.	n.a.
0.050	0.2014	7.670	2.320	1.879	60.28%	cracked	n.a.	n.a.	n.a.	n.a.
0.075	n.a.	n.a.	n.a.	n.a.	n.a.	broken	n.a.	n.a.	n.a.	n.a.
0.200	n.a.	n.a.	n.a.	n.a.	n.a.	broken	n.a.	n.a.	n.a.	n.a.

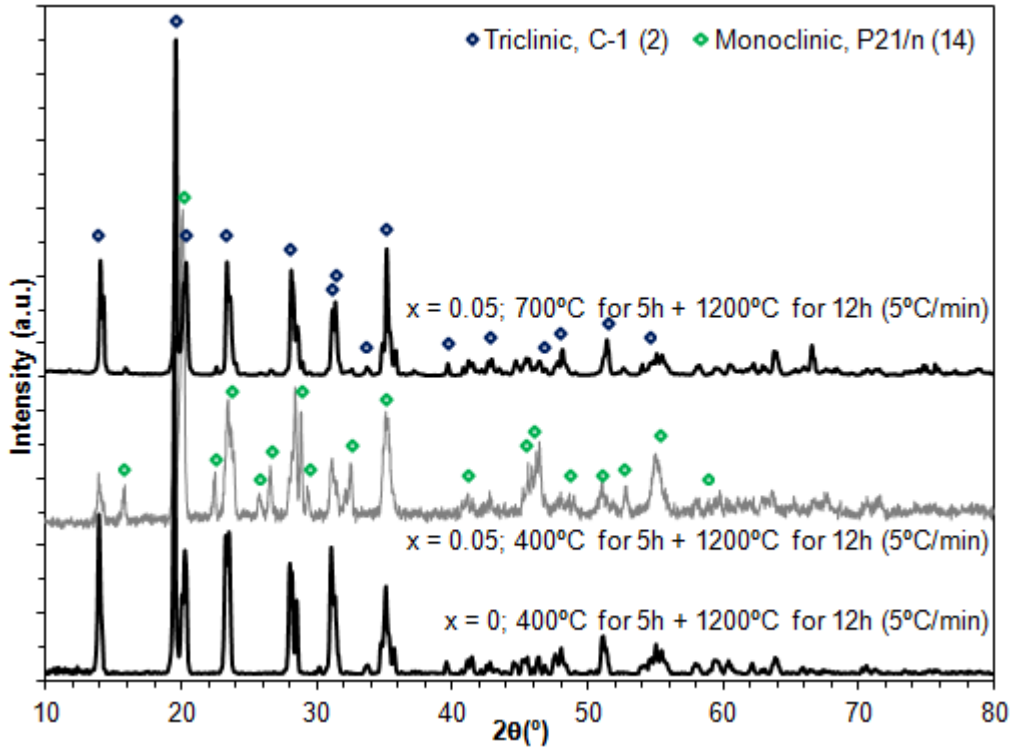

Figure 48: Powder XRD spectra of $Li_{1+x}Zr_{2-x}B_x(PO_4)_3$, x = 0, 0.050, comparing the powder sintered at 1200ºC for 12h after calcination at 400ºC for 5h and 700ºC for 5h.

Figure 49 shows the pictures of the SEM preformed in fractures of samples of $LiZr_2(PO_4)_3$ (A) and $Li_{1.05}Zr_{1.95}B_{0.05}(PO_4)_3$ (B) sintered with the selected cycle, with a dwell at 1200ºC for 12h, both only crystallized in the high temperature triclinic phase. The SEM pictures confirm the low density achieved for both samples as one can observe large pores along the grain boundary and also a small grain size, especially for the $LiZr_2(PO_4)_3$ (A). This along with the failed attempts of densification confirms that more work was needed to achieve dense pellets for future electrical characterization.

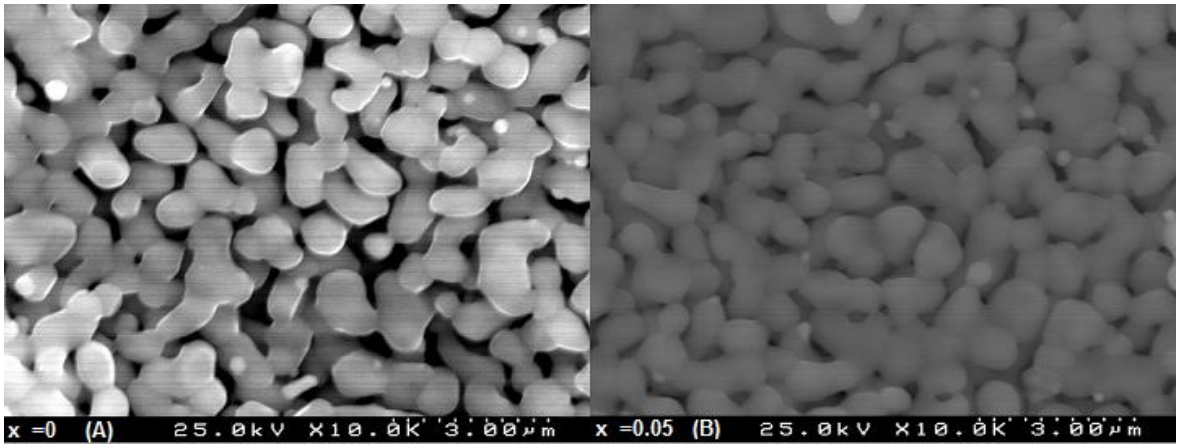

Figure 49: Microstructural analysis performed on sintered samples of $LiZr_2(PO_4)_3$ (A) and $Li_{1.05}Zr_{1.95}B_{0.05}(PO_4)_3$ (B) by SEM.

3.4. Conclusions

The method adapted from the recent work by Kim *et al* [51] does not offer good reproducibility as we could not achieve phase purity for $LiZr_2(PO_4)_3$. ZrP_2O_7 impurity peaks were always detected by powder XRD of the B doped and undoped $LiZr_2(PO_4)_3$ powders. However it was possible to achieve phase purity for $LiZr_2(PO_4)_3$ with the method adapted from the older work by Alamo *et al* [50].

With the method adapted from Alamo *et al* [50] it was clearly observed that the Zr-site is the preferential mechanism for B doping of $LiZr_2(PO_4)_3$ and not the P-site. With Li_3BO_3 impurity peaks being detected in all the samples prepared by B doping of the P-site, while no impurity peaks were detected for the samples prepared by B doping of the Zr-site, up to the composition $Li_{1.20}Zr_{1.80}B_{0.20}(PO_4)_3$.

On consideration of Vegard's law, after Rietveld refinement of the unit-cell parameters of the several synthesized compositions using the method adapted from Alamo *et al* [50], we verified that it is possible to obtain phase purity only up to $x = 0.05$. This conclusion coincides with the XRD data, which showed that after $Li_{1.075}Zr_{1.925}B_{0.075}(PO_4)_3$ there is no solid solution, because low temperature phase (monoclinic) peaks start being detected for the powder sintered at 1200ºC for 12h of compositions with $x \geq 0.075$.

The undoped and doped phases inside solid solution behave in accordance with the data in the literature of the undoped composition when analyzed by powder XRD under increasing temperature. Both compositions undergo phase transition from triclinic (PDF#01-074-2562) to rhombohedral (PDF#01-070-6734) for the high temperature phase when heating from 25ºC to 100ºC.

Despite the efforts, it was not possible to obtain dense pellets and with physical integrity after sintering, suggesting more work would be needed in order to try further approaches to progress to the next goal of measuring impedance for $LiZr_2(PO_4)_3$ and $Li_{1.05}Zr_{1.95}B_{0.05}(PO_4)_3$. All data pointed to the main issue deterring the densification of the sintered pellets to be the by-product NH_4Cl salt of the sol-gel synthesis that could probably be removed by heat treatment between 400 and 700ºC without compromising the integrity and densification of the pellets. Unfortunately there was no more time to test other temperatures and conditions.

Chapter 4 - Conclusions

Results showed that it is not possible to obtain a pure LLTO perovskite phase through mechanosynthesis, for the different conditions and the seven precursors combinations studied. However, the results showed that, as expected, the temperature and time needed to achieve a crystalline LLTO phase decreased to 1000ºC for 1h, when compared to the conventional solid state reaction (around 1350ºC for more than 1h).

Of all the seven combinations of precursors and conditions tested, the one where we milled activated La_2O_3 powder with Li_2CO_3 and TiO_2 for 480min (LaOLiCO-480) showed the best results, with impurity phases still being observed (22.84% after mechanosynthesis and 4.20% after calcination). The main impurity phase after calcination was that of Li_2TiO_3

As phase purity was not obtained, it was not possible to further analyze and modify the LLTO prepared by mechanosynthesis.

The method adapted from the recent work by Kim *et al* [51] for the preparation of NZP materials does not present good reproducibility as we could not achieve phase purity for $LiZr_2(PO_4)_3$, with ZrP_2O_7 impurity peaks always detected by powder XRD of the B doped and $LiZr_2(PO_4)_3$ powders. However it was possible to achieve phase purity for $LiZr_2(PO_4)_3$ with the method adapted from the older work by Alamo *et al* [50].

With the method adapted from Alamo *et al* [50] it was clearly observed that the Zr-site is the preferential mechanism for B doping of $LiZr_2(PO_4)_3$ and not the P-site, with Li_3BO_3 impurity peaks being detected in all the samples prepared by B doping of the P-site. On the contrary, phase purity was obtained for the samples prepared by B doping of the Zr-site, up to the composition $Li_{1.20}Zr_{1.80}B_{0.20}(PO_4)_3$

On consideration of Vegard's law, after Rietveld refinement of the unit-cell parameters of the several synthesised compositions using the method adapted from Alamo *et al* [50] we verified that it is possible to obtain phase purity only up to $x = 0.05$ in agreement with the XRD patterns, which showed the presence of low temperature phase (monoclinic) peaks for the powder sintered at 1200ºC for 12h of compositions with $x \geq 0.075$.

The phase pure undoped and doped phases behave in accordance with the data in the literature of the undoped composition when analyzed by powder XRD under increasing temperature. Both undergo phase transition from triclinic (PDF#01-074-2562) to rhombohedral (PDF#01-070-6734) for the high temperature phase when heating from 25ºC to 100ºC.

Despite the efforts, it was not possible to obtain dense pellets with physical integrity after sintering. More time must be committed to this goal before the electrical properties of $LiZr_2(PO_4)_3$ and $Li_{1.05}Zr_{1.95}B_{0.05}(PO_4)_3$ can be measured. All data pointed to the main issue deterring the densification of the sintered pellets to be the by-product NH_4Cl salt of the sol-gel synthesis that could probably be removed between 400 and 700ºC without compromising the integrity and densification of the pellets. Sintering time is also indicated as a highly important variable. Unfortunately there was no more time to test other temperatures and conditions.

Although the optimization of LLTO and $LiZr_2(PO_4)_3$ wasn't achieved, one can say that this work has contributed to the search for better and more sustainable technology of future energy storage solutions, by providing knowledge in materials preparation of two different electrolytes for Li-batteries from two distinct structural families and with two different synthesis procedures.

4.1. Future work

Regarding LLTO, the presence of La_2O_3 in the end of the mechanosyntheses suggests that the activity of this precursor must be increase. This may be performed by increased time or rotation speeds during the mechanical activation of the La_2O_3 powder and then adding this highly activated precursor to the Li_2CO_3 and TiO_2 precursors To avoid formation of Li_2TiO_3 it may also be beneficial to mechanically activate the TiO_2 and La_2O_3 precursors separately and then only add the Li-precursor to this activated mixture for subsequent mechanosynthesis. Other suggestions are more aggressive milling, for example, higher rotation velocities or a higher ball to powder ratio. The first of these is difficult as the rotation velocity used was already the maximum attainable from the Retzch PM200 planetary mill utilised. However, the second of these suggestions would be an easy experiment to be performed that has previously been shown to improve mechanosynthesis [56]. Changing the diameters of the balls used or use another material for the vial and balls could also be tested as both these factors have also been previously reported to enhance mechanosynthesis [56],[57].

Regarding $LiZr_2(PO_4)_3$, the ability to dope B on the Zr-site was a successful result of the current work. However, the inability to densify the undoped and B-doped compositions within the solid solution is a serious limitation to their application. Possible routes to improve the densification behaviour were highlighted to those of longer sintering times and careful control of the calcination cycle for the decomposition of the by-product NH_4Cl salt. A detailed sintering study is, therefore, suggested both by two-step sintering cycles using a long second dwell at a lower temperature, where Li-volatilisation would be less of an issue, and by careful analysis of dilatometric measurements of different sintering cycles. Intermediate milling, of the oven dried gel or the calcined powder, at higher energies or longer times can also be attempted as can the use of sintering additives, for example ZnO has been suggested as a sintering aid for similar materials [58]. However Barre *et al* [59] showed that at least for another NZP material, $Li_{0.4}La_{0.2}Zr_2(PO_4)_3$, the use of sintering additives like ZnO, B_2O_3, TiO_2, and $LiNO_3$ did not lead to sufficiently well-densified pellets (<70%). They achieved good values of densification using spark plasma sintering (SPS), and developed an alternative method consisting of a preliminary milling step (500rpm, 240min) followed by a flash heating at high temperature (1450°C, 5min); methods that they suggest can be applied for every compound which cannot be heated at high temperature, and, therefore, relevant to the current case [59]. After this densification is achieved, the originally planned electrochemical characterization can be performed.

References

[1] International Energy Agency (IEA), *Key World Energy Statistics*, France, 2011.

[2] S. Al-Hallaj, K. Kiszynski, *Hybrid Hydrogen Systems: Stationary and Transportation Applications*, Springer-Verlag, London, 2011.

[3] *Renováveis - estatísticas rápidas*, 109, DGGE 2014: retrieved from www.dgeg.pt on 26-06-2014.

[4] B. Scrosati and J. Garche, *Lithium batteries: status, prospects and future*, Journal of Power Sources 195 (2010) 2419-2430.

[5] E. Quartarone and P. Mustarelli, *Electrolytes for solid-state lithium rechargeable batteries: recent advances and perspectives*, Chemical Society Reviews 40 (2011) 2525-2540.

[6] T.M. Bandhauer, S. Garimella and T.F. Fuller, *A Critical Review of Thermal Issues in Lithium-Ion Batteries*, Journal of The Electrochemical Society 158(3) (2011) R1-R25.

[7] Y. Shimonishi *et al*, *A study on lithium/air secondary batteries—Stability of the NASICON-type lithium ion conducting solid electrolyte in alkaline aqueous solutions*, Journal of Power Sources 196 (2011) 5128-5132.

[8] Y. Shimonishi *et al*, *A study on lithium/air secondary batteries—Stability of NASICON-type glass ceramics in acid solutions*, Journal of Power Sources 195 (2010) 6187-6191.

[9] A. Väyrynen and J. Salminen, *Lithium ion battery production*, The Journal of Chemical Thermodynamics 46 (2012) 80–85.

[10] T. Ogasawara, A. Débart, M. Holzapfel, P. Novák, P.G. Bruce, *Rechargeable LI_2O_2 electrode for lithium batteries*, Journal of the American Chemical Society 128 (2006) 1390-1393.

[11] V.Thangadurai, A.K. Shukla and J. Gopalakrishnan, *New lithium-ion conductors based on the NASICON structure*, Journal of Materials Chemistry 9 (1999) 739.

[12] R. Padbury and X. Zhang, *Lithium–oxygen batteries—Limiting factors that affect performance*, Journal of Power Sources 196 (2011) 4436-4444.

[13] V. Thangadurai and W. Weppner, *Recent Progress in Solid Oxide and Lithium Ion Conducting Electrolytes Research*, Ionics 12 (2006) 81-92.

[14] Z. Sherafat, I. Antunes, C. Almeida, J.R. Frade, M.H. Paydar, G.C. Mather and D.P. Fagg, *Enhanced $BaZrO_3$ mechanosynthesis by the use of metastable ZrO_2 precursors*, Dalton Transactions 43 (2014) 9324-9333.

[15] N. Nasani, P.A.N. Dias, J.A. Saraiva and D.P. Fagg, *Synthesis and conductivity of $Ba(Ce,Zr,Y)O_{3-d}$ electrolytes for PCFCs by new nitrate-free combustion method*, Int. J. Hydrogen Energy, 38(20) (2013) 8461-8470.

[16] N. Nasani, P.N. Dias, G.C. Mather and D.P. Fagg, *The importance of phase purity in Ni-$BaZr_{0.85}Y_{0.15}O_{3-d}$ cermet anodes – Novel nitrate-free combustion route and electrochemical study*," RSC Advances, 3(3) (2013) 859.

[17] A.D. Brandão, I. Antunes, J.R. Frade, J. Torre, V.V. Kharton and D.P. Fagg, *Enhanced low-temperature proton conduction in $Sr_{0.02}La_{0.98}NbO_{4-d}$ by scheelite phase retention*, Chemistry of Materials 22(24) (2010) 6673.

[18] D.P. Fagg, S. Garcia-Martin, V.V. Kharton and J.R. Frade, *Transport properties of fluorite-type $Ce_{0.8}Pr_{0.2}O_{2-d}$ containing 2mol% and 5mol% additions of Co oxide sintering aid*, Chemistry of Materials 21(2) (2009) 381.

[19] K.Y. Yang, J.W. Wang and K.Z. Funga, *Roles of lithium ions and La/Li-site vacancies in sinterability and total ionic conduction properties of polycrystalline $Li_{3x}La_{2/3-x}TiO_3$ solid electrolytes $(0.21 \leq 3x \leq 0.50)$*, Journal of Alloys and Compounds 458 (2008) 415-424.

[20] F. Suderau, D. Petit and J.P. Boilot, *Dimorphism, Phase Transitions, and Transport Properties in $LiZr_2(P0_4)_3$*, Journal of Solid State Chemistry 83 (1989) 78-90.

[21] K.Y. Yang *et al*, *Mechanism of the interfacial reaction between cation-deficient $La_{0.56}Li_{0.33}TiO_3$ and metallic lithium at room temperature*, Journal of Materials Research 23 (7) (2008) 1813-1825.

[22] C. W. Ban and G. M. Choi, *The effect of sintering on the grain boundary conductivity of lithium lanthanum titanates*, Solid State Ionics 140 (2001) 285-292.

[23] P. Jia, Z. Shao and K. Liu, *Synthesis and electrochemical performance of $Li_4Ti_5O_{12}$ by high temperature ball milling method*, Materials Letters 125 (2014) 218-220.

[24] A. Mei et al, *Role of amorphous boundary layer in enhancing ionic conductivity of lithium–lanthanum–titanate electrolyte*, Electrochimica Acta 55 (2010) 2958–2963.

[25] H.X. Geng, A. Mei, C. Dong, Y.H. Lin and C.W. Nan, *Investigation of structure and electrical properties of $Li_{0.5}La_{0.5}TiO_3$ ceramics via microwave sintering*, Journal of Alloys and Compounds 481 (2009) 555–558.

[26] I. Antunes, A. Brandão, F.M. Figueiredo, J.R. Frade, J. Gracio and D.P. Fagg, *Mechanosynthesis of nanopowders of the proton-conducting electrolyte material $Ba(Zr,Y)O_{3-\delta}$*, Journal of Solid State Chemistry 182 (8) (2009) 2149-2156.

[27] V. V. Zyryanov, *Ultrafast mechanochemical synthesis of mixed oxides*, Inorganic Materials, 41(4) (2005) 378-392.

[28] V.V. Zyryanov, *Mechanism of mechanochemical synthesis of complex oxides and the peculiarities of their nano-structurization determining sintering*, Science of Sintering, 37 (2005) 77-92.

[29] E. Ivanov and C. Suryanarayana, *Materials and Process Design through Mechanochemical Routes*, Journal of Materials Synthesis and Processing, 8 (3/4) (2000) 235-244.

[30] R. O. Fuentes, E. Chinarro, F. M. Figueiredo, R. Soares, F. M. B. Marques and J. R. Frade, *Processing of submicrometric $CaTi_{0.8}Fe_{0.2}O_{3-\delta}$ ceramics by mechanical activation*, Journal of Materials Science 41 (2006) 7393-7400.

[31] V.V. Zyryanov *et al*, *Mechanosynthesis of complex oxides with fluorite and perovskite-related structures and their sintering into nanocomposites with mixed ionic–electronic conductivity*, Solid State Ionics 176 (37-38) (2005) 2813-2818.

[32] J.F.Monteiro, A.A.L.Ferreira, I.Antunes, D.P.Fagg, J.R.Frade, *Thermodynamic restrictions on mechanosynthesis of strontium titanate*, Journal of Solid State Chemistry 185 (2012) 143-149.

[33] P. Baláž *et al*, *Hallmarks of mechanochemistry: from nanoparticles to technology*, Chemical Society Reviews 42 (2013) 7571- 7637.

[34] V. Sepelák *et al*, *Mechanochemical reactions and syntheses of oxides*, Chemical Society Reviews 42 (2013) 7507-7520.

[35] M.N Obrovac, O Mao and J.R Dahn, *Structure and electrochemistry of $LiMO_2$ (M=Ti, Mn, Fe, Co, Ni) prepared by mechanochemical synthesis*, Solid State Ionics 112 (1-2) 1998 9-19.

[36] P. Jia, Z. Shao and K. Liu, *Pretreatments-assisted high temperature ball milling route to $Li_4Ti_5O_{12}$ and its electrochemical performance*, Materials Letters 130 (2014) 71-74.

[37] M. Senna, *The promising aspects of processing nanomaterials under mechanical stressing for physicochemical viewpoints*, Advanced Powder Technology 21 (2010) 586–591.

[38] H. Xie, J.B. Goodenough, Y. Li, *$Li_{1.2}Zr_{1.9}Ca_{0.1}(PO_4)_3$, a room-temperature Li-ion solid electrolyte*, Journal of Power Sources 196 (2011) 7760–7762.

[39] A. Ramzy and V. Thangadurai, *Tailor-Made Development of Fast Li Ion Conducting Garnet-Like Solid Electrolytes*, ACS Applied Materials Interfaces 2 (2010) 385–390.

[40] A. Clearfield in *Proton Conductors: Solids, Membranes and Gels-Materials and Devices*, Ed. P. Colomban, Cambridge University Press, Cambridge, 1992.

[41] A.B. Yaroslavtsev and I.A. Stenina, *Complex phosphates with the NASICON structure ($M_xA_2(PO_4)_3$)*, Russian Journal of Inorganic Chemistry, 51(2006) S97-S116.

[42] D.A. Woodstock and P. Lightfoot, *Comparison of the structural behaviour of the low thermal expansion NZP phases $MTi_2(PO_4)_3$ (M = Li, Na, K)*, Journal of Materials Chemistry 9 (1999) 2907-2911.

[43] H.Y-P. Hong, Crystal structures and crystal chemistry in the system $Na_{1+x}Zr_2Si_xP_{3-x}O_{12}$, Materials Research Bulletin 11 (1976) 173-182.

[44] J.E.Iglesias, C.Pecharroman, *Room temperature triclinic modification of NASICON-type $LiZr_2(PO_4)_3$*, Solid State Ionics 112 (1998) 309–318.

[45] M. Catti, S. Stramare, R. Ibberson, *Lithium location in NASICON-type Li conductors by neutron diffraction. I. Triclinic α'-$LiZr_2(PO_4)_3$*, Solid State Ionics 123 (1999) 173–180.

[46] M. Casciola *et al*, *Preparation, structural characterization and conductivity of $LiZr_2(PO_4)_3$*, Solid State Ionics 26 (1988) 229-235.

[47] T. Suzuki *et al*, *Stabilization of superionic conduction phase in $Li_3Sc_2(PO_4)_3$,* Solid State Ionics 104 (1997) 27-33.

[48] T. Šalkus *et al*, *Fabrication and electrical properties of $Li_3Sc_{2-x}B_x(PO_4)_3$ superionic materials*, Lithuanian Journal of Physics 45 (4) (2005) 257–262.

[49] R.S. Futagami, M. Nishimori, H. Nishizawa, Hydrothermal synthesis and electric conductivity of the NASICON-related solid solution, $Na_{1+2x}Ti_2B_xP_{3-x}O_{12}$, Journal of Materials Science Letters 19 (2000) 405–407.

[50] J. Alamo and J.L. Rodrigo, *Thermal expansion of $LiZr_2(PO_4)_3$: water inclusion influence*, Solid State Ionics 32/33 (1989) 70-76.

[51] H.S. Kim, H. S. Ahnn, J.H. Lee, Y.K. Sun and Chong S. Yoon, *Electrochemical Properties of Sol-Gel Prepared $Li_2Zr_xTi_{1-x}(PO_4)_3$ Electrodes for Lithium Secondary Batteries*, Journal of the Electrochemical Society 158 (4) (2011) A396-A399.

[52] R.D. Shannon, *Revised effective ionic radii and systematic studies of interatomic distances in halides and chalcogenides*, Acta Crystallographica A32(5) (1976) 751-767. Data retrieved from www.webelements.com on 20-02-2013.

[53] M. Barre, M. P. Crosnier-Lopez, F. Le Berre, J. Emery, E. Suard, and J.-L. Fourquet, *Room Temperature Crystal Structure of $La_{1/3}Zr_2(PO_4)_3$, a NASICON-type Compound*, Chemistry of Materials 17 (2005) 6605-6610.

[54] http://www.engineeringtoolbox.com/fuels-ignition-temperatures-d_171.html, Data retrieved on 30-05-2013.

[55] Y. Hasegawa, S. Tamura, and N. Imanaka, *Effect of Low-melting Oxide Additives on the Sinterability and Ion Conductivity of Al^{3+} Ion Conducting Solid Electrolytes with the NASICON Type Structure*, Journal of New Materials for Electrochemical Systems 8 (2005) 203-207.

[56] A. Perejón, *Direct mechanosynthesis of pure $BiFeO_3$ perovskite nanoparticles: reaction mechanism*, Journal of Materials Chemistry C (2013) 3551-3562.

[57] D. Tank, F. Patel and S. Patel, *Review Paper on Perovskite Prepared by Reactive Grinding*, International Conference on Current Trends in Technology, NUiCONE (2011).

[58] M. V. Sukhanov, V. I. Pet'kov, and D. V. Firsov, *Sintering Mechanism for High-Density NZP Ceramics*, Inorganic Materials 27 (2011) 674–678.

[59] M. Barré *et al*, *The NASICON solid solution $Li_{1-x}La_{x/3}Zr_2(PO_4)_3$: optimization of the sintering process and ionic conductivity measurements*, Ionics 15 (2009) 681–687.

Appendix

Table A 1: Stoichiometric amounts of reagents needed to synthesize LLTO.

$m_{reagents}$ (g)	Mechanosynthesis	Lanthanum		Lithium		Titanium
		precursor	m (g)	precursor	m (g)	$mTiO_2$ (g)
4.5000	LaOLiOH.W	La_2O_3	2.0106	$LiOH.H_2O$	0.5179	1.9715
4.5000	LaOHLiOH.W	$La(OH)_3$	2.1824	$LiOH.H_2O$	0.4822	1.8354
4.5000	LaOLiOH	La_2O_3	2.1151	LiOH	0.3109	2.0739
4.5000	LaOLiCO	La_2O_3	2.0387	Li_2CO_3	0.4623	1.9990
4.5000	LaOLiAcetate	La_2O_3	1.7263	$CH_3COOLi.2H_2O$	1.0810	1.6927

Table A 2: Stoichiometric amounts of reagents needed to synthesize 2.0g of $Li_{1+6x}Zr_2(P_{1-x}B_xO_4)_3$, with x= 1.42965 and y=2.57035.

$m(CH_3COOLi.2H_2O)$ (g)	$m[(CH_3COO)_xZr(OH)_y]$ (g)	$m(H_3PO_4)$ (g)	$m(H_3BO_3)$ (g)	$m(C_6H_8O_7)$ (g)	$M[Li_{1+6x}Zr_2(P_{1-x}B_xO_4)_3]$ (g/mol)	x
0.4435	1.8499	1.4584	0.0000	18.3197	474.3032	0.00
0.5777	1.8536	1.3883	0.0393	20.1918	473.3611	0.05
0.7124	1.8573	1.3178	0.0787	22.0714	472.4190	0.10
0.8477	1.8610	1.2471	0.1183	23.9584	471.4768	0.15
0.9835	1.8647	1.1761	0.1580	25.8530	470.5347	0.20
1.1198	1.8684	1.1048	0.1979	27.7552	469.5926	0.25

Table A 3: Stoichiometric amounts of reagents needed to synthesize 2.0g of $Li_{1+x}Zr_{2-x}B_x(PO_4)_3$, with x= 1.42965 and y=2.57035.

$m[CH_3COOLi.2H_2O]$ (g)	$m[(CH_3COO)_xZr(OH)_y]$ (g)	$m[H_3PO_4]$ (g)	$m[H_3BO_3]$ (g)	$m[C_6H_8O_7]$ (g)	$M[Li_{1+x}Zr_{2-x}B_x(PO_4)_3]$ (g/mol)	x
0.4435	1.8499	1.4584	0.0000	18.3197	474.3032	0.00
0.4693	1.8177	1.4698	0.0132	18.4627	470.6296	0.05
0.4955	1.7850	1.4814	0.0265	18.6080	466.9560	0.10
0.5221	1.7518	1.4931	0.0401	18.7555	463.2824	0.15
0.5492	1.7181	1.5050	0.0539	18.9054	459.6088	0.20
0.5767	1.6838	1.5172	0.0679	19.0578	455.9352	0.25

Table A 4: Stoichiometric amounts of reagents needed to synthesize 2.0g of $Li_{1+6x}Zr_2(P_{1-x}B_xO_4)_3$.

m[$ZrOCl_2.8H_2O$] (g)	m(H_3BO_3) (g)	m[Li_2CO_3] (g)	m($NH_4H_2PO_4$) (g)	M[$Li_{1+6x}Zr_2(P_{1-x}B_xO_4)_3$] (g/mol)	x
2.7313	0.0000	0.1574	1.4552	474.30320	0.00
2.7368	0.0393	0.2050	1.3852	473.36108	0.05
2.7422	0.0787	0.2528	1.3149	472.41896	0.10
2.7477	0.1183	0.3008	1.2443	471.47684	0.15
2.7532	0.1580	0.3490	1.1735	470.53472	0.20
2.7587	0.1979	0.3974	1.1023	469.59260	0.25

Table A 5: Stoichiometric amounts of reagents needed to synthesize 2.0g of $Li_{1+x}Zr_{2-x}B_x(PO_4)_3$.

m[$ZrOCl_2.8H_2O$] (g)	m(H_3BO_3) (g)	m[Li_2CO_3] (g)	m($NH_4H_2PO_4$) (g)	M[$Li_{1+x}Zr_{2-x}B_x(PO_4)_3$] (g/mol)	x
2.7313	0.0000	0.1574	1.4552	474.30320	0.000
2.7077	0.0066	0.1619	1.4608	472.46640	0.025
2.6839	0.0132	0.1665	1.4665	470.62960	0.050
2.6598	0.0198	0.1712	1.4723	468.79280	0.075
2.6356	0.0265	0.1758	1.4781	466.95600	0.100
2.5866	0.0401	0.1853	1.4898	463.28240	0.150
2.5368	0.0539	0.1949	1.5017	459.60880	0.200
2.4862	0.0679	0.2046	1.5138	455.93520	0.250